GaAs/AlGaAs BIPOLAR TRANSISTOR WAVEGUIDE STRUCTURE CARRIER-INJECTED OPTICAL MODULATOR/SWITCH

(GaAs/AlGaAs系バイポーラ・トランジスタ導波路構造
キャリア注入型光変調器・スイッチに関する研究)

THESIS
Submitted in partial satisfaction of
the requirements for the degree of
Doctor of Philosophy

by YOSHITAKA OKADA

Advisor
Professor KUNIO TADA, ph.D

Department of Electronic Engineering
Faculty of Engineering
University of Tokyo

ACKNOWLEDGEMENTS

I would like to express my deepest gratitude to Professor Kunio Tada for his kind guidance and encouragement throughout the course of this study. Without his valuable suggestions and constant understanding and encouragement, none of this work could have been accomplished. I would also like to express my sincere appreciations to Professors James L. Merz, Larry A. Coldren, and Herbert Kroemer of the University of California at Santa Barbara, for their fruitful discussions and comments.

I would like to thank Dr. Y. Nakano, Mr. T. Murai and Ms. M. Washiyama for their kind advice and continuous support and guidance throughout the course of this study. Also deeply appreciated are Dr. K. Ishida and Dr. H. Inoue of Hitachi Central Laboratory for their valuable technical support and comments.

I would like to thank the members of the Professor Tada's Laboratory and my colleagues at the University of Tokyo for their valuable help, suggestions, and warm friendship. They are Dr. Y. C. Liang, Mrs. Y-S. Li, and Messieurs H. Hayashi, T. Ishikawa with very special thanks, Y. Luo, H. Nakamura, Y. C. Chan, and Miss E. Momiyama. I am especially thankful to M. Nakayama, M. Gotoda, and T. Higuchi for their priceless efforts and direct collaboration and commitment to this work. I am also thankful to R-H. Yan, R. J. Simes, M. Nishiguchi, and T. Takamori of the University of California at Santa Barbara, for their fruitful discussions and friendship during my stay in the U.S.A. for 1987–88. I am further indebted to Dr. S. Hirata of Sony Central Laboratory for supplying the GaAs DFB laser diodes, H. Yanagawa of Furukawa Electric for supplying the short-wavelength single-mode optical fibers, and Y. Tono-oka of NEC Corporation for supplying the photomasks used in this work.

Finally, I would like to acknowledge Professor L. A. Lindsay at King's College of the University of London for his kind encouragement and understanding. Thanks are also due to the Fulbright Committee for their support during my stay in the U.S.A. And I would especially like to dedicate this work to my beloved parents for their love and courage to endure the loneliness for the success of their only son.

PUBLICATIONS

I. Research Papers

[1] K. Tada and Y. Okada
"Bipolar Transistor Carrier-Injected Optical Modulator/Switch; Proposal and Analysis"
IEEE Electron Device Letters, **EDL–7**, 11, pp. 605–606, 1986.

[2] Y. Okada, R-H. Yan, L. A. Coldren, J. L. Merz, and K. Tada
"The Effect of Band-Tails on the Design of GaAs/AlGaAs Bipolar Transistor Carrier-Injected Optical Modulator/Switch"
IEEE Journal of Quantum Electronics, **25**, 4, pp. 713–719, 1989.

[3] Y. Okada, T. Ishikawa, and K. Tada
"Optical intensity modulator for integrated optics by use of heterojunction bipolar transistor waveguide structure"
Applied Physics Letters, **55**, 25, pp. 2591–2593, 1989.

[4] Y. Okada and K. Tada
"Analysis of GaAs/AlGaAs Reflection-Type Optical Switch Using Bipolar Transistor Waveguide Structure"
to be submitted to *Photonic Switching II*, Springer Series (New York, 1990).

II. International and Domestic Conferences

[5] K. Tada and Y. Okada
"Proposal of Bipolar Transistor Carrier-Injected Optical Modulators and Switches"
Extended Abstracts of the 18th. (International) Conference on Solid State Devices and Materials (ssdm86), pp. 169–172, Tokyo, Aug. 1986.

[6] Y. Okada, R-H. Yan, L. A. Coldren, J. L. Merz, and K. Tada
"The Effect of Bandtailing on the Performance of GaAs/AlGaAs Optical Modulators and Switches Operated by Free Carrier Injection"
Conference Proceedings of the 1st. IEEE/LEOS Annual Meeting (LEOS'88), pp. 47–49, Santa Clara (U.S.A.), Nov. 1988.

[7] Y. Okada, R. J. Simes, L. A. Coldren, J. L. Merz, and K. Tada
"GaAs/AlGaAs Double-Heterojunction Bipolar Transistor Carrier-Injected Optical Intensity Modulator"
Extended Abstracts of the 21st. Conference on Solid State Devices and Materials (ssdm89), pp. 449–452, Tokyo, Aug. 1989.

[8] Y. Okada, T. Ishikawa, Y. Nakano, and K. Tada
"GaAs/AlGaAs Double-Graded Heterojunction Bipolar Transistor Prepared by MBE with Precise Temperature Control Using Modern Control Theory"
Technical Digest of the 1st. International Meeting on Advanced Processing and Characterization Technologies (APCT'89), pp. 191–194, Tokyo, Oct. 1989.

[9] K. Tada, Y. Okada, and T. Ishikawa
"Semiconductor Optical Modulator/Switch with Heterojunction Bipolar Transistor Waveguide Structure"
Technical Digest of the 2nd. Regional Symposium on Optoelectronics, pp. 3–6, Jakarta (Indonesia), Nov. 1989.

[10] Y. Okada and K. Tada
"GaAs/AlGaAs Reflection-Type Optical Switch Using Heterojunction Bipolar Transistor Waveguide Structure"
To be presented at *1990 International Topical Meeting on Photonic Switching (PS'90)*, Kobe, April 1990.

[11] K. Tada, Y. Nakano, T, Ishikawa, Y. Okada, and Y. C. Chan (Invited)
"Precise Control of MBE System and Application to Thin Film Photonic Devices"
to be presented at *C-MRS (Material Research Society) International 1990 Symposium*, Beijing (China), June 1990.

(III)全国大会・学会研究会

[12] 多田邦雄・岡田至崇

「バイポーラトランジスタ構造キャリア注入型光スイッチの提案」

1986年(昭和61年)春季第33回応用物理学関係連合講演会，4a-L-5，(於・日本大学).

[13] 多田邦雄・岡田至崇

「バイポーラトランジスタ構造キャリア注入型光スイッチとその特性解析」

昭和61年度電子通信学会総合全国大会，962，(於・新潟大学).

[14] 岡田至崇・林秀樹・中野義昭・多田邦雄

「キャリア注入型光変調器／スイッチ用ヘテロ接合バイポーラトランジスタの試作」

昭和62年度電子情報通信学会半導体・材料部門全国大会，339，(於・熊本大学).

[15] 岡田至崇・多田邦雄・R. H. Yan・L. A. Coldren・J. L. Merz

「バンドテイル・モデルを用いたキャリア注入型光変調器／スイッチの特性解析」

1988年(昭和63年)秋季第49回応用物理学会学術講演会，5p-S-15，(於・富山大学).

[16] 岡田至崇・多田邦雄・R. J. Simes・L. A. Coldren・J. L. Merz

「ヘテロ接合バイポーラトランジスタ構造単一ガイド型キャリア注入型光変調器」

1989年電子情報通信学会秋季全国大会，4-199，(於・神奈川大学).

[17] 岡田至崇・石川卓哉・多田邦雄

「傾斜ヘテロ接合バイポーラトランジスタ構造キャリア注入型光強度変調器の作製」

1989年(平成元年)秋季第50回応用物理学会学術講演会，27p-ZH-11，(於・福岡工大).

[18] 岡田至崇・多田邦雄

「反射型バイポーラトランジスタ導波路構造キャリア注入型光スイッチの検討」

1990年(平成2年)春季第37回応用物理学関係連合講演会，(於・東洋大学朝霞校舎).

[19] 岡田至崇・石川卓哉・多田邦雄

「ノンアロイ・オーミックコンタクトのＨＢＴ構造キャリア注入型光変調器への適用」

1990年(平成2年)春季第37回応用物理学関係連合講演会，(於・東洋大学朝霞校舎).

[20] 岡田至崇・多田邦雄、
「バイポーラ・トランジスタ構造半導体キャリア注入型光スイッチ」
第4回電子情報通信学会・集積光エレクトロニクス研究会, 1990.2.23, (於・東京大学).

[21] 岡田至崇・多田邦雄、
「バイポーラ・トランジスタ構造キャリア注入型光変調器・スイッチ」
固体エレクトロニクス・オプトエレクトロニクス研究会, 1990.3.6, (於・東京大学).

(IV) その他

[22] 多田邦雄・岡田至崇
「バイポーラ・トランジスタ構造半導体キャリア注入型光変調器・スイッチ」
刊行誌OplusEに掲載予定。

TABLE OF CONTENTS

References are included at the end of each Chapter.

CHAPTER 1

INTRODUCTION AND MOTIVATION

Quest for Monolithic Integration

Recently, the development of high performance semiconductor optical sources (lasers), optical modulators and switches, optical switch arrays, and photodetectors for lightwave communication systems, optical signal processing, and optoelectronic or photonic integrated circuits (OEICs or PICs) have been the focus of intense research activity accompanying the improvements in the transparency and bandwidth of optical fibers. Preponderance of the advances in optoelectronic components has dealt with discrete forms of devices made using GaAs/AlGaAs material system for short-wavelength transmission ($\lambda \sim 0.8$–0.9 μm), whereas InP/InGaAs(P) alloys have been investigated for long-wavelength ($\lambda < 1.65$ μm) applications. The usefulness of devices made from these two material systems can be summarized in general, as follows; Short-wavelength GaAs-based devices are useful for short-haul (0–3 km), low-cost, and high fiber-density applications such as local area networks (LANs) or computer interconnects. On the other hand, long-wavelength InP-based devices are used in long-haul (3–200 km) low fiber-density communication links.

Although considerable works have been conducted in order to improve the performance and reduce the cost of discrete components in both material systems, until recently have efforts been expended in the integration of photonic and electronic components on a single chip of GaAs or InP (or even on Si). The potential advantages inherent in such monolithic integration may, with caution, be drawn from the experiences with electronic integration using Si and GaAs. In general, electronic integration of multiple components can lead to a reduction in cost, an increase in functionality, and an improvement in performance over a similar hybrid circuit. Therefore, it is quite reasonable to conclude that monolithic integration of both the photonic and the electronic components would lead to the same watershed of advantages as has accompanied the electronic integration.

PICs (In this work, no distinction is drawn between the term "OEIC" and the term "PIC", though some people prefer to stick to one term or the other.) have a number of advantages over simple electronic integrated circuits, which may allow large increases in performance and reliability over the currently available technology based on the integrated electronics, and printed circuit board interconnection of the

individual wafers. The motivation behind the development of PICs is to use existing electronic devices and circuits where they no not hinder the ability of the overall system to meet the performance specifications, but to switch over to optical circuitry where the use of optical signals can boost the system performance well beyond that obtainable with electronics alone. This scheme takes advantage of the very high bandwidth and extremely low cross-talk of optical waveguides, as compared to evaporated metal bus lines or printed circuit boards, when they are used to form optical interconnections between the electronic subunits. Optical signal processing also opens up the possibility of performing very high-speed computations with relatively simple optical circuit elements, which might otherwise require complex electronic circuits to do the same task. The benefits are not limited to the performance alone. Indeed, hybrid optoelectronic systems can almost match PICs, if the computational speed is the only factor considered. However, hybrid circuits pay a large penalty in size, cost, weight, and reliability when compared to monolithic PICs due to the complicated assembly procedures required.

Figure 1.1 shows an illustration of one such PIC circuit, which contains all the elements required of a fully operational system [1]. Here, the electronic subsystems are being employed such that the complexity and size of each unit is minimized allowing higher computational speeds within each unit than could be obtained by integrating all of them into one unit. The key advantage of this scheme is that optical circuits are used for ultra high-speed data transfer between these computational units. This is shown as the laser sources, optical waveguides, optical switches, and detectors joining the four computational units as well as the laser sources pointed off-chip for use with optical fiber inter-chip connections. As shown in the figure, the 4×4 switch array is reciprocal, i.e. capable of both the forward and the backward transmissions. The details of component selection within the array may, however, prevent it from obeying reciprocity. Therefore, optical components are used to shuttle information between the units and between the chips in such a manner that the usual information bottleneck, i.e. low bandwidth, high loss, and poor isolation, of electronic bus lines can be completely avoided. Such an example employing a similar idea as shown in Fig. 1.1 was reported very recently by H. Takeuchi *et al.* at NTT [2] at the *7th International Conference on Integrated Optics and Optical Fiber Communication (IOOC'89)*. Moreover, one can indeed even consider including vertically emitting lasers, or surface emitting lasers [3] located within the wafer as an additional, and even more flexible means of coupling light into optical fibers or sending light directly to another wafer located directly above.

Several reasons for the increased performance of optical circuits are well known [4], and will now be outlined. From the systems standpoint, the most interesting is that several signals can be multiplexed

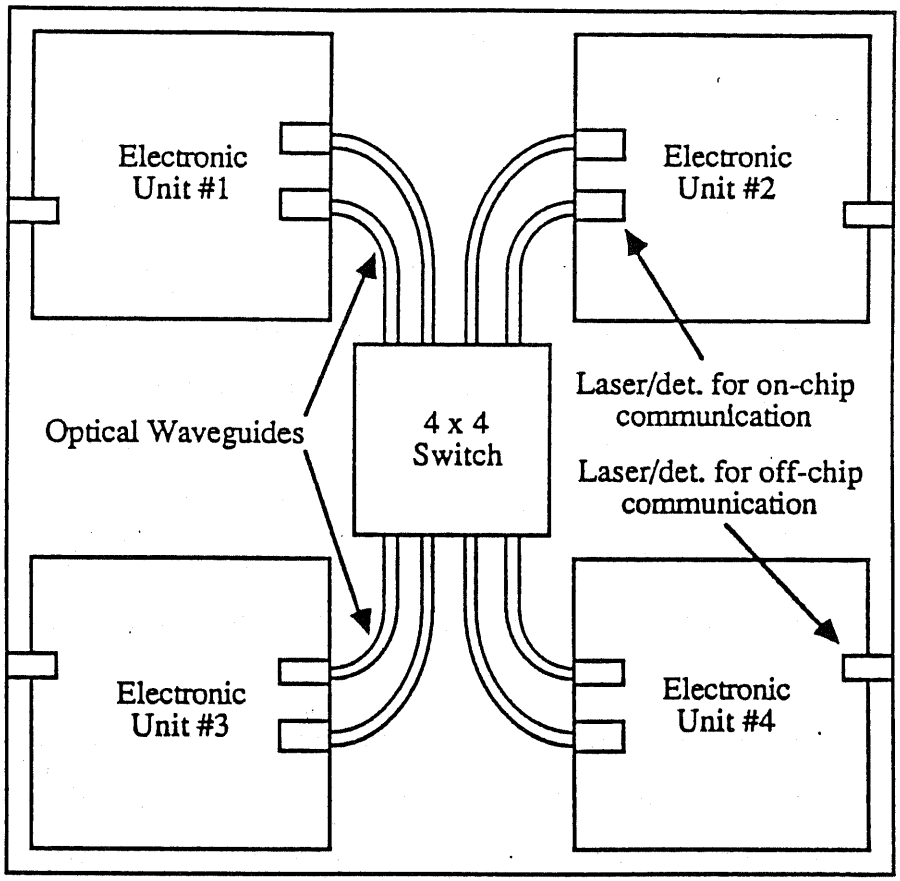

Fig. 1.1 Generalized illustration of an optoelectronic or photonic integrated circuit. Small rectangles are either semiconductor lasers or photodetectors, as required.

onto a single optical waveguide or fiber. This is believed to eliminate a great deal of redundancy in the interconnection lines. For example, frequency (or wavelength) multiplexing can be achieved by coupling two or more lasers operating at different wavelengths into a single guide. Demultiplexing is simply a matter of stacking detectors in series such that the absorption edge of each serves as a "long-pass" filter. In this manner, a single fiber could carry an entire 8 or 16-bit word as a parallel bus structure with a different wavelength for each bit. In fact, this technique has been used to multiplex 6 different laser sources onto a single waveguide [5]. However, three of the most important reasons for using optical interconnection and optical signal processing are the extremely low loss of optical waveguides at high frequencies, minimal cross-talk between the waveguides, and the extremely large bandwidth of optical waveguides. The loss issue can be illustrated by a simple example. As an inter-chip connection, a piece of optical fiber can be expected to have a loss, independent of the modulation frequency, of less than 5 dB/km at 0.85 μm, so that an 1 m section joining the two chips inside a computer would provide a loss of only 0.05 dB. In comparison, an 1 m section of RG58U coaxial cable in the same application provides a loss of 2 dB at 1 GHz, and 5 dB at 10 GHz. Clearly, at frequencies greater than 10 GHz, where high-power transistors are very difficult to build and even more difficult to integrate, the use of optical fiber or waveguide interconnections has distinct advantages.

Full realization of PICs still requires that a number of important technological problems be solved. Among these are; (i) the capability to couple laser output light efficiently into passive optical waveguides, (ii) development of high-quality optical modulator/switch and optical switching arrays, (iii) fabrication of low-threshold lasers, which do not disturb neighboring electronics with dissipated heat, (iv) the ability to place lasers randomly within the wafer without the need to form the Fabry-Perot facets via cleavage or dry-etching, and lastly, (v) development of a simple fabrication sequence capable of placing high-quality optical and electronic devices on the same wafer without compromising the performance of either type of device.

This dissertation aims to focus on just a few of these issues. It specifically centers on the proposal, design, fabrication, and characterization of high-quality optical modulators and switches, the device structures of which are particularly suitable for monolithic integration with other optical and electronic components. All of these are also tied together with an overall consideration for device structures and processes that are mutually compatible. For this purpose, the first bipolar transistor carrier-injected optical modulator/switch using a GaAs/AlGaAs double heterostructure (DH) waveguide structure is studied in this dissertation, which is not only expected to improve the overall performance of the optical

modulators and switches operated by the free-carrier injection, but also should be a useful device structure in possible PIC applications.

Importance of High-Quality Optical Modulators and Switches

By changing the index of refraction or absorption coefficient in a region of a material, it is possible to construct optical phase or absorption modulation elements as well as reflection-type optical switches for a propagating lightwave. The combination of the phase modulation element with an optical interferometer [6] or directional coupler [7] geometry can also provide amplitude modulation and optical switching. Absorption modulators [8], although somewhat simpler in concept, are not quite versatile, and potential problems with thermal heating, wavelength sensitivity, and disposing of the generated free carriers may exist.

This work is focused on a particularly desirable geometry for obtaining large index or absorption variations in optical waveguides in semiconductors. The resulting waveguide optical modulator/switch is directly useful in possible 4×4 optical switch arrays as illustrated in Fig. 1.1, and may form fundamental building blocks for more sophisticated forms of PICs. For this reason, it is desirable to create an optical modulator/switch, which is small in size and efficient, that is, one which provides the maximum index or absorption variation per unit length, per unit voltage or current. Maximizing this normalized modulation parameter will also result in increased speeds, if it can be made to increase more than the capacitance per unit length of the device structure. There is another parameter that should also be taken care of, that is, the chirp parameter, which may be simply defined as the ratio of the index to absorption variation (or more precisely, the ratio of the relative change of the real to imaginary parts of the refractive index), since both variations occur simultaneously and are related by the classical Kramers-Kronig relationship. As illustrated in Fig. 1.2, it has been pointed out that, for practical applications, the phase modulation due to the variation of the refractive index, which accompanies the intensity modulation in an absorption modulator, should be *minimized* in order to reduce the chirp-like spectral broadening [9]. For phase modulators, the requisite should be opposite.

Until recently, most of the optical modulators and switches are characterized by an efficient use of the linear electro-optic effect (LEO) or Pockels effect as the main scheme of modulation/switching method. However, a complete understanding of the different effects that can change the refractive index or absorption in the waveguide region, has not yet given, although several useful papers have been published toward this

CHIRPING EFFECT

– Simultaneous Phase and Intensity Modulation

$$\alpha_c = \frac{\Delta\mu(\text{real})}{\Delta\mu(\text{imag.})} = 2\,\frac{\Delta\phi}{\Delta\alpha L}$$

Example: $\Delta\phi=\pi$

$\Delta\alpha L=2.3$ (10dB ON/OFF)

→ $\alpha_c=2.7$

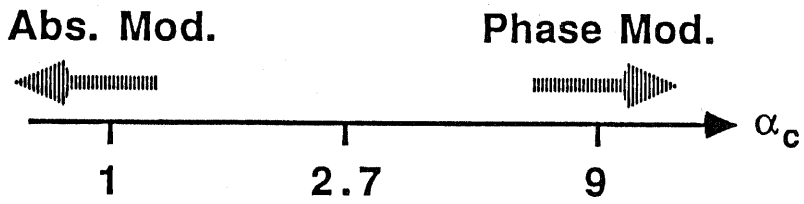

Fig. 1.2 Use of a chirp parameter as a figure of merit for the absorption and phase modulators.

goal. A theoretical analysis for a *P-i-N* electro-optic modulator was done by Marshall and Katz [10], in terms of the LEO and carrier-induced effects. Also, Adams *et al.* reported on the optimum overlap of electric and optical fields in waveguide devices [11]. A more complete theory that is able to account for the experimentally measured index and hence phase shifts was not available until very recently, when J. G. Mendosa-Alvarez *et al.* has reported based on their depletion edge translation lightwave modulators [12].

The table 1-I briefly summarizes the four main effects, which have been commonly used in the index or absorption modulation in optical waveguides to date. These are the field-induced linear electro-optic (LEO) [13], and the electro-refraction (ER) due to the Franz-Keldysh electro-absorption [14] effects, and the carrier-induced plasma dispersion (PL) [15] and the band-filling (BF) or Burstein-Moss shift [16] effects. For light of 1.06 μm or longer wavelength propagating along the optical waveguide, the LEO effect will give the major contribution for the index (or absorption) change, followed by the BF, ER, and PL in the given order of decreasing importance, respectively. However, for wavelengths very close to the absorption edge, the ER and BF effects will dominate. Also should be noted is the effect known as the quantum-confined Stark effect (QCSE), which is observed in a quantum well structure of a semiconductor material [17], [18]. (The application of the QCSE effect has opened up a new branch for the optical modulation and has attracted much activity in the last several years, however, the details are left for other literatures here.) Out of these major effects, this dissertation concentrates on the use of the BF and PL effects to the index and absorption modulation at a light wavelength close to the absorption edge, and which can be obtained with injection and/or removal of free carriers;

(i) Plasma effect (PL)

The plasma effect is due to the free carrier absorption either in the conduction or valence bands of the semiconductor. The absorption of a photon by a free carrier (electron or hole) in the band implies the transition to higher-energy states in the same band, and requires some interaction to satisfy the requirement of momentum conservation. The additional momentum can be provided by lattice interaction via photons or by scattering with ionized impurities. Because transitions inside the same band usually involve small energy changes, free carrier absorption has an important contribution to the overall absorption spectra for longer wavelengths below the bandgap energy, and somewhat smaller contributions for wavelengths close to the band-edge. As with the other effects, free carrier absorption will induce a corresponding refractive index variation $\Delta\mu$(PL). An expression assumed to approximate $\Delta\mu$(PL) [15] is as formulated in Table 1-I.

Table 1-I Comparison of various effects used for changing the index of refraction in optical modulators and switches.

Effect	Abb.	Field or Carrier density	$\Delta\mu$ (10^{-3}) @0.89 μm $\mu_0 = 3.60$	$\Delta\mu$ (10^{-3}) @1.06 μm $\mu_0 = 3.48$
a) Electro-optic	LEO	250 kV/cm	0.93	0.63
b) Electro-refraction	ER	250 kV/cm	1.52	0.27
c) Plasma	PL	1×10^{17} cm^{-3}	0.15	0.22
d) Band-filling	BF	1×10^{17} cm^{-3}	1.25	...

a) For a field $E_z \perp$ (001) plane,

$$\left|\Delta \mu_{x,y} \text{ (LEO)}\right| = \frac{1}{2}\mu_0^3 r_{41} E_z$$

where $r_{41} = 1.6\times10^{-10}$ cm/V at $\lambda = 0.89$ μm, and 1.2×10^{-10} cm/V at $\lambda = 1.06$ μm were assumed, respectively. (After reference [13])

b) $\Delta\mu(\text{ER}) \approx A(\lambda)\, E^2$

$$= 3.45\times10^{-16} \exp\left[3 / \lambda^3\right] E^2 \quad \text{for } \lambda = 0.9\text{–}1.5 \text{ μm}$$

where λ is in units of μm. (After reference [14])

c) $$\Delta\mu \text{ (PL)} = -\frac{q^2 \lambda^2}{8\pi^2 c^2 \varepsilon_0 \mu_0}\left[\frac{\Delta n}{m_e^*} + \frac{\Delta p}{m_h^*}\right]$$

$$\approx 6.67\times10^{-21}\, \lambda^2\, \Delta n / \mu_0 \qquad \text{for electron injection}$$

where λ and Δn are in units of μm and cm^{-3}, respectively. (After reference [15])

d) This work. (c.f. Chapter 3)

(ii) Band-filling effect (BF)

When the carriers are injected into a semiconductor material, the absorption coefficient will change from that of an intrinsic material to that of a doped material. For example, in a undoped material as illustrated in Fig. 1.3(a), when the carriers (electrons) are injected, the conduction band fills its energy states with the consequent moving of the Fermi level up toward the conduction band-edge. As a result, the fundamental absorption edge will shift to higher energies as illustrated in Fig. 1.3(b), producing a negative increment of $\Delta\alpha$(BF) of the absorption in the region where the carriers have been injected.

The negative absorption variation due to the band-filling will induce a negative refractive index change $\Delta\mu$(BF) for energies below the band-gap as can be clearly seen from the Kramers-Kronig relationship between $\Delta\alpha$ and $\Delta\mu$;

$$\Delta\mu(E) = \frac{hc}{\pi}\int_0^{\infty} \frac{\Delta\alpha(E')}{E'^2 - E^2}\,dE' \tag{1-1}$$

so that,

$$\Delta\mu(\mathrm{BF}) \approx \mathrm{B}(\lambda)\,\Delta n \tag{1-2}$$

where Δn is the injected carrier density and B is the proportionality constant which depends on the wavelength λ, respectively.

These carrier-induced changes can be larger than those changes expected from the electro-optic effect as can be seen from Table 1-I. Furthermore, the carrier-induced index changes are not dependent on the polarization of the optical input, unlike the case of the electro-optic changes, which in fact, exhibit a strong polarization dependence. The above features make it more attractive to use the free-carrier effects to realize polarization-independent optical modulators and switches with greatly reduced device dimensions (on the order of a few hundred microns or less), which are very useful and advantageous in constructing compact optical network systems using single-mode optical fibers.

Optical modulators and switches with *pn* (*p-i-n*) structures, whose operations are based on the application of the carrier-induced variations of the absorption coefficient and/or the refractive index have been recently reported. For example, simple *pn* (*p-i-n*) structured carrier-injected X-switches using Si

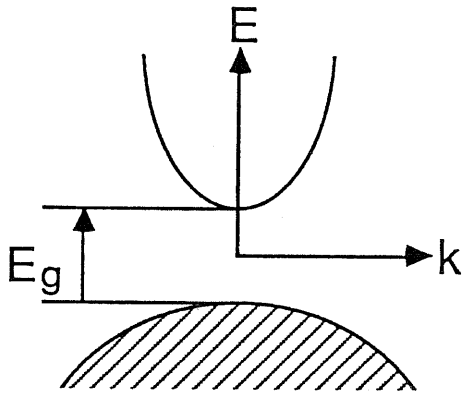

(a) Before Carrier Injection

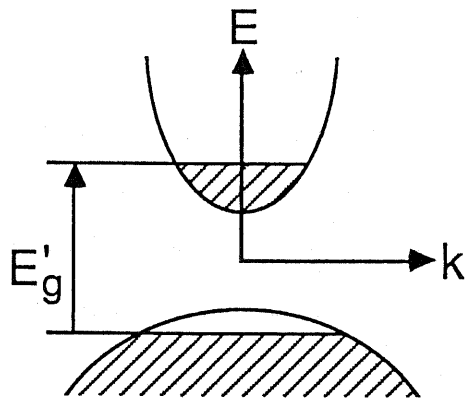

(b) After Carrier Injection

Fig. 1.3 An illustration showing the effect of band-filling in semiconductors.

[19], and InP/InGaAsP [20]–[22], as well as integrated 4×4 matrix arrays [23] have been demonstrated. These switches have also been monolithically integrated with buried heterostructure (BH) DFB lasers [24].

However, the switching times of such diode-structured optical switches are most often limited by the lifetime of the injected carriers and are, for example, on the order of several to 10 ns in GaAs. If a bipolar transistor structure is employed with the injection of carriers into its base, then the methods such as a fast-rate removal of stored excess carriers by reverse biasing the base-collector junction, which are frequently applied in practical transistor circuits for high-speed current switching, can also be applied for optical switching at high speeds. The amplification nature of the transistors also means that large emitter (or collector) currents can be controlled by small base currents. Therefore, small driving power is needed to drive this type of three terminal device.

All of these have led to a proposal and consideration of a bipolar transistor carrier-injected optical modulator/switch using a GaAs/AlGaAs double heterostructure (DH) waveguide structure, which is described fully in Chapter 2. Furthermore, the linear relationship between the index change $\Delta\mu$(BF) and the carrier density Δn given in Eq. (1-2) will be valid for both n-type and p-type GaAs and for N-type and P-type AlGaAs with the proper B-constants as long as the semiconductors are lightly-doped ($\leq 5\times10^{17}$ cm^{-3}). For highly-doped material, the parabolic band model will no longer be valid and band tails in the densities of states should also be considered; besides, in this regime, the band-gap shrinkage due to carrier-to-carrier interaction will be considerable, and give an index variation which opposes the one from the band-filling effect. The above considerations have led to a full theoretical analysis of the effects of free carrier injection on the variations of the absorption and index of refraction in GaAs as will be presented fully in Chapter 3. Also in Chapter 3, the chirp parameters are also discussed. In Chapter 4, an emphasis is placed on the process technology employed for the fabrication of a GaAs/AlGaAs double-heterojunction bipolar transistor (DHBT) waveguide structure carrier-injected optical intensity modulator/switch grown by MBE, and on the characterization of the device performance, particularly the electrical properties and optical modulation characteristics of the DHBT waveguide structure. The results are also applied to design, compute, and analyze the characteristics expected for a reflection-type optical switch, as proposed in Chapter 2. In Chapter 5, a technological improvement has been searched for producing low ohmic contact resistance to n-type GaAs by using a non-alloyed ohmic contact, namely, graded $In_xGa_{1-x}As$ layer, in order to achieve ultra-fast switching speeds of the proposed device structure. Chapter 6 summarizes the contents of this dissertation and gives future directions in the field of integrated

optics, which the author has been engaged for the past several years for this dissertation.

References

[1] G. A. Vawter, "Monolithically integrated transverse junction stripe lasers in GaAs/AlGaAs for optical interconnects", *ph.D Dissertation, Department of Electrical and Computer Engineering, University of California, Santa Barbara*, October, 1987.

[2] H. Takeuchi, K. Kasaya, Y. Kondo, H. Yasaka, K. Oe, and Y. Imamura "Monolithic integrated optical circuit for coherent detection", *Technical Digest of the 7th. International Conference on Integrated Optics and Optical Fiber Communication*, Kobe, PDB-6, p. 48, 1989.

[3] S. Kinoshita and K. Iga, "Circular buried heterostructure (CBH) GaAlAs/GaAs surface emitting laser", *IEEE J. Quantum Electron.*, vol. QE-23, p. 882, 1987.

[4] R. G. Hunsperger, *Integrated Optics: Theory and Technology*, Spring-Verlag, New York, 1982.

[5] J. L. Merz, R. A. Logan, and A. N. Sergent, "GaAs integrated optical circuits by wet chemical etching", *IEEE J. Quantum Electron.*, vol. QE-15, p. 72, 1979.

[6] F. J. Leonberger, "High-speed operation of $LiNbO_3$ electro-optic interferometric waveguide modulators", *Opt. Lett.*, vol. 5, p. 312, 1980.

[7] R. C. Alferness, "Waveguide electro-optic modulators", *IEEE Trans. Microwave Theory and Tech.*, vol. MTT-30, p. 1121, 1983.

[8] T. H. Wood, C. A. Burrus, D. A. B. Miller, D. S. Chelma, T. C. Damen, A. C. Gossard, and W. Wiegmann, "131 ps optical modulation in semiconductor multiple quantum wells (MQW's)", *IEEE J. Quantum Electron.*, vol. QE-21, p. 117, 1985.

[9] F. Koyama and K. Iga, "Frequency chirping of external modulation and its reduction", *Electron. Lett.*, vol. 21, p. 1065, 1985.

[10] W. K. Marshall and J. Katz, "Waveguide *P-i-N* junction electrooptic modulators: theoretical analysis and design criteria", *Appl. Opt.*, vol. 24, p. 1996, 1985.

[11] M. J. Adams, S. Ritchie, and M. J. Robertson, "Optimum overlap of electric and optical fields in semiconductor waveguide devices", *Appl. Phys., Lett.*, vol. 48, p. 820, 1986.

[12] J. G. Mendoza-Alvarez, L. A. Coldren, A. Alping, R-H. Yan, T. Hausken, K. Lee, and K. Pedrotti, "Analysis of depletion edge translation lightwave modulators", *J. Lightwave Tech.*, vol. 6, p. 793, 1988.

[13] A. Yariv and P. Yeh, Optical Waves in Crystals, John Wiley & Sons, New York, 1984.

[14] A. Alping and L. A. Coldren, "Electrorefraction in GaAs and InGaAsP and its application to phase modulators", *J. Appl. Phys.*, vol. 61, p. 2430, 1987.

[15] J. Pankove, *Optical Processes in Semiconductors*, Dover, New York, 1975.

[16] J. Manning, R. Olshansky, and C. B. Su, "The carrier-induced index change in AlGaAs and 1.3 μm InGaAsP diode lasers", *IEEE J. Quantum Electron.*, vol. QE-19, p. 1525, 1983.

[17] T. H. Wood, "Multiple quantum well (MQW) waveguide modulators", *J. Lightwave Tech.*, vol. 6, p. 743, 1988.

[18] Y. Kan, H. Nagai, M. Yamanishi, and I. Suemune, "Field effects on the refractive index and absorption coefficient in AlGaAs quantum well structures and their feasibility for electrooptic device applications", *IEEE J. Quantum Electron.*, vol. QE-23, p. 2167, 1987.

[19] J. P. Lorenzo and R. A. Soref, "1.3 μm electro-optic silicon switch", *Appl. Phys. Lett.*, vol. 51, p. 6, 1987.

[20] O. Mikami and H. Nakagome, "Waveguided optical switch in InGaAsP/InP using free carrier plasma absorption", *Electron. Lett.*, vol. 20, p. 228, 1984.

[21] O. Mikami and H. Nakagome, "InGaAsP/InP optical waveguide switch operated by a carrier-induced change in the refractive index", *Opt. Quantum Electron.*, vol. 17, p. 449, 1985.

[22] K. Ishida, H. Nakamura, H. Matsumura, T. Kadoi, and H. Inoue, "InGaAsP/InP optical switches using carrier induced refractive index change", *Appl. Phys. Lett.*, vol. 50, p. 141, 1987.

[23] H. Inoue, H. Nakamura, Y. Sasaki, T. Katsuyama, N. Chinone, and K. Morosawa, "Eight-millimeter long nonblocking 4×4 optical switch array", *Technical Digest of the 8th. CLEO*, TUK1, Anaheim, 1988.

[24] S. Sakano, H. Inoue, H. Nakamura, T. Katsuyama, and H. Matsumura, "InGaAsP/InP monolithic integrated circuit with lasers and an optical switch", *Electron. Lett.*, vol. 22, p. 594, 1986.

CHAPTER 2

GaAs/AlGaAs HETEROJUNCTION BIPOLAR TRANSISTOR CARRIER-INJECTED OPTICAL MODULATOR/SWITCH

2.1 Introduction

Until recently, most of the optical modulators and switches fabricated either in discrete or integrated forms, using either dielectric materials such as $LiNbO_3$ and $LiTaO_3$, or semiconductors such as GaAs/AlGaAs and InGaAsP/InP III-V compound system, are characterized by an efficient use of the first-order electro-optic effect as the main scheme of modulation/switching method. These devices, however, resulted in relatively large physical sizes (typical device length > ~1 mm), in order to obtain reasonable characteristics. Large sizes will limit the possible high-density integration of these kinds of devices on a single chip, and also result in larger capacitance which will ultimately limit the high-frequency operation.

It has been known, however, that very large changes in the absorption coefficient and refractive index can be obtained in semiconductor materials by the injection of free carriers [1]–[5], primarily because of the band-filling effect or Burstein-Moss shift effect, and these carrier-induced changes can be larger than those changes expected from the electro-optic effect. Furthermore, the carrier-induced index changes are not dependent on the polarization of the optical input [7]–[8], unlike the case of the electro-optic changes, which in fact, exhibit a strong polarization dependence. The above features make it more attractive to use the free-carrier effects to realize polarization-independent optical modulators and switches with greatly reduced device dimensions (on the order of a few hundred microns or less), which are very useful and advantageous in constructing compact optical network systems using single-mode optical fibers.

Optical modulators and switches with *pn* (*p-i-n*) structures, whose operations are based on the application of the carrier-induced variations of the absorption coefficient and/or the refractive index have been recently reported. For example, simple *pn* (*p-i-n*) structured carrier-injected X-switches using Si [6], and InP/InGaAsP [7]–[9], as well as integrated 4×4 matrix arrays [10] have been demonstrated. These switches have also been monolithically integrated with buried heterostructure (BH) DFB lasers [11].

However, the switching times of such diode-structured optical switches are most often limited by the lifetime of the injected carriers and are, for example, on the order of 10 ~ 100 ns in GaAs. If a bipolar

transistor structure is employed with the injection of carriers into its base, then the methods such as a fast-rate removal of stored excess carriers by reverse biasing the base-collector junction, which are frequently applied in practical transistor circuits for high-speed current switching, can also be applied for optical switching at high speeds. The amplification nature of the transistors also means that large emitter (or collector) currents can be controlled by small base currents.

In this chapter, the first Bipolar Transistor Carrier-Injected Optical Modulator/Switch using a GaAs/AlGaAs double heterostructure (DH) structure is proposed and analyzed, which is expected to improve the overall performance of the optical modulators and switches operated by the free-carrier injection.

2.2 Single-Mode Guiding in GaAs/AlGaAs DH Waveguide Structures

2.2.1 Method of Effective Refractive Index [12]

The electric field E travelling in the z-direction in a dielectric waveguide is often characterized by a scalar wave equation,

$$\nabla_{tr}^2 E + (\mu^2 k_0^2 - \beta^2) E = 0 \tag{2-1}$$

where the suffix tr means in the transverse plane, k_0 is the wave number in free space, μ is the refractive index of the propagating medium, and β is the propagation constant. For the wave propagation, we also assume exp[i $(w\,t - \beta\,z)$] dependence . For a slab waveguide with m layers, as illustrated in Fig. 2.1, Eq. (2-1) can be reduced in dimension to,

$$\frac{d^2\Psi(x)}{dx^2} + (\mu_j^2 k_0^2 - \beta^2) \Psi(x) = 0 \qquad j = 1,2,.....m \tag{2-2}$$

A general solution to Eq. (2-2) is then given by,

$$\Psi(x) = A_j \exp(ik_{xj}x) + B_j \exp(-ik_{xj}x) \tag{2-3a}$$

$$k_{xj} = (\mu_j^2 k_0^2 - \beta^2)^{1/2} = (\beta_j^2 - \beta^2)^{1/2} \tag{2-3b}$$

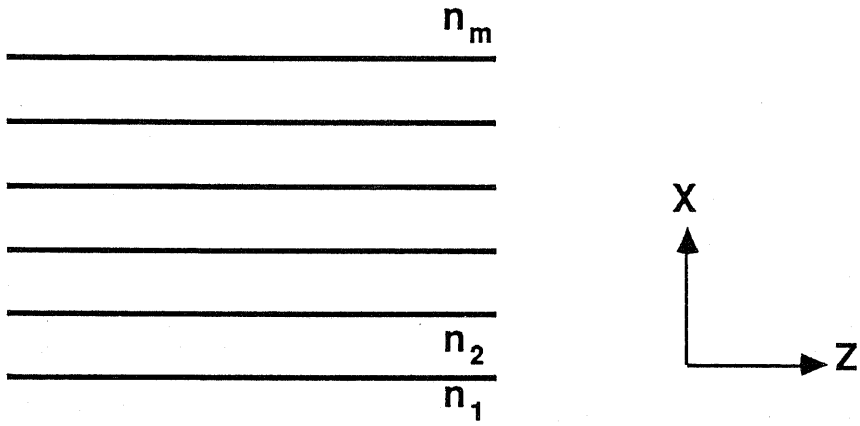

Fig. 2.1 An m-layer slab waveguide structure considered for the analysis.

The constants A_j, B_j, and β are determined from the boundary conditions. For the TE modes, the boundary conditions at a dielectric interface require the continuity of E_y and H_z components, corresponding to the continuity of $\Psi(x)$ and $\Psi'(x)$. k_{xj} takes an imaginary value where the field in layer j is evanescent, i.e. in layer 1 and m as shown in Fig. 2.1.

For an exact treatment of any stripe (or ridged) waveguides, a two dimensional analysis of Eq. (2-1) is necessary, but for most cases, $(d^2 / dx^2) >> (d^2 / dy^2)$, and therefore we can consider the region I and II as shown in Fig. 2.2, as two independent slab waveguides. Eq. (2-1) can then be modified to determine the field distribution in the y-direction as,

$$\frac{d^2\Psi(y)}{dy^2} + (\mu_{ej}^2 k_0^2 - \beta^2)\Psi(y) = 0 \qquad j = \text{I, II} \tag{2-4}$$

where $\mu_{ej}{}^2 k_0{}^2 = \beta_j{}^2$, and μ_{ej} represents the effective refractive index in region j, also shown in Fig. 2.2. A solution to Eq. (2-4) can be obtained in just the same way as for Eq. (2-2), however, the boundary conditions are now different. Since the wave-guiding is dominated by the slab waveguide in the x-direction (lateral), the polarization of the wave will not vary greatly and the electric field E_y is nearly perpendicular to the interface between region I and II. Thus, strictly speaking, the continuity of εE_y rather than E_y should be used as the boundary conditions. However, the difference in material permittivity $\Delta\varepsilon$ between the region I and II is usually very small, which makes it valid to use the same kind of boundary conditions in this case, i.e. the continuity of $\Psi(y)$ and $\Psi'(y)$.

By considering the given stripe structure as a symmetrical slab waveguide in the y-direction (transverse), the cut-off stripe width W_{co} for the *mth*-order TE mode is given by,

$$W_{co} = (m\,\lambda / 2)\,(\mu_{e_{II}}{}^2 - \mu_{e_I}{}^2)^{-1/2} \tag{2-5}$$

2.2.2 Numerical Analysis

Based on the theory briefly described in Sec. 2.2.1, a relationship between the cut-off stripe width W_{co}, and the stripe height t for a specific single-mode GaAs/AlGaAs DH stripe-waveguide structure, as shown in Fig. 2.3, is calculated. The values of the refractive index at λ = 890 nm (E =

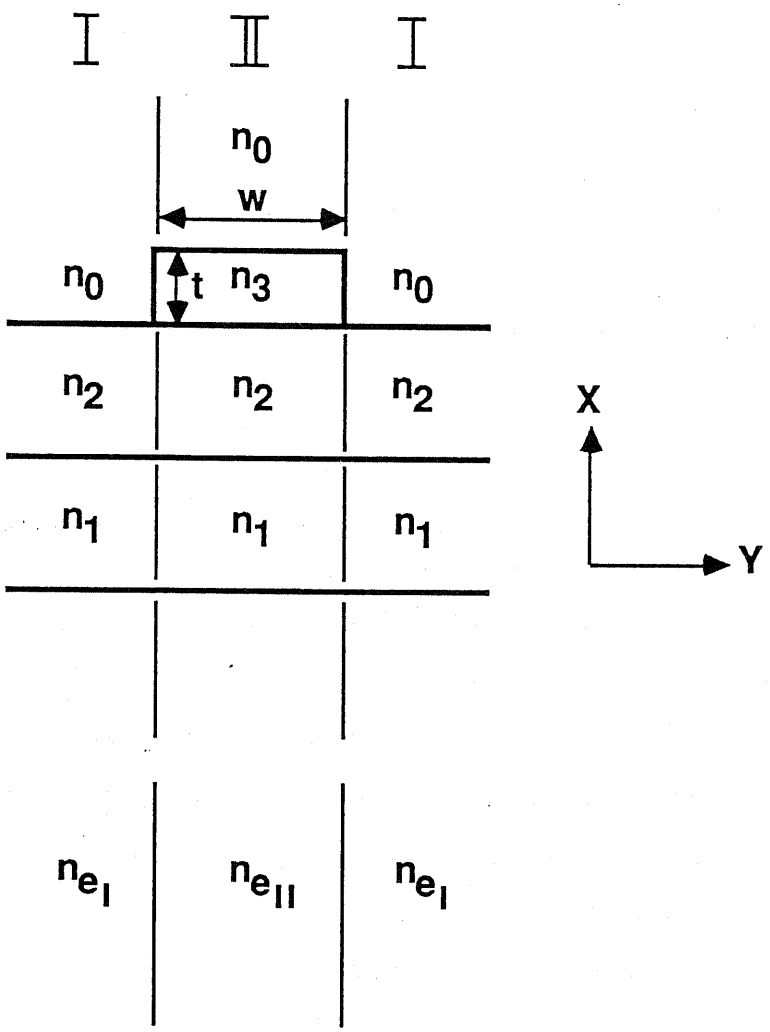

Fig. 2.2 A stripe waveguide structure considered for the analysis.

1.39 eV) for each layer are determined from the following equations [13],

$$\mu = 3.60\ (1 - 5.424\times10^{-22}\ n\ ) \qquad \text{for } n\text{-type GaAs} \qquad (2\text{-}6a)$$

$$\mu = 3.60\ (1 - 8.001\times10^{-23}\ p\ ) \qquad \text{for } p\text{-type GaAs} \qquad (2\text{-}6b)$$

$$\mu = 3.60\ (1 - 5.424\times10^{-22}\ N\ )\ (1 - x\ /\ 7) \qquad \text{for } N\text{-type } Al_xGa_{1-x}As \qquad (2\text{-}6c)$$

$$\mu = 3.60\ (1 - 8.001\times10^{-23}\ P\ )\ (1 - x\ /\ 7) \qquad \text{for } P\text{-type } Al_xGa_{1-x}As \qquad (2\text{-}6d)$$

where n, p, N, or P are the carrier densities in each layer, and x is the aluminum content. The effective refractive index for the region I and II are determined numerically by solving Eq. (2-4). Having calculated μ_{e_I} and $\mu_{e_{II}}$ for a given stripe height t, we can then determine the maximum cut-off stripe width W_{co} allowable for a single fundamental lateral mode wave-guiding, using Eq. (2-5).

Figure 2.4 shows the calculated relationship between the stripe height t and the cut-off stripe width W_{co} for the first-order TE-mode, obtained for the waveguide structure as shown in Fig. 2.3. It can be observed that W_{co} is a sensitive function of the height t. If the mesa etching of the region I, whether chemical or plasma-related etching such as the reactive ion etching (RIE), is not sufficient, then the wave-guiding of the fundamental TE_0-mode will be weak. On the other hand, if over-etched, then the mode confinement will be too strong and the higher-order modes are also likely to be excited. Therefore in theory, the two parameters should be carefully controlled to accomplish a complete single-mode guiding. In practice, however, the higher-order modes have much higher attenuation constants, and hence, will be attenuated quickly in a relatively short distance of propagation [14]. Thus, a "quasi" single-mode guiding may be achieved even in a moderately over-etched *multimode* stripe waveguide.

2.3 Proposal of GaAs/AlGaAs Heterojunction Bipolar Transistor Carrier-Injected Optical Modulator/Switch

In view of easier fabrication of the device, it is most convenient for the optical waveguides and heterojunction bipolar transistor (HBT) of a Bipolar Transistor Carrier-Injected optical Modulator/Switch to have the same or very similar layer structures. At first, we consider both the design constraints for an optimum device structure; one imposed by the design principles for optical waveguides and the other imposed by those for HBT's.

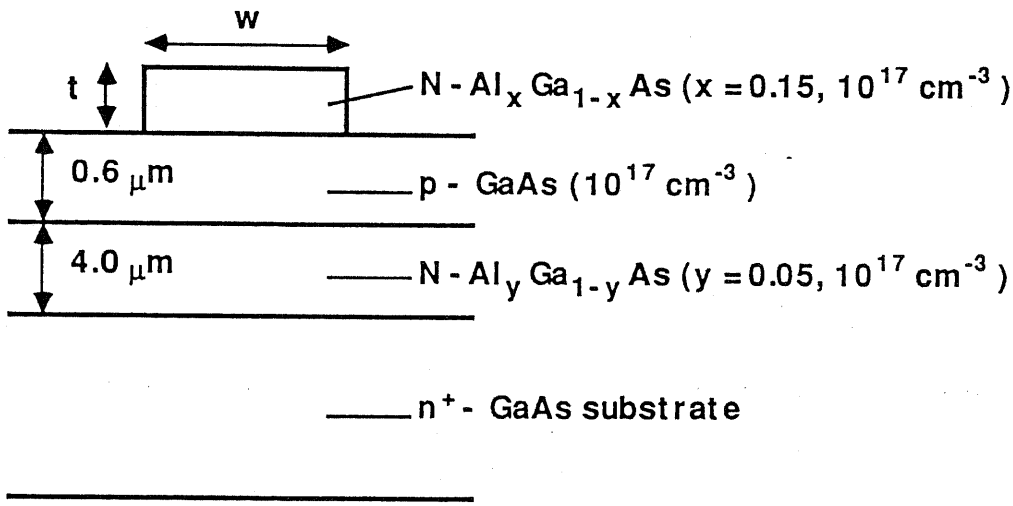

Fig. 2.3 An example of a stripe waveguide structure with numerical values used for the analysis.

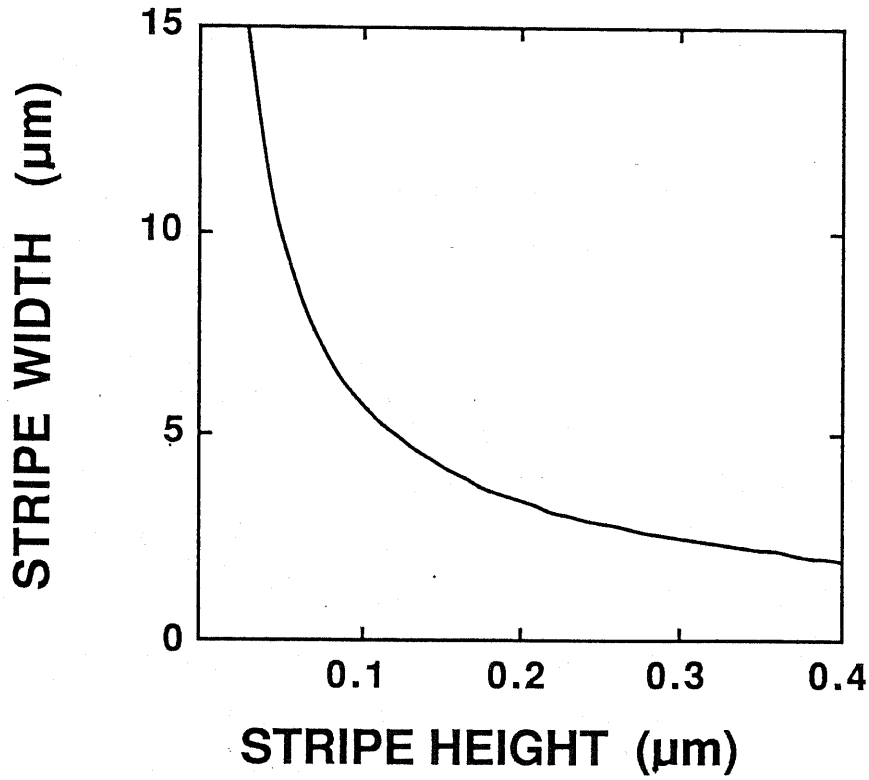

Fig. 2.4 Calculated relationship between the height t and cut-off width w.

(A) Basic Design Principles for Optical Waveguides

(i) A complete single-mode index guiding of the propagating optical wave is achieved through the use of a GaAs/AlGaAs material system with a double heterostructure (DH) stripe configuration.

(ii) Optical wavelength of $\lambda = 890$ nm ($E = 1.39$ eV) is chosen for the optical input on the basis of the experimental data on the carrier-induced variations of the refractive index $\Delta\mu$ in the active layer of a GaAs/AlGaAs DH laser diode, measured by Henry *et al.*[1]. Here, we use,

$$\Delta\mu \approx - \ 0.024\times10^{-18}\ \Delta n \tag{2-7}$$

where the injected carrier density Δn is in units of cm^{-3}. A more detailed theoretical analysis on the variations of the absorption coefficient and the refractive index due to free carrier injection is described in the next chapter.

(iii) Each layer of the cladding, the buffer, and especially the waveguide layer should be designed to have the lowest possible impurity doping density in order to minimize the absorption loss by the free carriers and the scattering loss. Typically, the doping level of $< 10^{16}$ cm^{-3} is desired in practice.

(iv) A strong confinement of the mode(s) in the lateral direction, where the GaAs waveguide layer is sandwiched between the two AlGaAs layers with a high aluminum composition, may cause significant non-linear effects and increased scattering, which also depends on the "layer-quality" of the epitaxial growth. Furthermore, it necessitates the waveguides to have narrow lateral widths for the required complete single-mode wave-guiding. Therefore, the waveguide thickness of 0.5 ~ 2.0 μm range and the aluminum composition of 0.05 ~ 0.25 for the cladding and buffer layers are taken as reasonable values.

(B) Basic Design Principles of HBT's

(i) An HBT structure is achieved through the use of a GaAs/AlGaAs material system with a wide-gap emitter. The considerable benefits of the HBT structure have been proposed as early as in 1957 by Kroemer [15] and well reviewed recently by the same author [16], and hence are not discussed here but to mention the least that the HBT structure is a preferred approach in the domain of high-speed electron devices [17], *as well as* optical devices. For example, HBT structures have been recently applied to active optical devices such as laser transistors [18].

(ii) The impurity doping density of the emitter is selected to minimize the emitter capacitance, and yet to provide the necessary current densities without ohmic drops or current saturation. The aluminum fraction

x is chosen so that the carrier injection from the base into the emitter is minimal. Typically, $x = 0.2 \sim 0.3$ is often used in practice.

(iii) An abrupt emitter-base interface is assumed, which gives rise to a "spike" in the conduction band energy profile. Though this spike decreases the collector current and the emitter injection efficiency due to an increased recombination at the junction interface, it can provide injection of high-velocity electrons into the base, thereby reducing the transit time across the base [16]. The base thickness of 0.1 ~ 0.3 μm is often desired for high current gain and high frequency operation.

(iv) Optimum values of impurity doping densities in the base and collector must be searched in order to minimize the depletion layer capacitance C_{ct}, and external base resistance R_B, i.e. in order to reduce the collector time constant $R_B C_{ct}$, and to prevent early punch-through effects.

Figure 2.5 shows just one example of our proposal as applied to a DH-TIR (Total Internal Reflection) X-switch. A single fundamental mode is supported and guided through an n-GaAs layer (10^{17} cm^{-3} and 0.6 μm thick), which is placed between an N-$Al_{0.15}Ga_{0.85}As$ cladding layer (10^{17} cm^{-3} and 0.2 μm thick) and an N-$Al_{0.05}Ga_{0.95}As$ buffer layer (10^{17} cm^{-3} and 4 μm thick). An N-p-N GaAs/AlGaAs HBT is formed around the intersecting region of the two single-mode waveguides of 4 μm in width, which has been determined from Fig. 2.4. Here, a part of the n-GaAs waveguide layer and N-$Al_{0.15}Ga_{0.85}As$ cladding layer are converted into p-type to form the base region of the bipolar transistor. The optical field/power distributions of the TE_0-like mode in the transverse direction and the vertical direction of the waveguide structure are determined using the method of effective refractive index as described in Sec. 2.2, and the results are as shown in Fig. 2.6.

The basic operation principle of the proposed device is as follows; A guided wave excited in one of the input waveguide arms, as indicated in Fig. 2.5, propagates straight and appears at an output port 1 with optical power L_1, if no carriers were injected in the switching region. When the carriers are gradually injected into the waveguide/base region, then the refractive index of the given region starts to decrease primarily because of the band-filling effect, and the guided wave starts to get reflected by total internal reflection [19]. Some of the optical power then appear at the other output arm with L_2, until all the power is eventually switched to the port 2.

An inverse relationship between the switch length and intersecting angle θ is shown in Fig. 2.7. For $\theta = 4°$, the switch length is ~ 110 μm, which is considerably smaller than the common directional coupler-type geometry, whose switch lengths are typically in the range, 1 ~ 5 mm. The optical switching

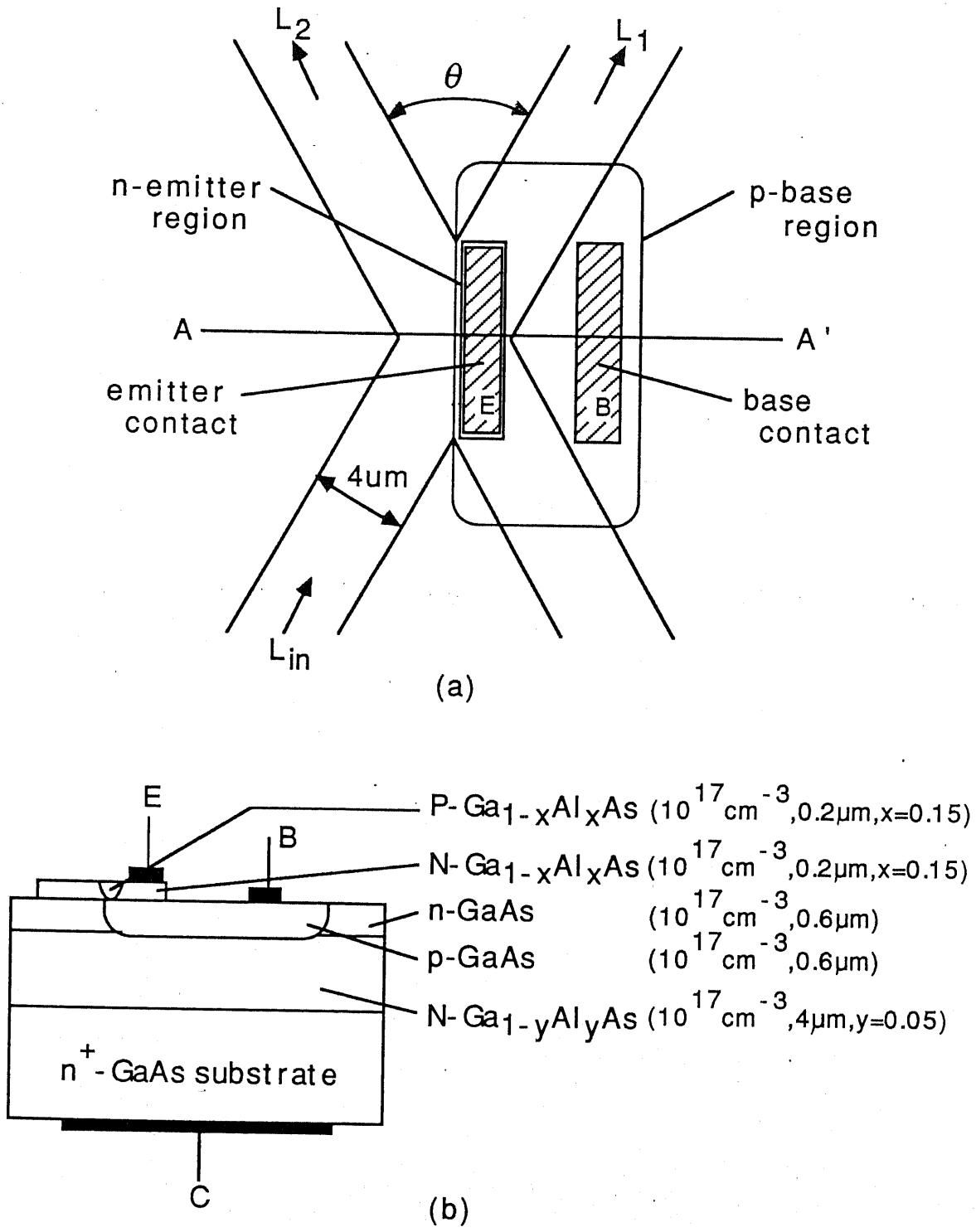

Fig. 2.5 An example of Bipolar Transistor Carrier-Injected Optical Switch, as applied to a double-heterostructure (DH) X-crossing; (a) overview, and (b) AA' cross-section.

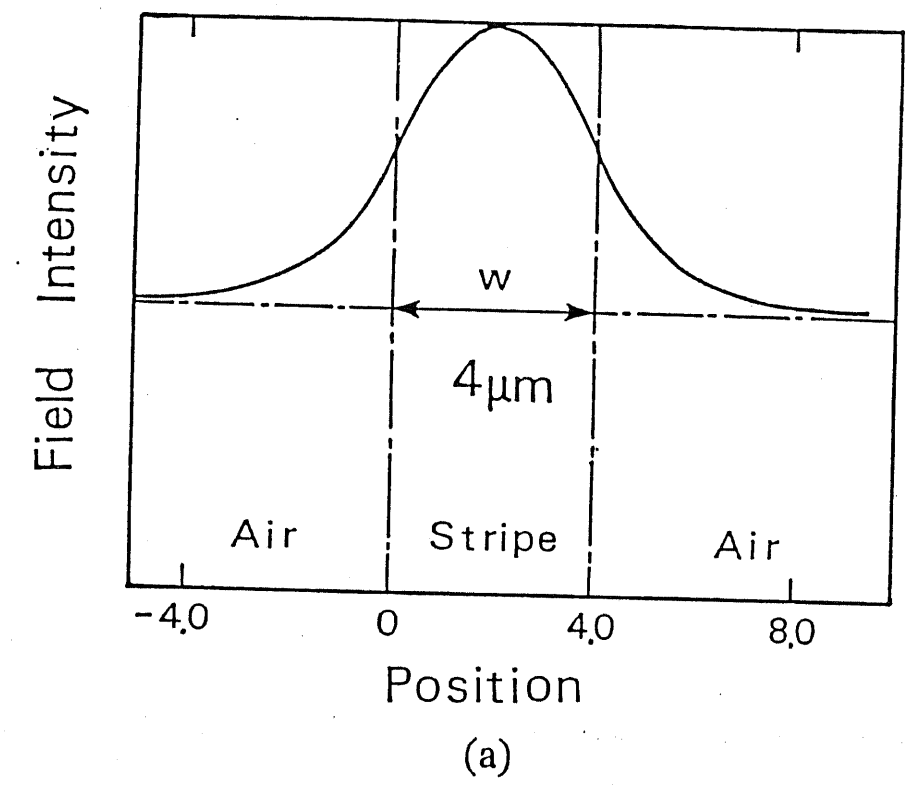

(a)

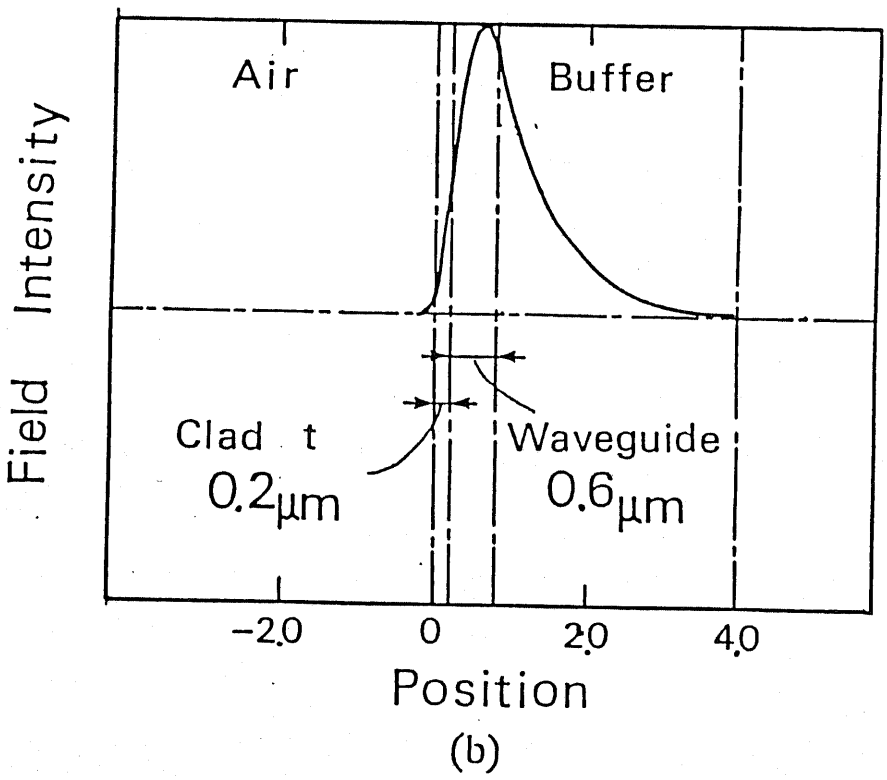

(b)

Figure 2.6 Calculated optical field/power distribution of the mode supported in; (a) transverse direction, and (b) vertical direction.

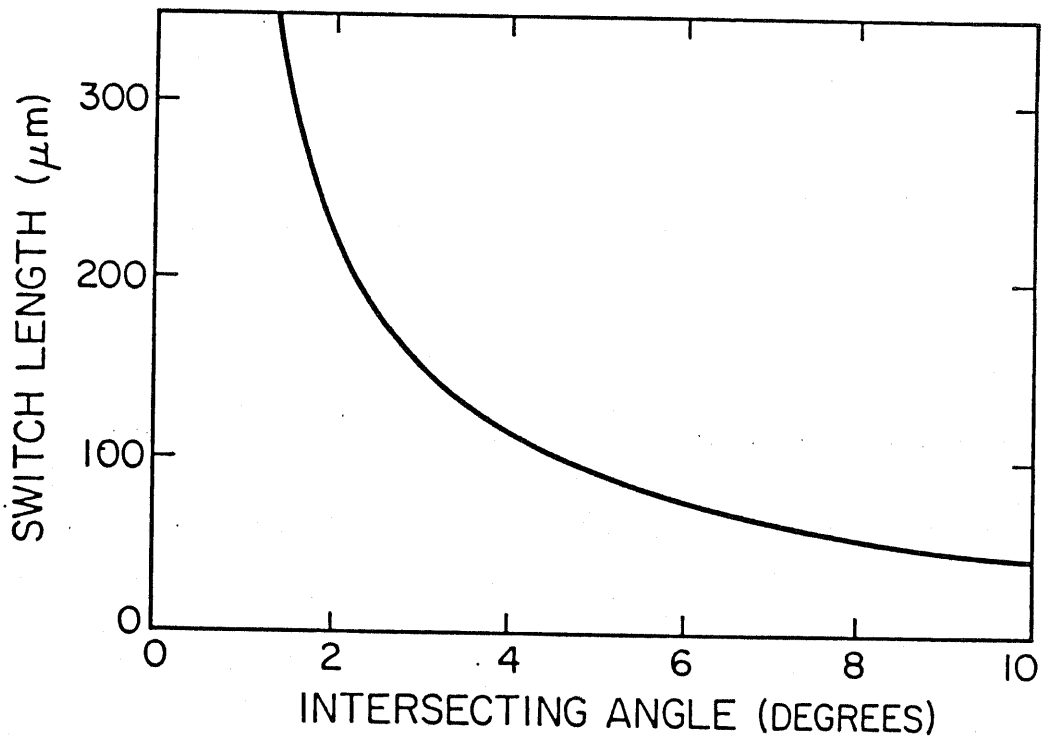

Fig. 2.7 Calculated relationship between the switch length and intersecting angle θ.

characteristics for different values of θ are theoretically determined and discussed in the next section.

One major claimed disadvantage, which is an inherent characteristics of this kind of device that operates in the vicinity of the band-gap energy, is the significant loss of the light power due to the band-to-band optical absorption. The measured absorption loss for $\lambda \approx 890$ nm ($E \approx 1.39$ eV) is ~ 40 dB/cm [20]. If the device length is made shorter than 1 mm in total, then the absorption loss may be significantly reduced to ~ 3 dB. A more detailed theoretical analysis and discussion regarding the question of absorption losses are presented in the next chapter.

2.4 Theoretical Analysis of The Device Switching Characteristics

2.4.1 Optical Switching Characteristics

Two dimensional beam propagation method (BPM) [21]–[23] is applied to determine the behavior of mode propagation and the switching characteristics of the proposed X-structure as of Fig. 2.5. The Fourier transform required for the BPM method is accomplished using a standard subroutine in Tokyo University Computer Centre Mathematical Subroutine Library MSL II. The assumed parameters for the analysis are as follows;

(i) A TE_0-like mode is excited in one of the two input single-mode waveguide arms. The wavelength of the guided mode is assumed to be $\lambda = 890$ nm ($E = 1.39$ eV).

(ii) The total device length is 800 μm. This means that for $\theta = 4°$, the separation of the waveguide arms at the both ends of the device is ~ 30 μm, which should be sufficient, for example, to place and separate the two single-mode fibers at the both ends.

(iii) Negative changes in the refractive index are caused in the waveguide/base region as a result of electron injection for the given wavelength. The index variations are attributed primarily to the carrier-induced shift of the fundamental absorption edge, i.e. band-filling effect or Burstein-Moss shift. The amount of index variation is estimated using the results written in Eq. (2-7).

(iv) The transistor is assumed to operate in its active state when fully turned on. This means that the distribution of the injected minority carriers will be at a maximum at the emitter end of the base region, decreasing nearly *linearly* to zero at the collector end, where the carriers are removed by the electric field that is set up across the base-collector reverse biased junction. Since the carrier-induced index variations

also vary accordingly with distance in the waveguide/base layer, a fully three dimensional BPM analysis is necessary for an exact treatment of the mode propagation. In order to reduce the problem to a two dimensional one without much loss of accuracy and to save the running time of computation, an *average* value of the carrier density and hence the refractive index in the base/waveguide region are considered.

(v) The transistor emitter current is given by [24]–[25],

$$I_E = Q_B / \tau_B \tag{2-8}$$

where I_E is the emitter current, Q_B = average carrier charge in the base, and τ_B is the minority carrier lifetime in the base. If the transistor is driven in the active state, then τ_B equals the transit time τ_T for the minority carriers to diffuse across the base width w, and it is given by,

$$\tau_B = \tau_T = w^2 / 2D \qquad \text{(active state)} \tag{2-9}$$

where D is the diffusion constant of the minority carriers in the base. For $D = D_n \approx 85$ cm^2/sec and w = 0.6 μm, we obtain $\tau_T \approx 21$ ps.

(vi) Internal losses such as optical absorption by the free carriers and band-to-band optical transitions are not included in the loss calculations here, however, they are treated in detail in the next chapter. The term used here only accounts for optical *radiative losses* (*not* to be confused with *radiative recombination*).

The switching characteristics for different values of the intersecting angle θ are evaluated using the BPM method. For $\theta = 4°$, the propagating beam is switched by total internal reflection at an emitter current of 150 mA, and an extinction ratio of better than 14 dB is obtained. The results are shown in Fig. 2.8. Typical optical field/power distributions obtained for both the through and crossover states as well as for the "intermediate" state are shown in Fig. 2.9(a), (b), and (c), respectively.

It can be observed from Fig. 2.10, that if the intersecting angle is increased, for example to θ = 8°, then though the switch length can be reduced, the required refractive index change $\Delta\mu$ as derived from the conditions for total internal reflection will be increased, thereby increasing the required switching current density. The switching current therefore cannot be reduced by a profitable amount. The more serious and limiting factor is an increase of optical radiative losses around the bend for large intersecting angles. For $\theta = 8°$, the optical radiative loss is determined to be ~ 1 dB in the crossover state, while that

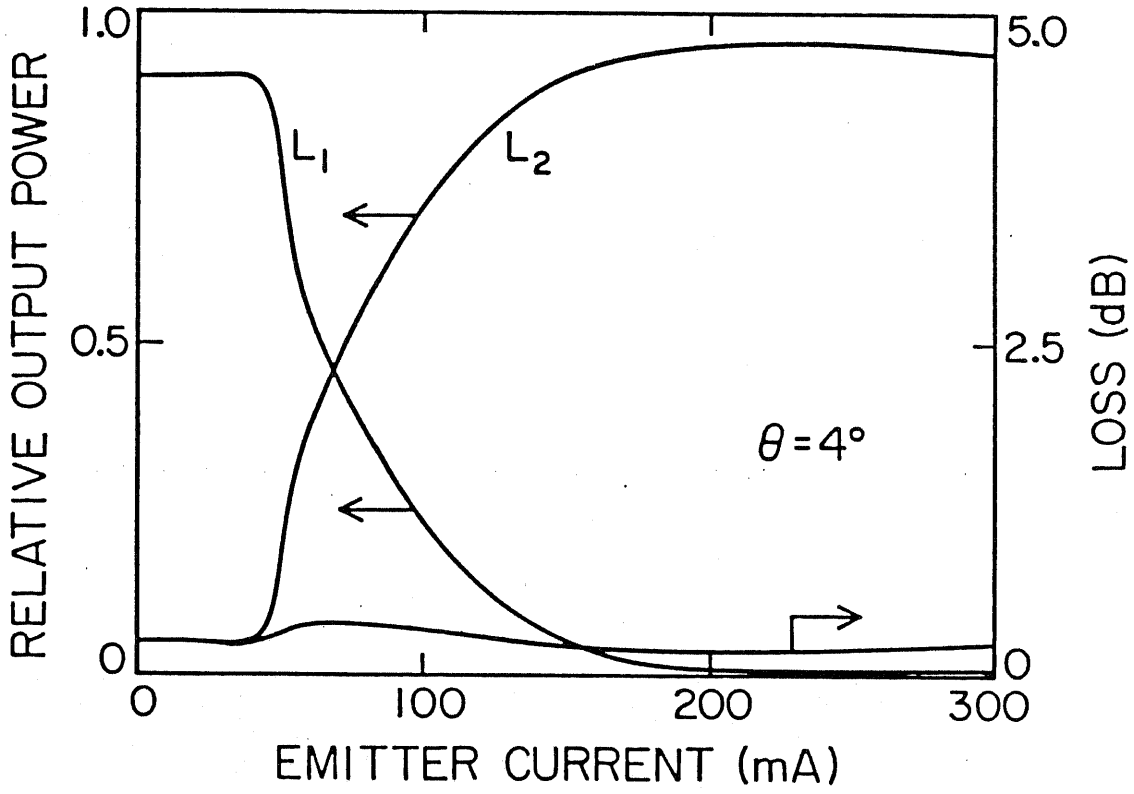

Fig. 2.8 Optical switching characteristics for $\theta = 4°$, calculated using the BPM method.

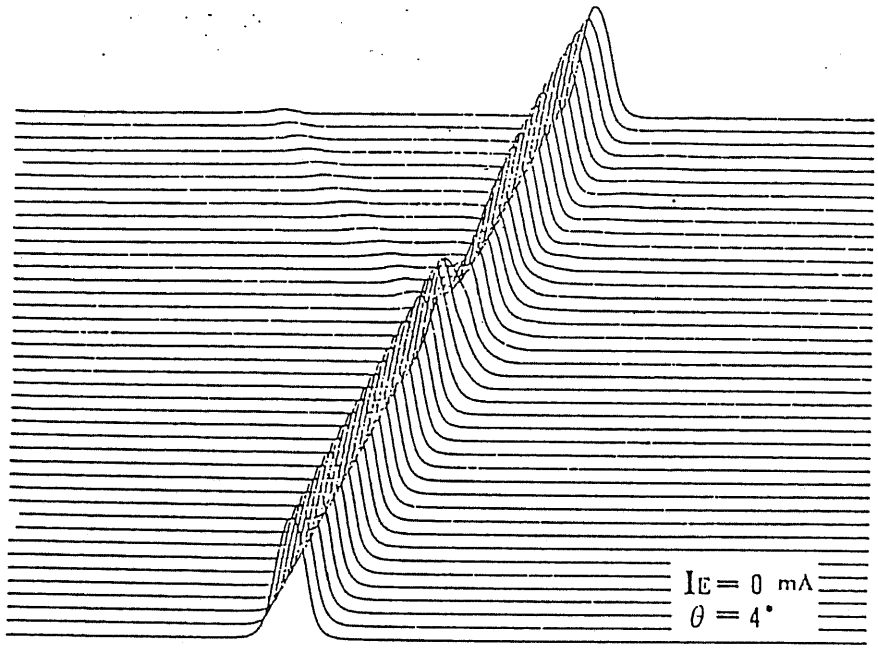

(a)

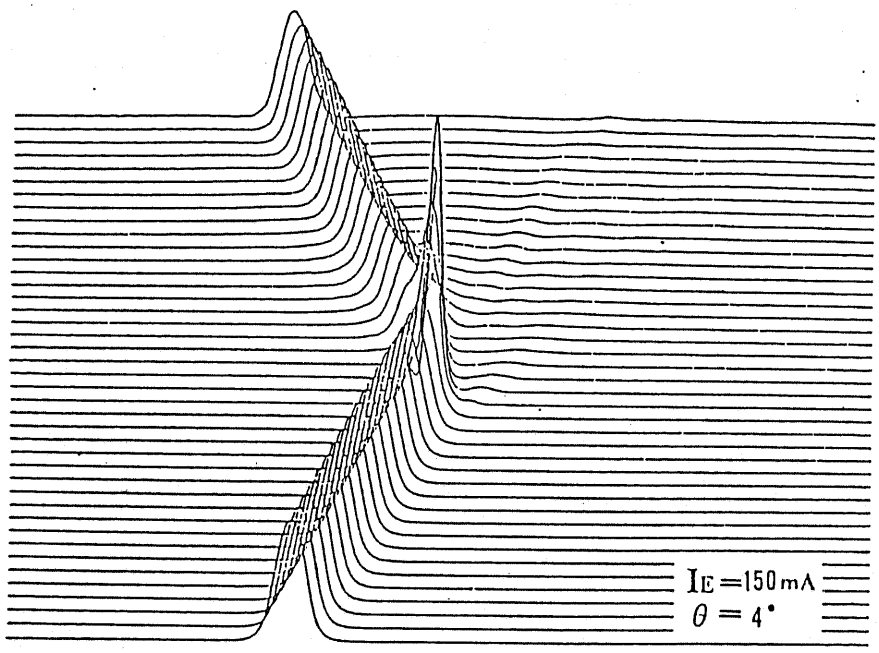

(b)

Fig. 2.9 Calculated optical power distributions obtained for; (a)through state, (b)cross-over state, and (c)"intermediate" state. $\theta = 4°$.

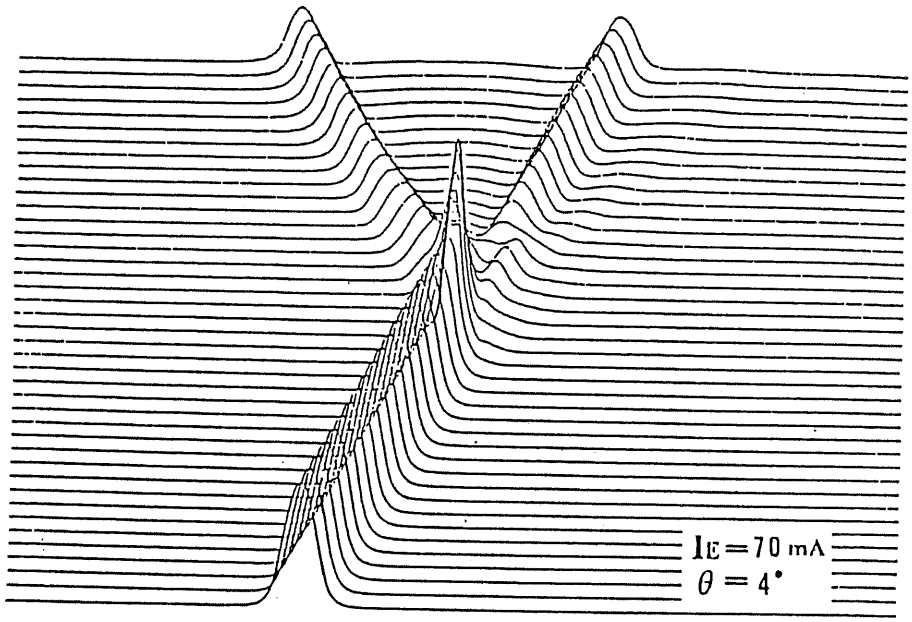

(c)

Fig. 2.9 Calculated optical power distributions obtained for; (a)through state, (b)cross-over state, and (c)"intermediate" state. $\theta = 4°$.

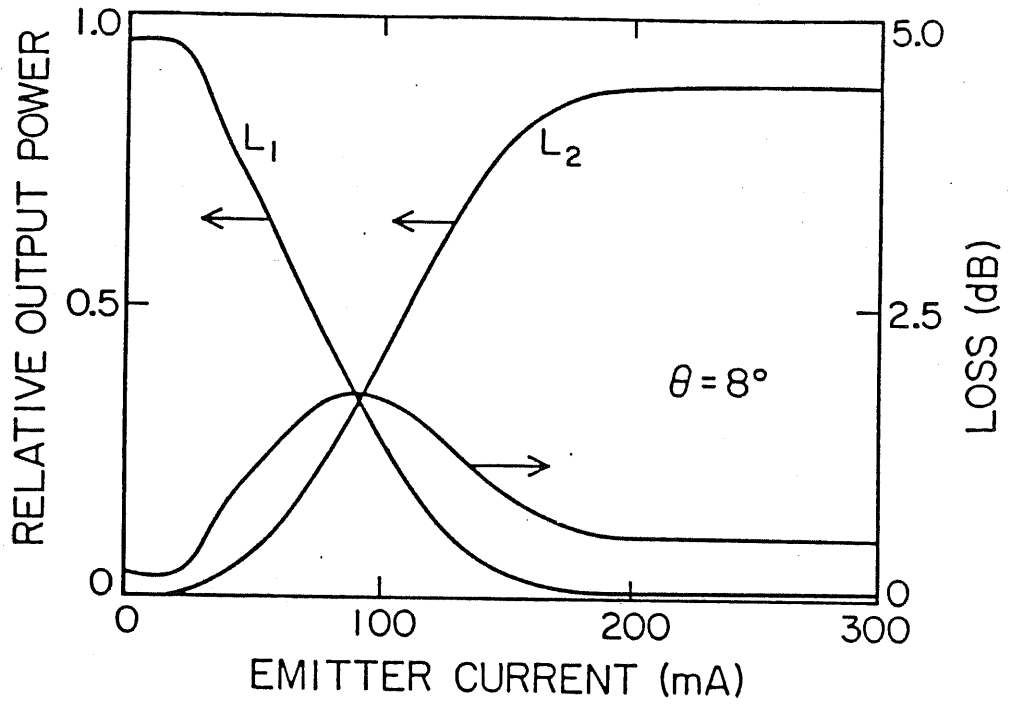

Fig. 2.10 Optical switching characteristics for $\theta = 8°$.

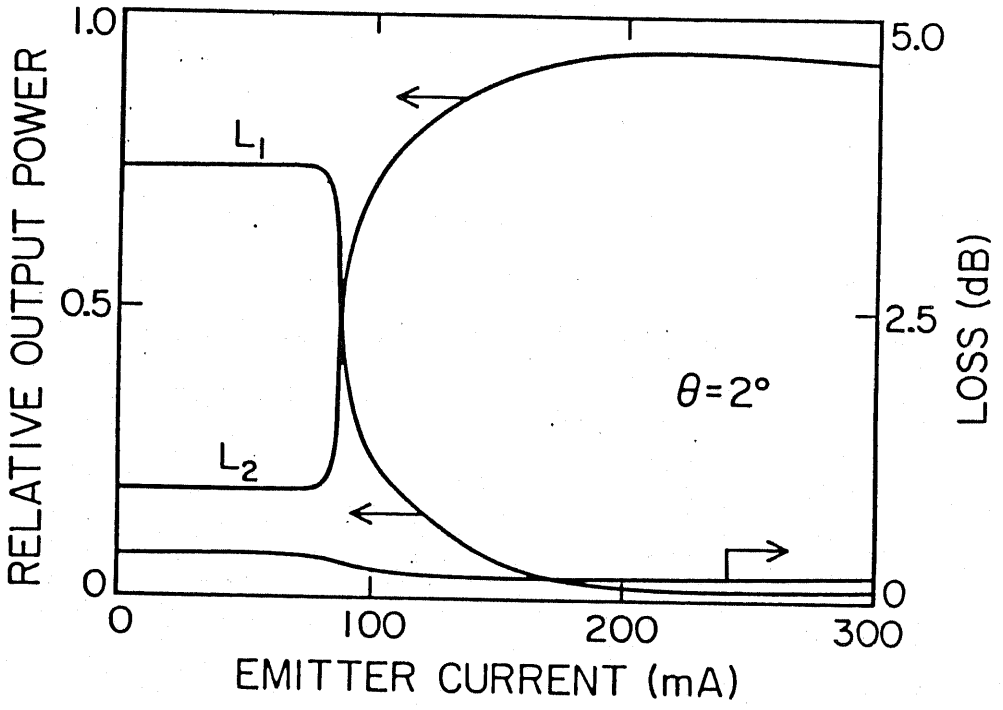

Fig. 2.11 Optical switching characteristics for $\theta = 2°$.

for $\theta = 4°$ is < 0.5 dB.

If the angle is reduced, for example to $\theta = 2°$, in attempt to reduce the required $\Delta\mu$, then the resulting increased switch area increases the required switching current, as can be observed from Fig. 2.11. Furthermore, in view of fast optical switching, an increased depletion layer capacitance of the base-collector junction of the transistor due to a larger junction area, is undesirable. Therefore, the optimum intersecting angle is $\theta \sim 4°$.

2.4.2 Switching Speeds

The analytical expressions for the 0–90% rise time t_r, and 100-10% fall time t_f of the output current when a bipolar transistor is driven by a constant input current in the common-base configuration, can be derived from the method of charge control analysis [24]–[29], and are given approximately by,

$$t_r = \left(\frac{1}{\omega_N} + M\ \alpha_N C_{ct} R_L \right) \ln \left[\frac{I_{E_1}}{I_{E_1} - \dfrac{0.9\, I_{C_{on}}}{\alpha_N}} \right] \tag{2-10}$$

$$t_f = \left(\frac{1}{\omega_N} + M'\ \alpha_N C_{ct} R_L \right) \ln \left[\frac{I_{C_{on}} + \alpha_N I_{E_2}}{0.1\, I_{C_{on}} + a_N I_{E_2}} \right] \tag{2-11}$$

where I_{E_1} and I_{E_2} are the values of the emitter current after the switch-on and switch-off step are applied, respectively, α_N and ω_N are the normal small-signal active region current gain and cut-off frequency, $I_{C_{on}}$ is the collector current in the on-state, R_L is the load resistance, and C_{ct} is the depletion layer capacitance of the base-collector junction obtained by the usual Poisson analysis. M, M' are given by,

$$M = \frac{2\left[\phi_{BC} + V_{BC_i} - \left(\left(\phi_{BC} + V_{BC_i} \right) \left(\phi_{BC} + V_{BC_j} \right) \right)^{1/2} \right]}{V_{BC_i} - V_{BC_j}} \tag{2-12}$$

where V_{BC_i} and V_{BC_j} represent the initial and final values of the changes in the base-collector voltage before and after the currents are applied, respectively, and ϕ_{BC} is the contact potential between the base-

collector junction.

The rise time and the fall time as a function of step-input emitter current are plotted in Fig. 2.12 and Fig. 2.13, in which the effect of base width modulation is also taken into consideration. The base width varies with V_{BC} and is approximately given by,

$$w\,(V_{BC}) = w_0 - (2\,\varepsilon / q\,N_A)^{1/2}\,(\phi_{BC} + V_{BC})^{1/2} \qquad (2\text{-}13)$$

where q is the electron charge, ε is the permittivity (For GaAs, $\varepsilon = 13\,\varepsilon_0$ is assumed.), N_A is the acceptor density in the base, and w_0 is the base width when $V_{BC} = -\phi_{BC}$.

For the calculations of the switching times, we assume the following numerical values;

Recombination lifetime τ_n in GaAs= 1 ns.

Electron diffusion constant $D_n = 85$ cm^2/sec

Electron diffusion length $L_n = (D_n\,\tau_n)^{1/2} = 2.9$ μm

Base width $w = 0.6$ μm

Base acceptor doping $N_A = 10^{17}$ cm^{-3}

Collector donor doping $N_D = 10^{17}$ cm^{-3}

Collector area $A_C = 1.2\times10^{-5}$ cm^2 (corresponding to $\theta = 4°$)

Base-collector contact potential ϕ_{BC} [30] = 1.53 eV

Load resistance $R_L = 50\,\Omega$

It can be observed that both the t_r and t_f are approximately 60 ps for the required optical on-off switching. These switching times are about two orders of magnitude faster than those obtainable with the conventional *pn* (*p-i-n*) structured devices.

2.4.3 Comments

The emitter current of 150 mA, as determined for the required optical switching may be relatively large and hence, some thermal problems may arise if the device is tested in practice. The dissipation of heat due to a large current flow results in thermally-induced refractive index variations, and also limits its use in very fast on-off current switching applications unless some measures are taken to remove the heat efficiently. In thought of possible reduction of the switching currents, the transistor may be operated in

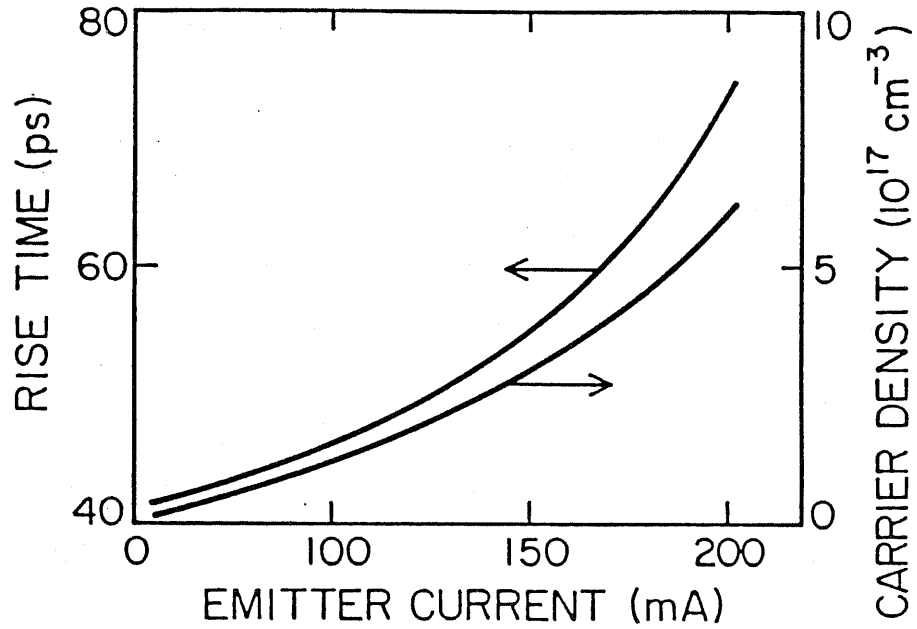

Fig. 2.12 Rise time of the transistor, calculated using the charge-control analysis.

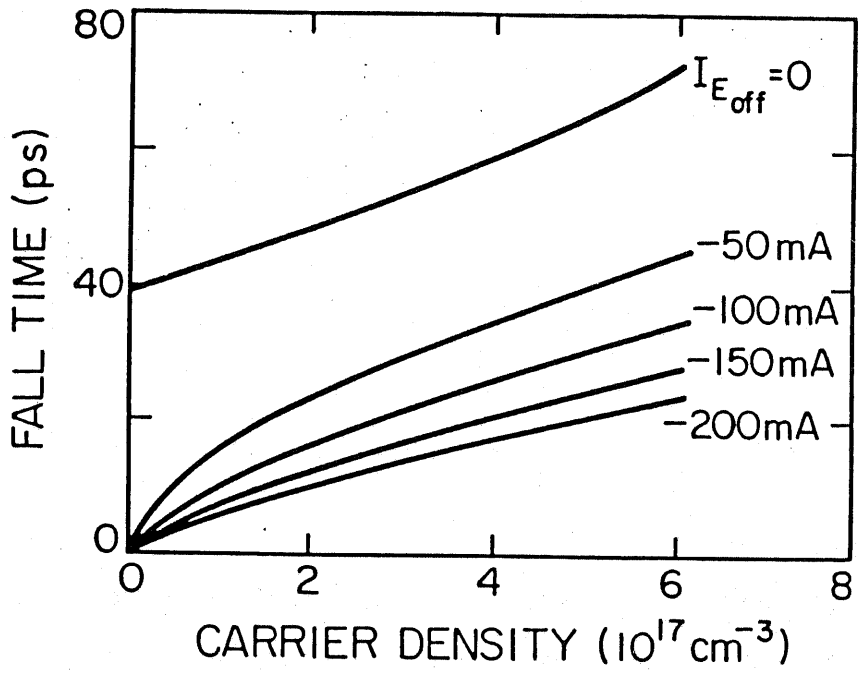

Fig. 2.13 Calculated fall time of the transistor.

the saturation regime, at the expense of an increased switch-off time by the storage time T_s.

In homogeneous base transistors, the charge configuration in the base region shortly after the switch-on is as shown in Fig. 2.14(a), and the switch-off characteristics will be as those illustrated in Fig. 2.14(b). When the base charge has been set up and has reached an equilibrium distribution in a time of the order of 1/5 of the steady-state transit time [25], the collector current I_C is proportional to the base charge gradient at the boundary of the collector junction. In homogeneous base transistors, this base gradient is nearly linear throughout the base region and is proportional to the total minority charge Q_B so that the collector current is approximately proportional to this base charge. Moreover, it can be readily seen that for the same current, Q_B is considerably smaller than the total charge that would have been present, if the base-collector junction were not reverse biased. This is so in this case, because the minority carrier lifetime τ_B in Eq. (2-9) is now given by the recombination lifetime τ_n.

If the transistor is driven into saturation, then the collector current is circuit controlled so that an increase in the base charge cannot lead to an increase in the collector current. Both the emitter-base and base-collector junctions are now forward biased and what happens then is that a saturation charge Q_{B_s} accumulates in the base until its recombination rate equals exactly the rate at which extra current is supplied to the base through an external circuit. The saturation charge which accumulates in the base of a homogeneous base transistor is illustrated in Fig. 2.15(a).

Using a quasi-three dimensional model [29], it is determined that the magnitude of the optical switching currents can be reduced by an estimate of more than 30%, if the transistor is operated in the saturation region. However, this excess storage of carriers in the base results in an increased switch-off time by the storage time T_s as shown in Fig. 2.15(b), which for the common-base mode is given by [24]–[29],

$$T_s = \left(\frac{\omega_N + \omega_I}{\omega_N \omega_I (1 - \alpha_N \alpha_I)} \right) \ln \left[\frac{I_{E_2} - I_{E_1}}{I_{E_2} + \frac{I_{C_{on}}}{\alpha_N}} \right] \tag{2-14}$$

where the suffix I represents the inverted state. The storage time T_s, however, can be shortened considerably by applying a large negative emitter current I_{E_2} at the moment of switch-off. A calculated relationship between T_s and I_{E_2} is shown in Fig. 2.16, and it is observed that for $|I_{E_2}|$ = 100 mA, $T_s \approx$ 40 ps.

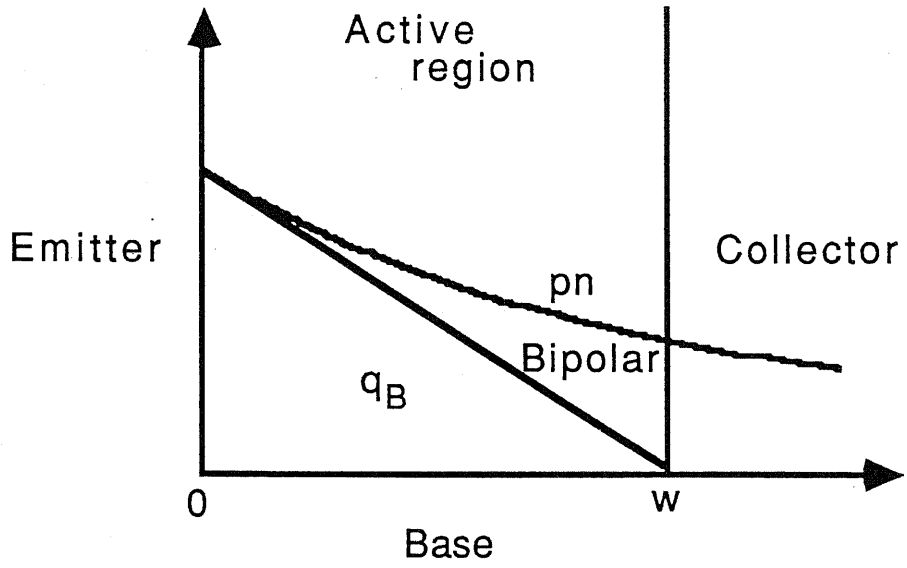

(a)

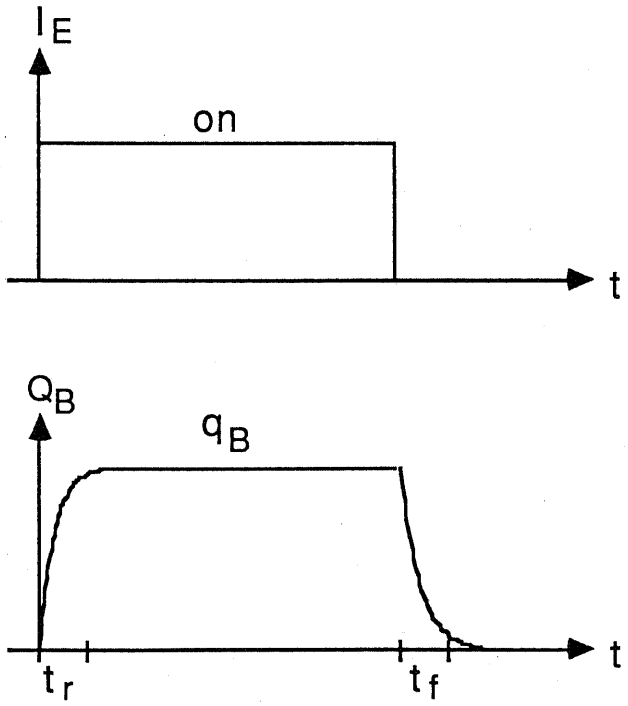

(b)

Fig. 2.14 (a)Charge distribution in the base, when the transistor is operated in the active region, and (b)Response to a large-signal current pulse.

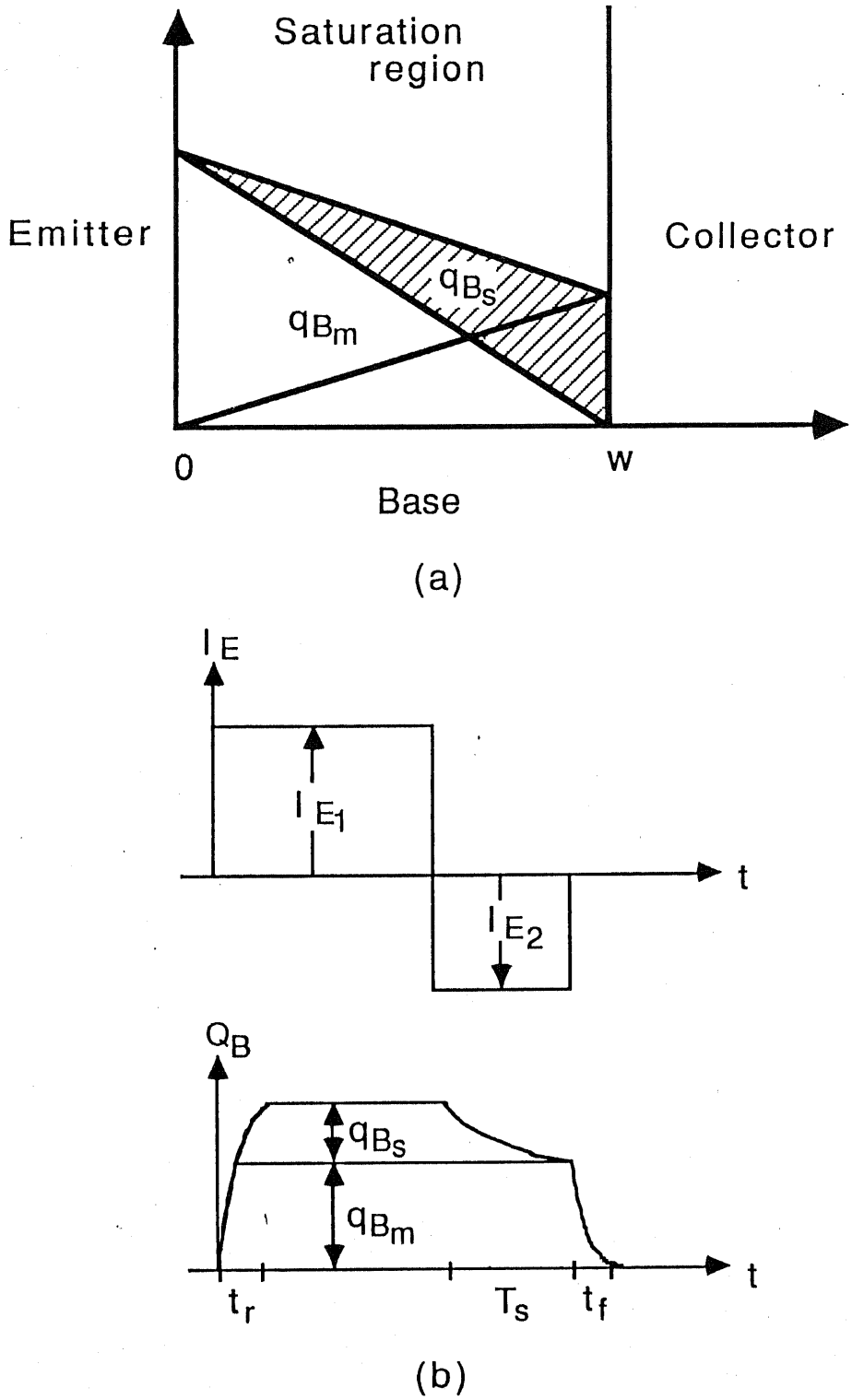

Fig. 2.15 (a)Charge distribution in the base, when the transistor is operated in the saturation region, and (b)Response to a large-signal current pulse. The switch-off time is increased by the storage time, T_s .

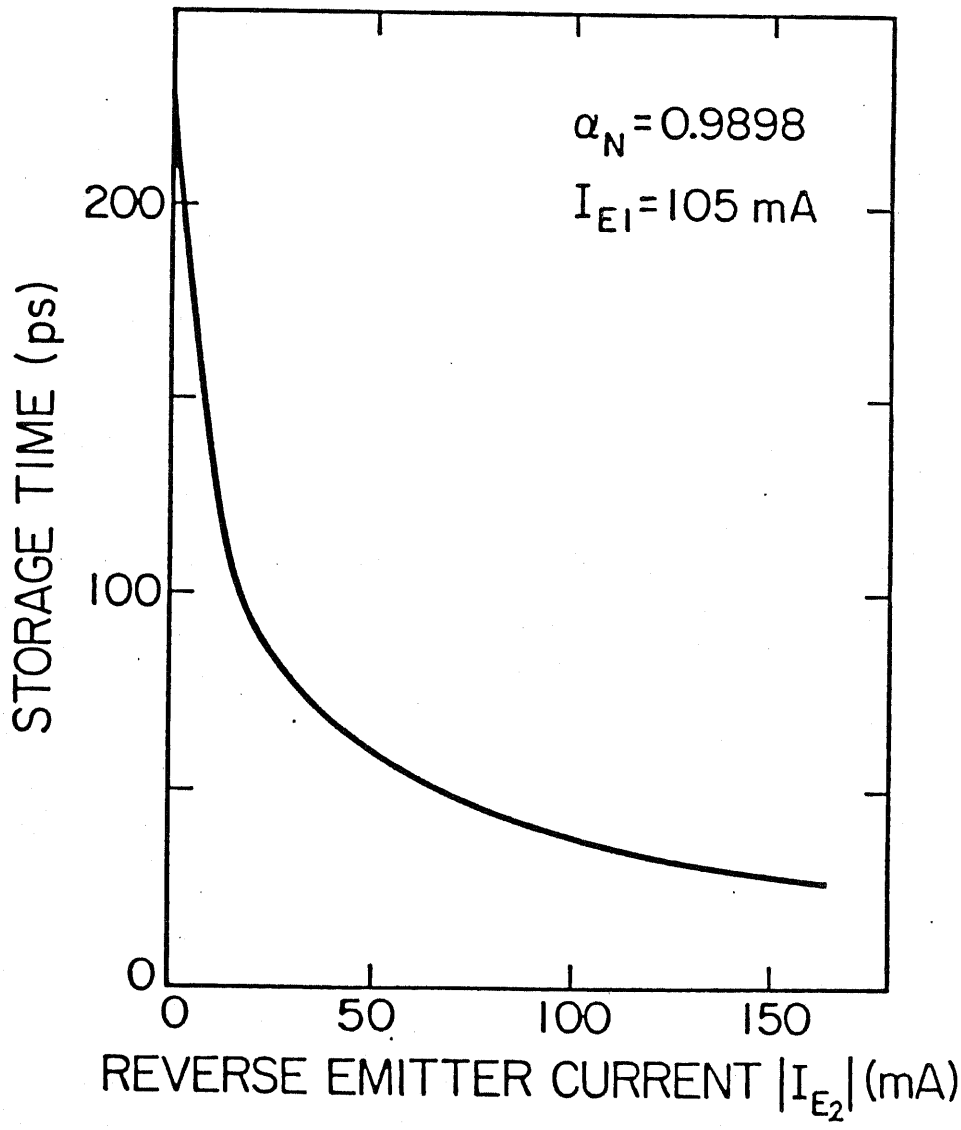

Fig. 2.16 Calculated relationship between the storage time and the reverse emitter current.

2.5 Conclusions

In this chapter, we have proposed a Bipolar Transistor Carrier-Injected Optical Modulator/Switch, and discussed its potential advantages. Some of the basic design rules and inherent characteristics are also discussed.

A theoretical analysis on the switching characteristics and the mode propagation behavior of the structure applied to a GaAs/AlGaAs DH-TIR X-switch is performed using the beam propagation method (BPM). It is concluded that for the proposed structure and $\theta = 4°$, the propagating beam is switched by total internal reflection at an emitter current of 150 mA and an extinction ratio of ~ 14 dB has been obtained.

A charge control analysis shows that the switching times of the proposed bipolar transistor structure can be as fast as ~ 60 ps, which are considerably faster than those expected for diode structures, which are typically on the order of 10 ~ 100 ns. We have also discussed qualitatively and quantitatively a method of reducing the switching current by driving the transistor into the saturation region.

Finally, Bipolar Transistor Carrier-Injected Optical Modulator/Switch is expected to be very useful in applications which require optical modulation as well as switching above 10 GHz frequency range.

References

[1] C. H. Henry, R. A. Logan, and K. A. Bertess, "Spectral dependence of the change in refractive index due to carrier injection in GaAs lasers", *J. Appl. Phys.*, vol. 52, p. 4457, 1981.

[2] M. Ito and T. Kimura, "Carrier density dependence of refractive index in AlGaAs semiconductor lasers", *IEEE J. Quantum Electron.*, vol. QE-16, p. 910, 1980.

[3] S. E. H. Turley, "Anomalous effect of carriers on dielectric constant of (In,Ga)(As,P) lasers at 1.3 μm wavelength", *Electron. Lett.*, vol. 18, p. 590, 1982.

[4] J. Manning, R. Olshansky, and C. B. Su, "The carrier-induced index change in AlGaAs and 1.3 μm InGaAsP diode lasers", *IEEE J. Quantum Electron.*, vol. QE-19, p. 1525, 1983.

[5] C. H. Henry, R. A. Logan, and F. R. Merritt, "Measurement of gain and absorption spectra in AlGaAs buried heterostructure lasers", *J. Appl. Phys.*, vol. 51, p. 3042, 1980.

[6] J. P. Lorenzo and R. A. Soref, "1.3 μm electro-optic silicon switch", *Appl. Phys. Lett.*, vol. 51, p. 6, 1987.

[7] O. Mikami and H. Nakagome, "Waveguided optical switch in InGaAsP/InP using free carrier plasma absorption", *Electron. Lett.*, vol. 20, p. 228, 1984.

[8] O. Mikami and H. Nakagome, "InGaAsP/InP optical waveguide switch operated by a carrier-induced change in the refractive index", *Opt. Quantum Electron.*, vol. 17, p. 449, 1985.

[9] K. Ishida, H. Nakamura, H. Matsumura, T. Kadoi, and H. Inoue, "InGaAsP/InP optical switches using carrier induced refractive index change", *Appl. Phys. Lett.*, vol. 50, p. 141, 1987.

[10] H. Inoue, H. Nakamura, Y. Sasaki, T. Katsuyama, N. Chinone, and K. Morosawa, "Eight-millimeter long nonblocking 4×4 optical switch array", *Technical Digest of the 8th. CLEO*, TUK1, Anaheim, 1988.

[11] S. Sakano, H. Inoue, H. Nakamura, T. Katsuyama, and H. Matsumura, "InGaAsP/InP monolithic integrated circuit with lasers and an optical switch", *Electron. Lett.*, vol. 22, p. 594, 1986.

[12] E. A. J. Marcatili, "Dielectric rectangular waveguide and directional coupler for integrated optics", *Bell Syst. Tech. J.*, vol. 48, p. 2071, 1969.

[13] H. C. Casey, Jr., D. D. Sell, and M. B. Panish, "Refractive index of Al_xGa_{1-x} As between 1.2 and 1.8 eV", *Appl. Phys. Lett.*, vol. 24, p. 63, 1974.

[14] L. A. Coldren, *private communication.*

[15] H. Kroemer, "Theory of a wide-gap emitter for transistors", *Proc. IRE*, vol. 45, p. 1535, 1957.

[16] H. Kroemer, "Heterostructure bipolar transistors and integrated circuits", *Proc. IEEE*, vol. 70, p. 13, 1982.

[17] P. M. Asbeck and D. L. Miller, " Recent advances in GaAs/(Ga,Al)As heterojunction bipolar transistors", *Extended Abstracts of the 16th (International) Conference on Solid-State Devices and Materials*, Kobe, p. 343, 1984.

[18] Y. Mori, J. Shibata, Y. Sasai, H. Serizawa, and T. Kajiwara, "Operation principle of the InGaAsP/InP laser transistor", *Appl. Phys. Lett.*, vol. 47, p. 649, 1985.

[19] C. S. Tsai, B. Kim, and F. R. El-Akkari, "Optical channel waveguide switch and coupler using total internal reflection", *IEEE J. Quantum Electron.*, vol. QE-14, p. 513, 1978.

[20] H. Inoue, *private communication.*

[21] J. Van Roey, J. van der Donk, and P. E. Lagasse, "Beam-propagation method: analysis and assessment", *J. Opt. Soc. Am.*, vol. 71, p. 803, 1981.

[22] M. D. Feit and J. A. Fleck, Jr., "Light propagation in graded-index optical fibers", *Appl. Opt.*, vol. 17, p. 3990, 1978.

[23] H. Kawamura, *B.E. Thesis, Department of Electronic Engineering, University of Tokyo*, March, 1985.

[24] R. Beaufoy and J. J. Sparkes, "The junction transistor as a charge controlled device", *ATEJ*, vol. 13, p. 310, 1957.

[25] J. J. Sparkes, "A study of the charge control parameters of transistors", *Proc. IRE*, vol. 48, p. 1696, 1960.

[26] J. L. Moll, "Large signal transient response of junction transistors", *Proc. IRE*, vol. 42, p. 1773, 1954.

[27] K. Tada, T. Sugano, and H. Yanai, *J. IEE Jpn.*, vol. 82, p. 982, 1962.

[28] K. Tada and H. Yanai, *J. IECE Jpn.*, vol. 50, p. 278, 1967.

[29] K. Tada, Paper of *Technical Group on Semiconductors and Semiconductor Devices, IECE Jpn.*, vol. 20, p. 2, 1967.

[30] R. Dingle, "Confined carrier quantum states in ultrathin semiconductor heterostructures", *Advances in Solid State Physics*, vol. 15, p. 21, 1975.

CHAPTER 3

THE EFFECT OF BAND-TAILS AND ITS APPLICATION TO GaAs/AlGaAs OPTICAL MODULATORS AND SWITCHES OPERATED BY FREE-CARRIER INJECTION

3.1 Introduction

Studies on the carrier-induced absorption and index changes have been carried out on some intensive scale in the field of semiconductor diode lasers, and for example, such index changes are known to be the cause for the spectral broadening of the longitudinal modes, a phenomenon long known as the chirping. These carrier-induced effects are also important in analyzing various forms of semiconductor optical modulators and switches. Especially, the band-filling effect is an important carrier-related effect and it has been evaluated in detail for GaAs/AlGaAs optical phase modulators using a simple parabolic band approximation, and it is shown that the band-filling effect can contribute to the total phase shift significantly by as much as ~ 25% [1]–[2]. The use of the parabolic band model may be justified in the case of lightly-doped waveguide layers and depletion-type optical modulators and switches; however, the effect of band-tails, plasma dispersion, and band-gap shrinkage must also be considered in addition to the band-filling effect, once the level of carrier injection and/or the doping of the interaction region becomes high, as in the case of the carrier-injected optical modulators and switches.

In this chapter, a complete calculation of the variations in the absorption coefficient and the refractive index in the waveguide region of a DH *N*-AlGaAs/*p*-GaAs/*N*-AlGaAs device structure, as a result of free carrier injection, is described using a band-tail model proposed by Stern [3]–[4]. The *p*-GaAs layer also serves as the base region of an HBT, and therefore is relatively heavily-doped in order to reduce the base resistance, which is an important device parameter that determines the upper limit of the modulation frequency. The results are then used to analyze in detail the performance of DHBT optical modulators and switches operated by free carrier injection, from the practical viewpoint of frequency chirping, absorption loss, and modulation depth. Optimum operating conditions are also evaluated.

3.2 Carrier-Induced Modulation of Absorption Coefficient and Refractive Index

3.2.1 Introduction

Many different analytic band models have been used to study the effects of heavy impurity doping and high carrier concentrations on the band-tailing in GaAs [3]–[8], and as shown by Hwang [7], the effects of carriers and doping start to become important for electron concentrations of about 4×10^{17} cm^{-3}, for which the electron average spacing is then comparable to the effective Bohr radius; for holes, the minimum concentration is around 1×10^{18} cm^{-3}. In this section, the changes in the absorption coefficient and the refractive index caused by free carrier injection are calculated using a band-tail model proposed by Stern [3]–[4], since his analytical model fits the experimentally determined absorption spectra very well.

For the purpose of calculation, we consider a double heterostructure (DH) waveguide formed by a p-GaAs layer, placed between an N-$Al_{0.2}Ga_{0.8}As$ ($N_D = 5\times10^{17}$ cm^{-3}) cladding layer and an N-$Al_{0.2}Ga_{0.8}As$ ($N_D = 10^{17}$ cm^{-3}) buffer layer. Both the donors in the N-AlGaAs layers and the acceptors in the p-GaAs layer are assumed to be fully ionized at room temperature. Also in the p-GaAs layer, the ratio $N_A / N_D \approx 5$ is chosen on the basis of the experimental studies on Zn-doped GaAs [9], and we take $p = N_A - N_D = 1.2\times10^{18}$ cm^{-3}, and the band-gap energy E_g = 1.408 eV at 300 K for this doping level [4]. Thus, we have an N-emitter/p-base/N-collector device configuration as shown in Fig. 3.1, which we define as a double-heterojunction bipolar transistor (DHBT) carrier-injected optical modulator/switch.

When a forward bias is applied across the N-AlGaAs/p-GaAs emitter-base heterojunction, free carriers, in this case electrons, will be injected into the p-GaAs base or waveguide layer. The flow of carriers in the reverse direction, that is, the flow of holes into the higher-energy-gap N-AlGaAs emitter or cladding layer, is efficiently blocked by the energy barrier inherently present at the heterojunction plane [10]–[11]. The effect of free carriers therefore is mainly observed in the p-GaAs waveguide layer.

As the level of carrier injection is increased, the absorption coefficient in the p-GaAs layer will change mainly because the quasi-Fermi level moves toward and eventually into the conduction band, giving rise to a shift of the absorption edge toward higher energy, an effect known as the band-filling or Burstein-Moss shift. As a final consequence, the changes in the absorption edge change the refractive index of the layer through the Kramers-Kronig dispersion relationship. These variations in the absorption and the refractive index mainly due to the band-filling effect caused by free carrier injection, together with

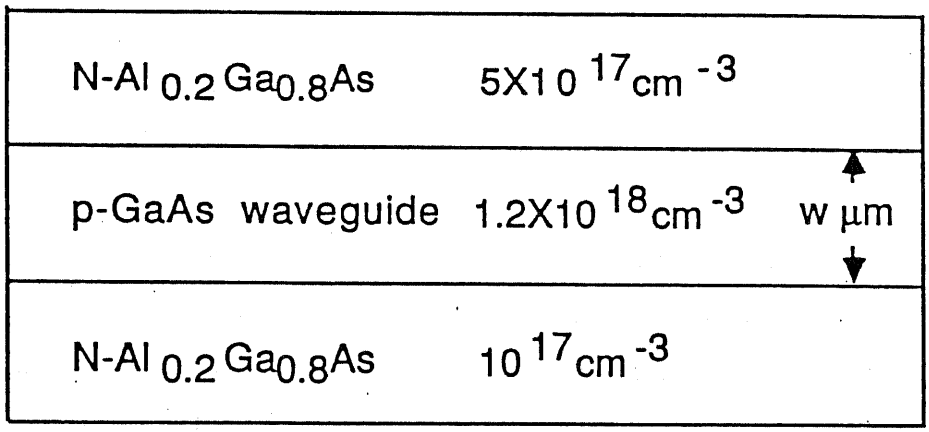

Fig. 3.1 Cross-section of the double-heterostructure (DH) *N-p-N* bipolar transistor waveguide structure considered for the analysis; the *p*-GaAs waveguide layer is heavily doped to $p=1.2\times10^{18}$ cm^{-3}.

the bipolar transistor device structure, can be used as a high-speed modulation/switching scheme in optical communication and processing systems.

3.2.2 Calculation of Optical Absorption Coefficient

The absorption coefficient α, for transitions between the conduction and valence band and the variations in the absorption edge with free carrier injection at a given photon energy E in the p-GaAs layer are calculated from the integral [12],

$$\alpha(E) = \frac{\pi q^2 \hbar}{\varepsilon_0 m_0^2 c \mu E} \int_{-\infty}^{+\infty} \rho_c(E_2)\,\rho_v(E_1)\,|M_{12}|^2\,[f(E_1) - f(E_2)]\,dE_2 \qquad (3\text{-}1)$$

where $E_1 = E_2 - E$, m_0 is the free electron mass, ε_0 is the permittivity of free space, μ is the index of refraction, ρ_c and ρ_v are the densities of states per unit volume and per unit energy interval in the conduction and valence band, respectively, M_{12} is the effective optical matrix element of the momentum operator between the two transition states, and f is the Fermi-Dirac distribution function; $f(E_1) = 1 / [1 + \exp((E_{fv} - E_1) / kT)]$, and $f(E_2) = 1 / [1 + \exp((E_2 - E_{fc}) / kT)]$.

In evaluating the integral in Eq. (3-1) by numerical computation, the band-gap shrinkage effect caused by the free carriers, and the contributions from both the heavy-hole and light-hole transitions to the total absorption are considered (by taking a sum of the terms obtained for each valence band using Eq. (3-1)). The amount of band-gap shrinkage ΔE_g associated with excitation is approximated by an experimentally determined relationship [4],

$$\Delta E_g\ (\text{eV}) = -\ 1.6\times10^{-8}\ (\Delta n^{1/3} + \Delta p^{1/3}) \qquad (3\text{-}2)$$

where Δn and Δp are in units of cm^{-3}, and $\Delta p \rightarrow 0$ for the case of the electron injection. The split-off valence band is ignored because it makes no significant contribution to the optical absorption of GaAs in the energy range of interest.

The effect of the band-tail is included by using Stern's density of states and optical matrix element [3]–[4], and some of the important points are summarized in the following section.

(A) Density of States

A model in which the electrons (holes) have sufficiently low kinetic energy so that they can follow the fluctuations in the potential (whose root mean square is V_{rms}) leads to a conduction-band (valence-band) density of states of the form [5],

$$\rho_c(E_2) = \left[\frac{2^{1/2} m_c^{3/2}}{\pi^2 \hbar^3}\right] \eta_c^{1/2} y \left(\frac{E_2 - E_c}{\eta_c}\right) \qquad \text{conduction band}$$

$$\rho_v(E_1) = \left[\frac{2^{1/2} m_v^{3/2}}{\pi^2 \hbar^3}\right] \eta_v^{1/2} y \left(\frac{E_v - E_1}{\eta_v}\right) \qquad \text{valence band} \tag{3-3}$$

where m_c and m_v are the density-of-states mass, and E_c and E_v are the nominal "parabolic" band-edge, for the conduction and valence band respectively. η_c and η_v are Stern's band-tail parameter for the corresponding band, and are smaller than the Kane's value, $\eta = \sqrt{2} V_{rms}$ (the reasons are discussed later in the section). y is known as Kane's band-tail function and is represented in an integral form as,

$$y(x) = \pi^{-1/2} \int_{-\infty}^{x} (x - z)^{1/2} \exp(-z^2)\, dz \tag{3-4}$$

If the potential fluctuations arise from the Coulomb potentials (Gaussian) of N_D^+ ionized donors and N_A^- ionized acceptors per unit volume that are randomly distributed on the lattice sites, then V_{rms}, which determines η, is given by,

$$V_{rms} = (q^2 / 4\pi\varepsilon)\, [\, 2\pi\, (N_D^+ + N_A^-)\, L_s\,]^{1/2} \tag{3-5}$$

where L_s is the screening length, and is given by,

$$L_s = \left[-\left(\frac{d\rho}{d\varphi}\right)_{\varphi=0} \varepsilon^{-1}\right]^{-1/2} \tag{3-6}$$

where ρ is the charge density in the crystal, and φ is the electrostatic potential associated with the presence of the charged impurities. In general, L_s depends on the carrier concentration, on the temperature, and on the actual shape of the density of states. Therefore, as shown by Eqs. (3-3), (3-5), and (3-6), a self-consistent solution is necessary in determining ρ_c or ρ_v, and L_s. At room temperature, however, the density of states has relatively small influence on L_s, therefore the free-carrier result,

$$L_s = (\varepsilon kT / p\, q^2)^{1/2} \tag{3-7}$$

which is the Debye length, can be used [3]. For $N_A = 1.5\times10^{18}$ cm^{-3}, $N_D = 3\times10^{17}$ cm^{-3}, (hence $p = 1.2\times10^{18}$ cm^{-3}), $\varepsilon = 13\varepsilon_0$, and $T = 300$ K, we obtain $L_s = 39$ Å, and $V_{rms} = 21$ meV [4].

Kane's density of states given in Eq. (3-3) neglects the possibility of electrons or holes tunneling through the potential barriers, and therefore overestimates the extent of band-tailing unless the carriers have a very large effective mass. Halperin and Lax made an improved analysis of the density of tail states by taking the kinetic energy of the carriers into account [6], and presented numerical results in a limited energy range in the band-tail. Stern's density of states in each band is characterized by a one-parameter fit of the density of states of Kane's model to the Halperin-Lax results in the band-tail, as shown in Fig. 3.2(a). The (only) fitting parameter is the band-tail parameter η_c and η_v in each band, which is found by requiring that the approximate density of states equals the value calculated by Halperin and Lax at an energy within the validity of their results. $\eta_c = 10$ meV and $\eta_v = 20$ meV are used in this work [4], which are smaller than the Kane's value $\eta = 30$ meV as can be obtained from Eq. (3-5). Furthermore, the bulk density-of-states mass is used to assure that the density of states agrees with the value in the undisturbed parabolic band structure for energies sufficiently above the band-tail; for GaAs, $m_c = 0.067m_0$, $m_{lh} = 0.085m_0$, and $m_{hh} = 0.50m_0$ are assumed.

(B) Optical Matrix Element

Stern's optical matrix element describes two different types of optical transitions; the transitions between the parabolic band states for high energies, where the **k**-selection rule is obeyed, and those between the band-tail states where the selection rule is not strictly obeyed, giving rise to a constant matrix element.

For localized energy states such as impurity states, the wave function can be written in an effective mass approximation as, $\psi(\mathbf{r}) = \psi_{env}(\mathbf{r})\, u(\mathbf{r})$, where $u(\mathbf{r})$ is a Bloch function at the appropriate

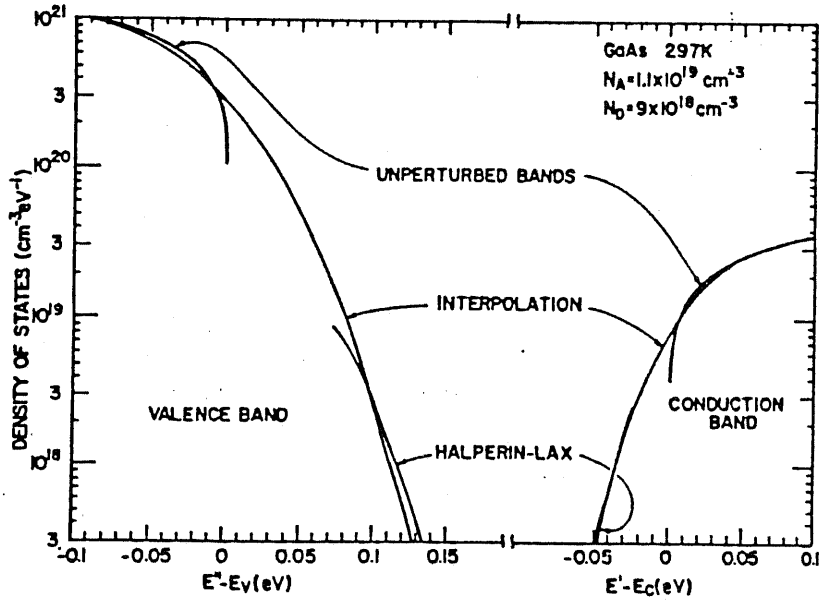

Fig. 3.2(a) Stern's Gaussian density of states, which is characterized by an one-parameter fit of the density of states of Kane's model to the Halperin-Lax results in the band-tail. (After reference [4])

band-edge, and ψ_{env} (r) is a normalized envelope wave function. For a plane-wave state with a wave vector **k**, the wave function can be written in the form, $\psi(\mathbf{r}) = V^{-1/2}\, u(\mathbf{r})\, \exp(i\mathbf{k}\cdot\mathbf{r})$, where V is the volume of the system. The dipole matrix element for transitions between a localized state in one band and a plane-wave state in another band is then given approximately by [5],

$$M_{12} = M_b\, M_{env} \tag{3-8a}$$

$$M_{env} = V^{-1/2} \int \psi^*_{env}(\mathbf{r})\, \exp(i\mathbf{k}\cdot\mathbf{r})\, d^3\mathbf{r} \tag{3-8b}$$

where M_b is an average matrix element connecting the Bloch states near the band edges, and for semiconductors, it is given by,

$$|M_b|^2 = \frac{m_0^2 E_g}{12 m_c}\left(\frac{E_g + \Delta}{E_g + \frac{2}{3}\Delta}\right) \tag{3-9}$$

where Δ is the spin-orbit splitting. Assuming $m_c = 0.067 m_0$, and $\Delta = 0.33$ eV for GaAs, then $|M_b|^2 = 1.35\, m_0\, E_g$.

The envelope matrix element M_{env}, which is derived by Stern assumes that the envelope wave function can be written in the following form,

$$\psi_{env}(\mathbf{r}) = (\beta^3 / \pi)^{1/2} \exp(i\mathbf{k}\cdot\mathbf{r}) \exp(-\beta\, |\, \mathbf{r} - \mathbf{r}_j\, |) \tag{3-10}$$

where **k** describes the plane-wave character of the wave function, while β determines the rate at which the wave function decays away from the localized energy state centered at $\mathbf{r}_j$. Both parameters are in units of cm^{-1}.

In order to calculate the parameters **k** and β for the envelope wave function for a bound state of energy E_2 in the perturbed conduction band, we define another energy E_c^*, such that the number of available bound states at energies less than E_c^* in the unperturbed (parabolic) density of states is equal to the number of available states at energies less than E_2 in the actual perturbed density of states. Then, $E_c^* - E_2$ is a measure of the lowering of the energy due to potential fluctuations. The same understanding is also followed for the valence band. A schematic diagram showing each parameter just

described is shown in Fig. 3.2(b). We now define, for the conduction band,

$$\hbar^2 k_c^2 / 2m_c = E_c^* - E_c \tag{3-11a}$$

$$\hbar^2 \beta_c^2 / 2m_c = h_c (E_c^* - E_2) \tag{3-11b}$$

where E_c is the nominal (parabolic) conduction band-edge. The factor h_c is chosen to make the quantity $h_c (E_c^* - E_2)$ equal the kinetic energy of a localized state, at the energy where Stern's Gaussian density of states is fitted to the Halperin-Lax value, and $h_c = 0.5$ is assumed here [3]. At high photon energies, where $E_c^* \approx E_2$, Eq. (3-10) gives the usual plane-wave result. At low photon energies, $E_c^* \approx E_c$, the state is localized and results in an appropriate kinetic energy of localization. For intermediate photon energies, the envelope wave function given by Eq. (3-10) may differ significantly from the correct envelope function, however, our main interest lies in the vicinity of the band-gap energy and hence Stern's model should give accurate results. A similar set of equations may be written for the valence band as follows,

$$\hbar^2 k_v^2 / 2m_v = E_v - E_v^* \tag{3-12a}$$

$$\hbar^2 \beta_v^2 / 2m_v = h_v (E_1^* - E_v^*) \tag{3-12b}$$

where $h_v = 0.4$ is assumed here [3].

The envelope matrix element is the product of the complex conjugate of the envelope wave function of Eq. (3-10) for the conduction band and a corresponding envelope wave function for the valence band, averaged over all directions of the wave vectors and over all positions of the sites at which the states are localized. The final form of the envelope matrix element is given by,

$$|M_{env}|^2 = (64\pi b / 3)(t^4 - q^4)^{-5} [(b^4 - 5b^2 B^2 + 5B^4)(3t^4 + q^4)(t^4 - q^4)^2 + 8b^2 B^2 t^2 (3b^2 - 10B^2)(t^8 - q^8) + 16b^4 B^4 (5t^8 + 10t^4 q^4 + q^8)] \tag{3-13}$$

where $B^2 = \beta_c \beta_v$, $b = \beta_c + \beta_v$, $t^2 = \beta^2 + k_c^2 + k_v^2$, and $q^2 = 2k_c k_v$. The structure of Stern's optical matrix element is shown in Fig. 3.2(c), where $|M_{env}|^2$ is plotted as a function of photon energy of the valence-band state measured from the nominal valence band-edge E_v.

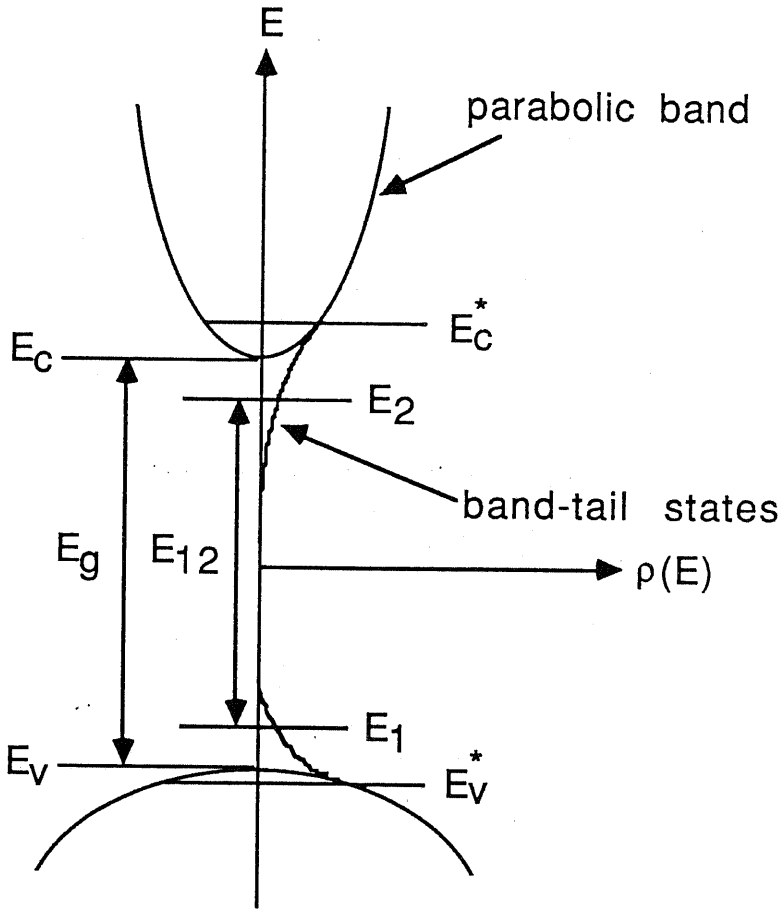

Fig. 3.2(b) Schematic density of states for the conduction band and the valence band, showing the effect of bandtailing.

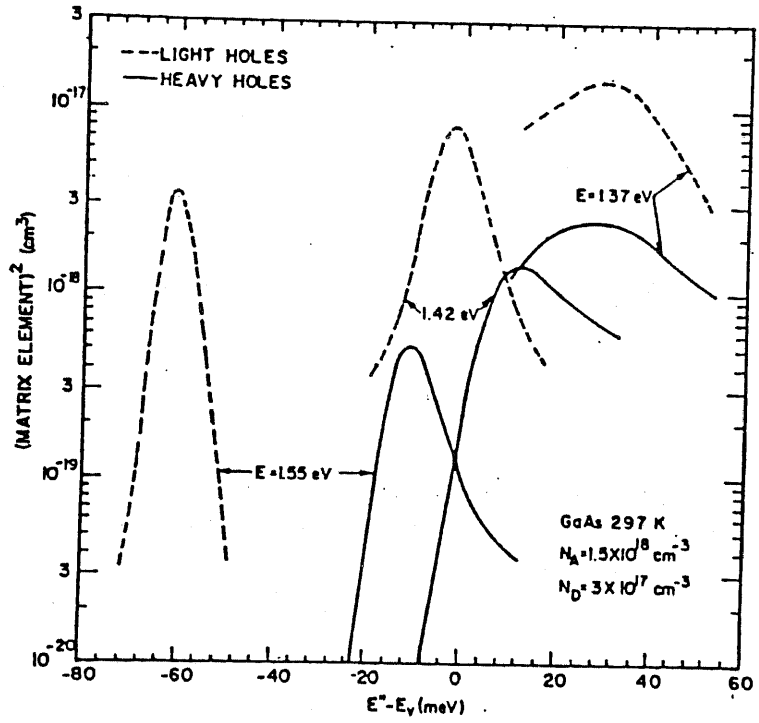

Fig. 3.2(c) Stern's optical matrix element, which describe two different types of optical transitions; the transitions between the parabolic band states for high energies where the *k*-selection rule is obeyed, and those between the band-tail states, giving rise to a constant matrix element. (After reference [4])

In general, the theoretical absorption coefficient calculated using Eq. (3-1) without any fitting parameters is consistently lower than the experimental results by a factor of 1.5 ~ 2.1 [13]. This discrepancy has been believed to be due to electron-hole Coulomb interactions, and contributions from higher bands, both of which act to enhance the optical matrix element. In this work, in order to match the absorption curve to the experimental values measured by Casey and Stern [4], $\alpha(E)$ was multiplied by a constant value of 1.6 to fit the absorption values for high energies.

Starting with an absorption curve for the p-GaAs layer at room temperature with no excitation, $\Delta n = 0$, a set of calculated absorption curves for different free carrier (electron) injection levels Δn, are shown in Fig. 3.3. In this figure, the absorption data calculated for $\Delta n = 3\times10^{17}$, 5×10^{17}, 7×10^{17}, and 10×10^{17} cm^{-3} are shown. It should be pointed out that these curves should differ from those calculated by Mendoza-Alvarez *et al.* [14], only by a constant multiplication factor, since we fitted the theoretical curves to the experimental data. It is observed that the absorption coefficient actually increases for energies below the band-gap for low injection levels up to about $\Delta n = 3\times10^{17}$ cm^{-3}, due to the dominant band-gap shrinkage effect and then starts to decrease as the band-filling effect becomes more predominant for higher injection levels.

3.2.3 Calculation of Refractive Index Variations

The resulting refractive index variation $\Delta\mu$, due to the change in the absorption edge is calculated by using a Kramers-Kronig analysis of the absorption data. The Kramers-Kronig calculation is performed following the approach proposed by Stern [15]. Previously, the same method has been used to evaluate $\Delta\mu$ for the case of a simple parabolic approximation of the density of states in a lightly-doped material, when examining the effect of band-filling in GaAs/AlGaAs DH phase modulators [1]–[2].

The refractive index μ is correlated to the absorption coefficient α by the equation [15],

$$\mu^2(E) - \frac{\lambda^2 \alpha^2(E)}{(4\pi)^2} - 1 = \frac{1}{\pi^2} \int_0^{E_s} \frac{\lambda \mu(E')\alpha(E') E'}{E'^2 - E^2} dE' + \sum_j \frac{G_j}{E_j^2 - E^2} \qquad (3\text{-}14)$$

where G_j and E_j are related to the intensity and energy position of the high-energy peaks in the imaginary part of the dielectric constant. E_s is an arbitrary energy separating the region near the band-

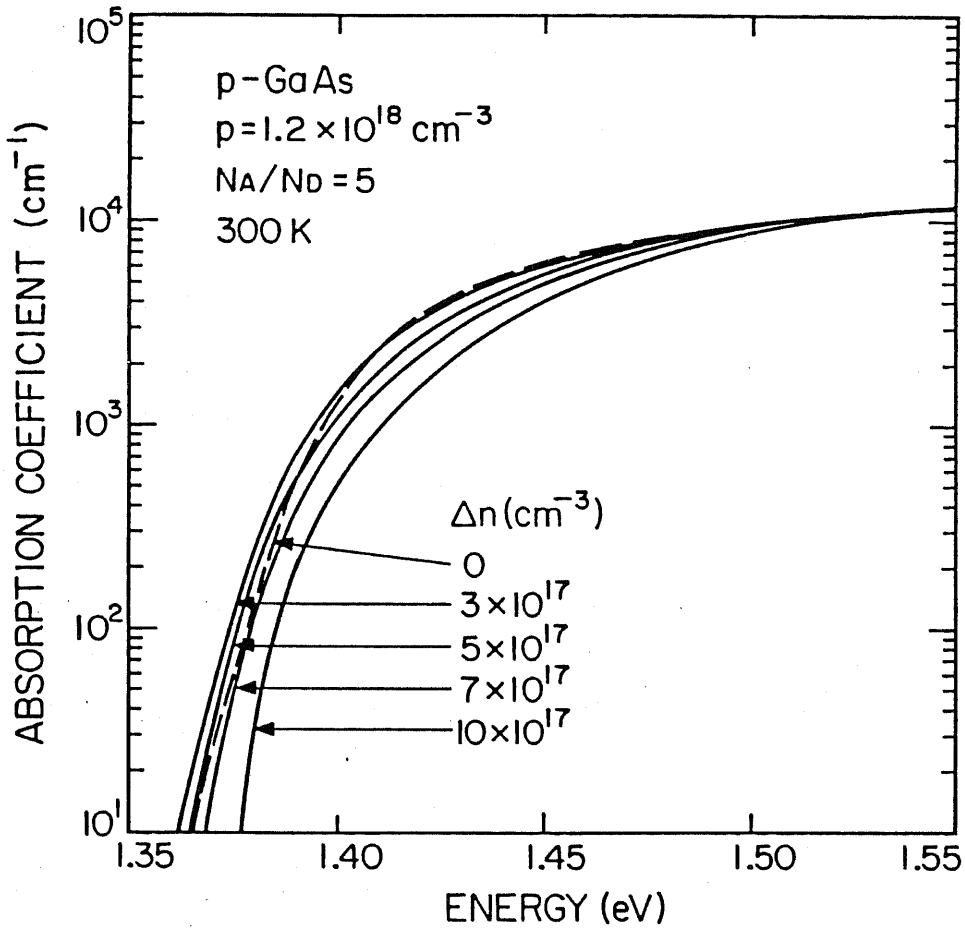

Fig. 3.3 Absorption coefficient versus photon energy at room temperature, calculated using Stern's band-tail model. Different curves are shown corresponding to different injected carrier densities between Δn=0 (no injection) and 10×10^{17} cm^{-3}.

edge from the high-energy region; E_s = 2.86 eV is assumed in this work [15]. The integral in Eq. (3-14) is solved numerically by successive approximations.

Shown in Fig. 3.4 are the results of the refractive index variation as a function of photon energy for different carrier density values in the range 3–10×10^{17} cm^{-3}. It can be observed that for energies below the band-gap, the variation is negative and it decreases as we approach the band-gap energy, reaching a minimum around the band-gap and then increasing to give a positive value of $\Delta\mu$ for energies above the band-gap. Moreover, the refractive index varies almost linearly with injected carrier density in the negative direction for energies below the band-gap, as shown in Fig. 3.5, in which different photon energies between 1.36 and 1.40 eV are plotted. In this figure, the contribution from the plasma dispersion effect due to free carriers to the total index change is also taken into account. It can be observed that $\Delta\mu$ is about -1.35×10^{-2} for $\Delta n = 10\times10^{17}$ cm^{-3}, at an energy of about 1.40 eV.

3.2.4 Comments

Assuming the transistor is driven in the common-base configuration, the emitter current density J_E is given by a charge-control equation,

$$J_E = \frac{q\,\Delta n\, w}{\tau_B} \tag{3-15}$$

where the product $q\Delta n$ and τ_B are the average charge density and the effective lifetime of the injected minority carriers in the base, respectively. w is the base thickness, which is also indicated in Fig. 3.1. If we consider a simple transistor operation, in which the transistor is driven in the saturation region with an open collector and assuming typical values for τ_B = 1 ns (given by the recombination lifetime in this case), and w = 0.3 μm, then $\Delta n = 10\times10^{17}$ cm^{-3} corresponds to $J_E \approx 5$ $kAcm^{-2}$. In fact, a refractive index change $\Delta\mu \approx -1\times10^{-2}$ has been measured experimentally at an injection level $J_E \approx 4.5$ $kAcm^{-2}$ [16]. If the base-collector junction is also forward-biased, then the *net* emitter current density will be smaller to achieve the same carrier density Δn, since the carriers will be injected from both junctions. The switching times are mainly determined by τ_B. For example, if the base-collector junction is reverse-biased at the moment of switch-off, then τ_B is given by the base transit time $\tau_T = w^2 / 2D \approx 5$ ps (where D is the diffusion coefficient of the minority carriers), and therefore a fast switch-off time can be

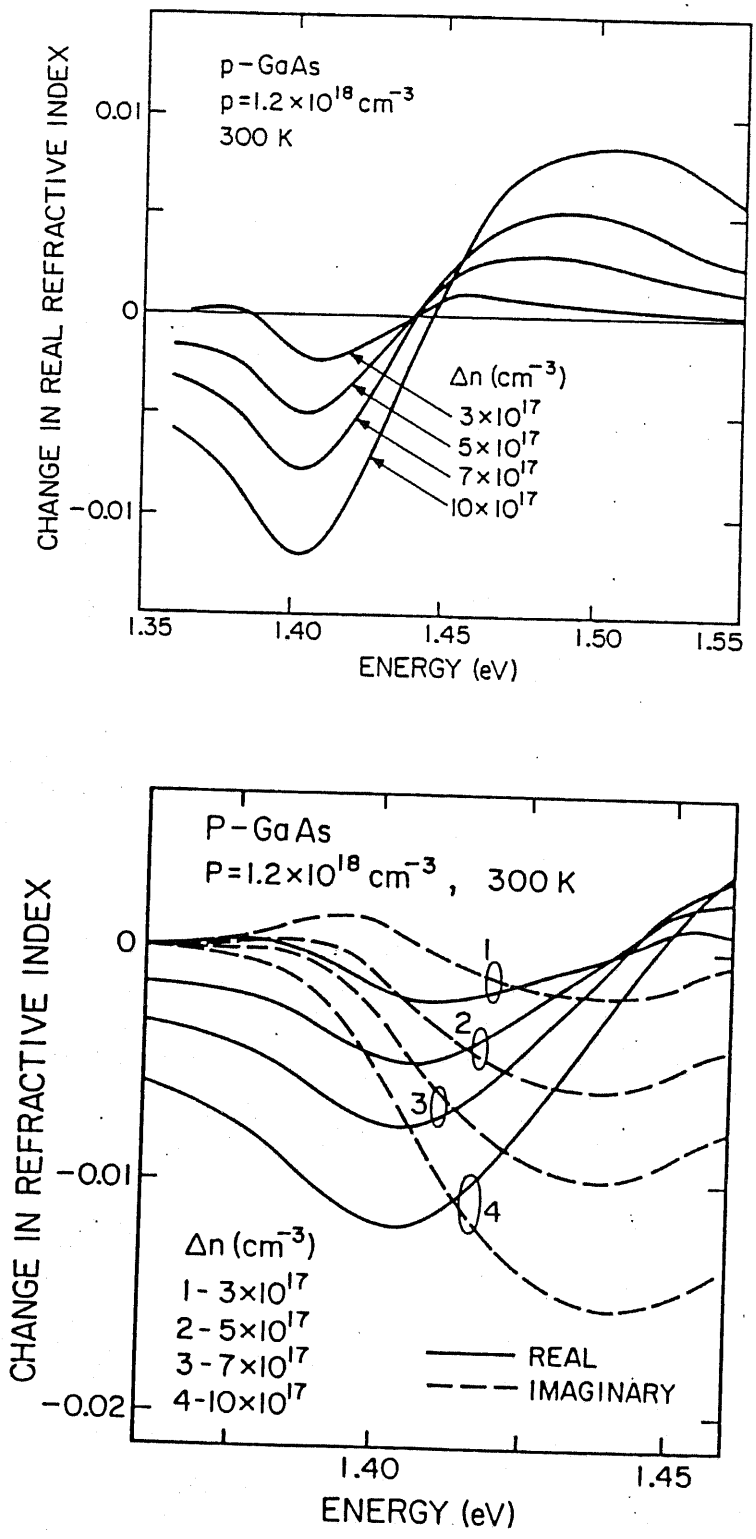

Fig. 3.4 Calculated refractive index variation versus photon energy, obtained from a Kramers-Kronig analysis of the data shown in Fig. 3.3. Different curves shown correspond to different injected carrier densities.

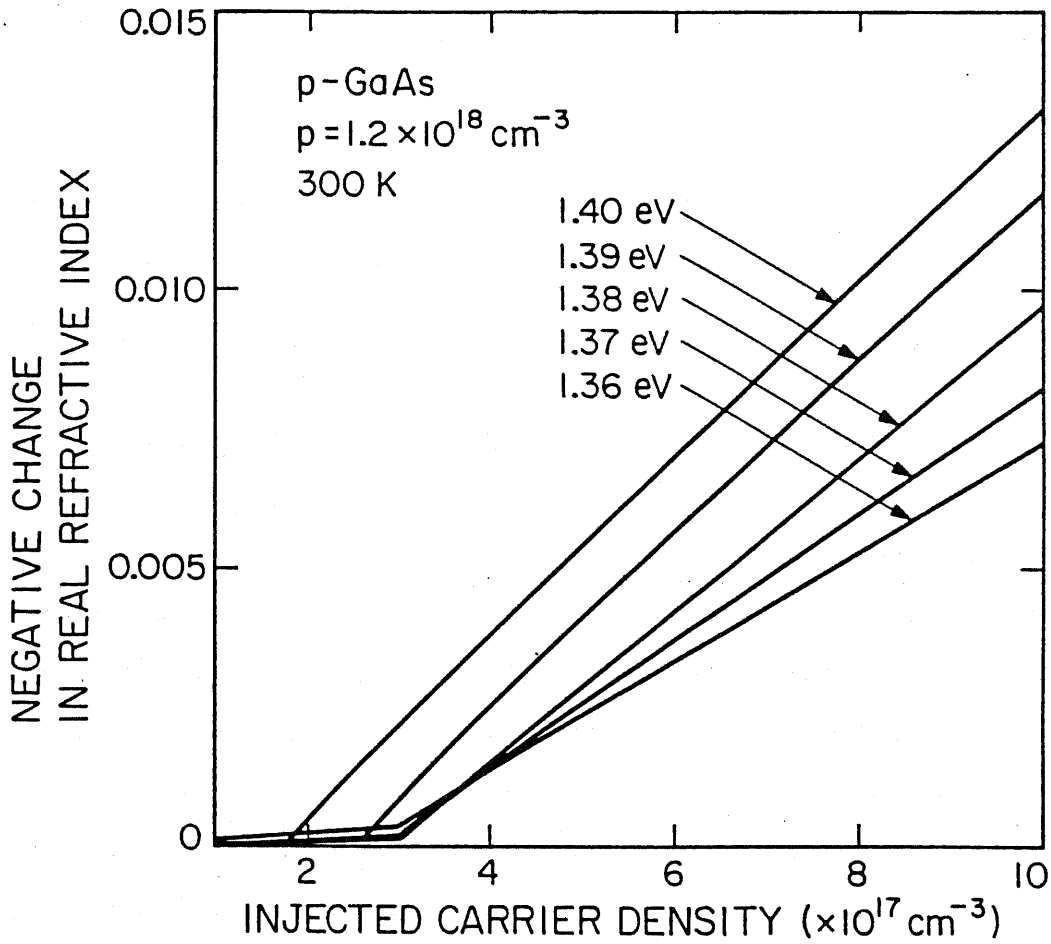

Fig. 3.5 Refractive index change $\Delta\mu$, as a function of injected carrier density Δn, for different photon energies in the range, E=1.36–1.40 eV. $\Delta\mu$ is approximately linear with Δn.

expected.

3.3 Optical Modulation and Switching by Free Carrier Injection

3.3.1 Introduction

In this section, we discuss the operating characteristics of a GaAs/AlGaAs DH bipolar transistor carrier-injected optical modulator/switch based on our calculated results of the free carrier effects on the absorption edge and refractive index. The main advantage of the bipolar transistor structure is that methods such as the rapid removal of stored excess carriers by reverse-biasing the base-collector junction, which are frequently applied in practical transistor circuits for high-speed current switching, can also be applied to optical switching at high speeds. Our previous calculations, as described in Chapter 2, show that for a given structure, the switching times can be as fast as 60 ps or less for the required on-off optical switching, which are two orders of magnitude faster than those expected for a diode structure, whose switching speeds are most often limited by the recombination lifetime of the injected carriers. Recently, it has also been shown that the calculated maximum modulation frequency, which is conventionally achievable with a diode structure in GaAs/AlGaAs system, is limited to about 1 GHz [17]. The amplification nature of transistors also means that large emitter or collector currents can be controlled by small base currents. In these calculations, however, the amount of frequency chirping, losses due to absorption and consequent reduction in achievable modulation depth, which are important practical parameters in these devices that operate in the vicinity of the band-gap energy with large absorption coefficients, have not been evaluated in detail.

3.3.2 Theoretical Analysis

(A) Frequency Chirping

Let us consider a GaAs/AlGaAs DH optical modulator/switch with the bipolar transistor waveguide structure with the same layer doping values as those in Fig. 3.1, a schematic of which is shown in Fig. 3.6. Typical values for the thickness of each of the cladding, waveguide, and buffer layer are assumed. One of the figures of merit that is often used in characterizing an absorption modulator/switch is

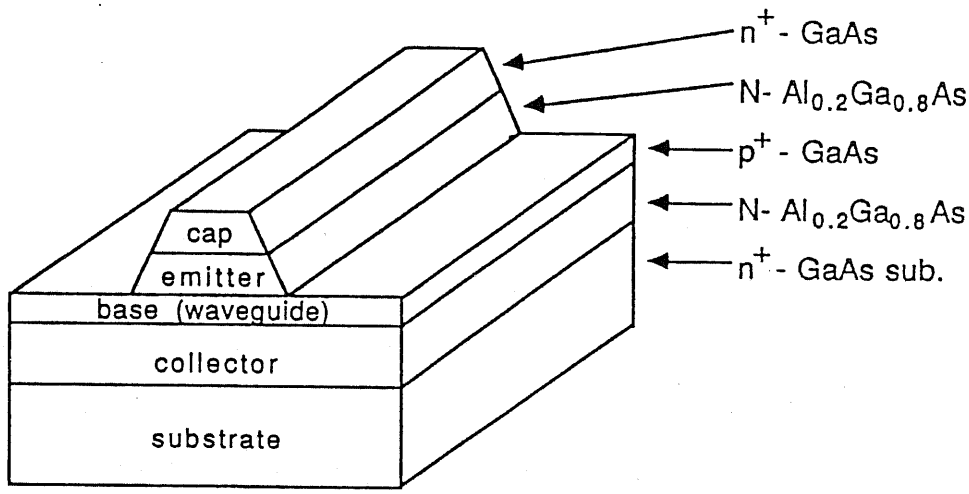

layer	doping (cm^{-3})	thickness (μm)
cap	10^{18}	0.3
emitter	5×10^{17}	0.5
base	10^{18}	0.2-0.3
collector	10^{17}	1.0

Fig. 3.6 A schematic drawing of the DHBT waveguide structure carrier-injected optical modulator/switch. The cross-section is the same as that in Fig. 3.1. Typical device layer parameters are also shown.

the material parameter $\alpha_c = \Delta\mu_{real} / \Delta\mu_{imag}$, which is defined as the ratio of the relative change of the real to imaginary parts of the refractive index. It has been pointed out that, for practical applications, the phase modulation due to the variation of the refractive index, which accompanies the intensity modulation, should be minimized in order to reduce the chirp-like spectral broadening [18]. Furthermore, the α_c-parameter gives a measure of frequency chirping due to the external modulation, equivalent to the chirping of direct laser modulation. Figure 3.7 shows the α_c-parameters calculated for different injection levels in the range $3–10\times10^{17}$ cm^{-3}, for the energy range 1.35–1.55 eV, in the *p*-GaAs waveguide layer. Note that there is an asymptotic transition at around E = 1.41 eV for $\Delta n = 3\times10^{17}$ cm^{-3} because $\Delta\mu_{imag} \approx 0$ around this energy. It is also observed that at around E = 1.44 eV, a maximum absorption modulation $\Delta\alpha$ of as large as ~ 2000 cm^{-1} can be obtained with $\Delta n = 10\times10^{17}$ cm^{-3}, with a small α_c-parameter of less than 1. However, the magnitude of the absorption coefficient is ~ 3000 cm^{-1} and therefore operation of the waveguide modulator at such energies would not be convenient because the absorption losses, even after the carrier injection, is too large in the GaAs waveguide layer for those energies.

Furthermore, the switching waveform of the carrier density in the waveguide layer will not be an ideal step-like shape in practice, but rather, it is characterized by finite rise and fall times. Even if a bipolar transistor structure is employed, leading to rise and fall times that are shorter by two orders of magnitude as compared to a diode structure, these on-off times will be still on the order of about 10 ~ 100 ps range (assuming the common-base configuration), which means a continuous variation of the carrier density during the transient times. It is therefore important to investigate the effect of injected free carriers on the absorption and refractive index variations at every moment of the modulation including the transient times. Hence, we use a more convenient figure of merit parameter β_c, similar to the parameter α' defined by Kan *et al.* [19]. β_c is defined as the ratio of the refractive index variation to the extinction coefficient variation due to a small free carrier density modulation,

$$\beta_c = (d\mu / dn) / (dk / dn) \tag{3-16}$$

where the extinction coefficient k is given by $k = \alpha\lambda/4\pi$, and α is the absorption coefficient. Thus, we want to minimize the β_c-parameter while keeping the obtainable carrier-induced absorption variation as large as possible, over the entire modulation period. Note that the β_c-parameter should be distinguished from those defined in Eqs. (3-10)-(3-13). Figure 3.8 shows plots of the theoretical β_c-parameters for injection levels in the range $3–10\times10^{17}$ cm^{-3}. At about E = 1.40 eV, β_c is less than 1 during the entire

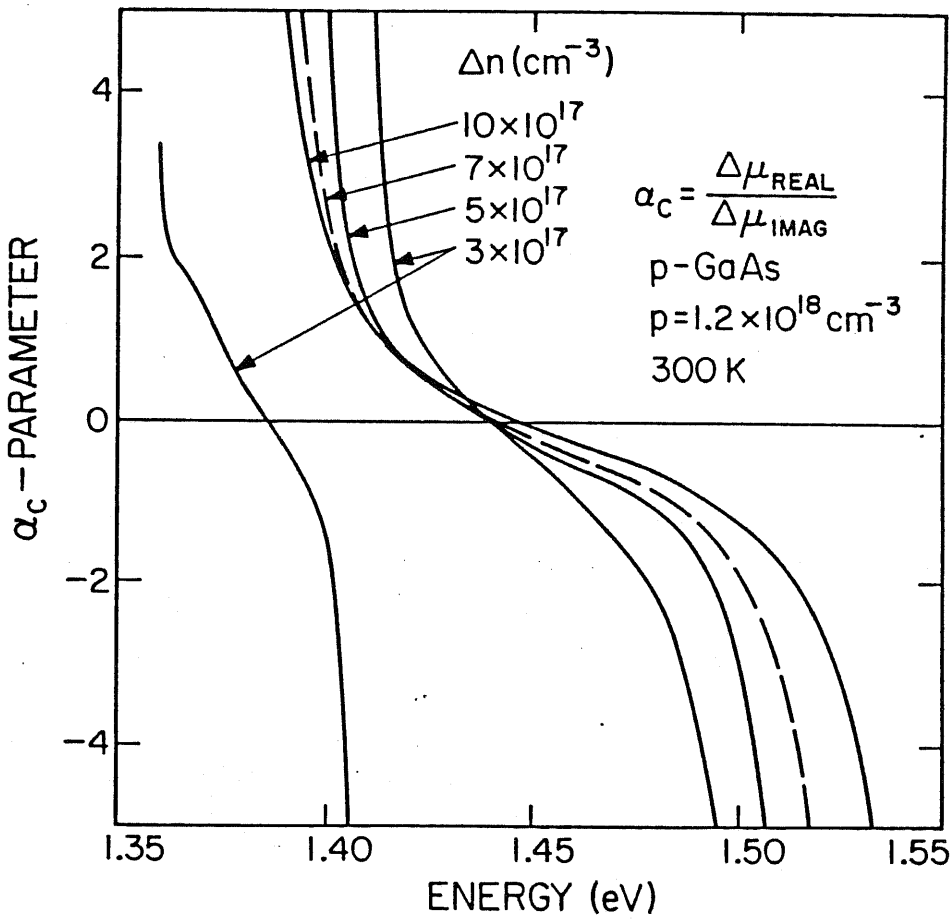

Fig. 3.7 α_c-parameter as a function of photon energy, calculated for different injected carrier densities in the range, $\Delta n = 3\text{–}10\times10^{17}$ cm^{-3}.

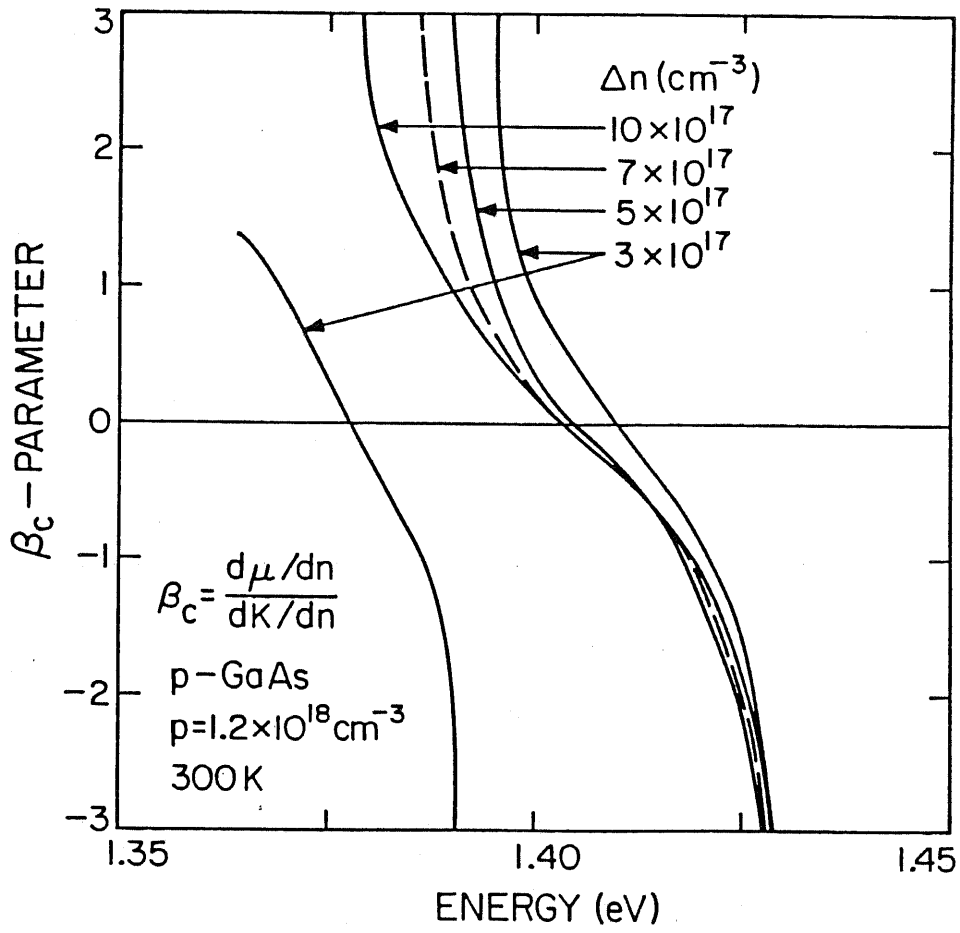

Fig. 3.8 β_c-parameter as a function of photon energy, calculated for different injected carrier densities in the range, $\Delta n = 3\text{–}10\times10^{17}$ cm^{-3}.

modulation, when the carrier density is modulated between $\Delta n = 3\times10^{17}$ and 10×10^{17} cm^{-3}. The value is much smaller than the measured linewidth enhancement factor for direct modulation of an injection laser diode, which was ~ 3 [20]. It is also observed that the β_c-parameter is strongly energy-dependent and changes rapidly at around $E = 1.40$ eV, reaching a value of ~ 2 at $E \approx 1.39$ eV.

(B) Modulation Depth and Absorption Losses

In selecting the optimum wavelength or a range of wavelengths for the external optical modulator/switch, we should also consider the maximum modulation depth or the extinction ratio, m, and the magnitude of the absorption coefficient itself, which can be obtained before and after the injection of carriers. Figure 3.9 (a) through (d) show the changes in the relative output power of the modulated beam, measured in dB, as the carrier injection level is varied from $\Delta n = 0$ to 10×10^{17} cm^{-3}, and calculated for photon energies $E = 1.37$, 1.38, 1.39, and 1.40 eV. In each figure, the results are plotted for a different effective modulator length ΓL, which is the product of the optical confinement factor Γ of the waveguide and length of the modulator L in the direction of the beam, calculated for $\Gamma L = 10$, 20, 30, 40, 50, and 100 μm. Figure 3.10 shows 2 sets of data; the maximum modulation depth m, obtainable when the carrier density is modulated between $\Delta n = 3\times10^{17}$ and 10×10^{17} cm^{-3}, and the relative power of the modulated output P_{on}, measured in dB, at an injection level $\Delta n = 10\times10^{17}$ cm^{-3}, both plotted as a function of effective modulator length ΓL. From the viewpoint of electrical device characteristics, the longer the interaction length, the larger the area of the base-collector junction, resulting in a larger junction capacitance and slower modulation speeds. Hence the effective length of the modulator/switch should be as short as possible.

Several important conclusions can be drawn from the results in Fig. 3.9 and Fig. 3.10, and from the β_c-parameter calculations as of Fig. 3.8. Firstly, it is observed that at $E = 1.37$ eV, a transition from the region of absorption to gain can be obtained above an injection density of about 9×10^{17} cm^{-3}, resulting in an amplification of the optical power. However, the maximum depth of modulation m, which can be obtained when the carrier density is modulated between $\Delta n = 3\times10^{17}$ and 10×10^{17} cm^{-3}, is rather small for useful practical applications. For $\Gamma L = 100$ μm, m is only about 2.5 dB, though $P_{on} \approx +0.38$ dB. Also the β_c-parameter becomes very large above $\Delta n = 3\times10^{17}$ cm^{-3}, which may not be suitable for high-speed operation.

Secondly, for a fixed confinement factor Γ and injection density Δn, the longer the modulator

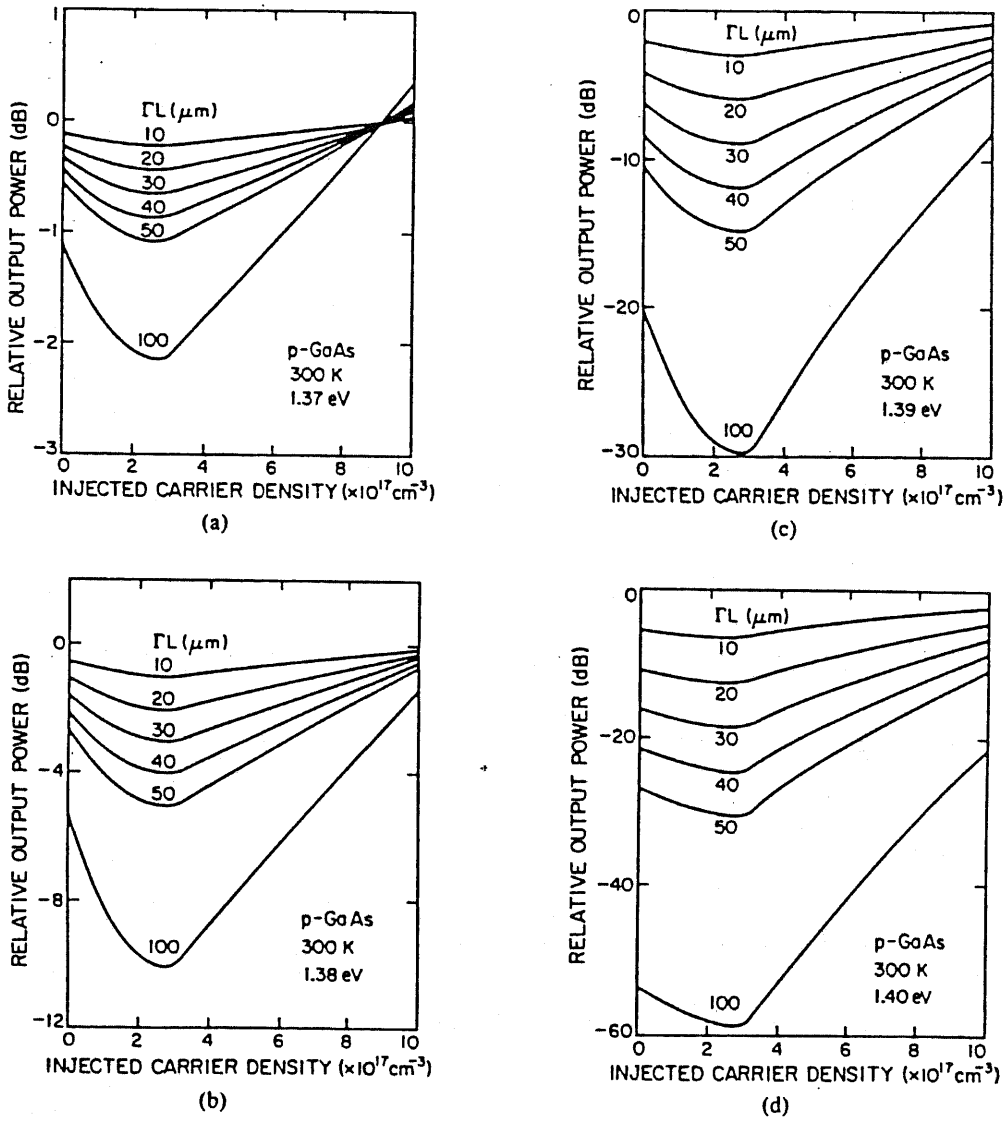

Fig. 3.9 Calculated relative output power as a function of injected carrier density for different photon energies; (a) E=1.37 eV, (b) E=1.38 eV, (c) E=1.39 eV, and (d) E=1.40 eV. In each figure, different curves are shown corresponding to different effective modulator lengths in the range, ΓL= 10–100 μm.

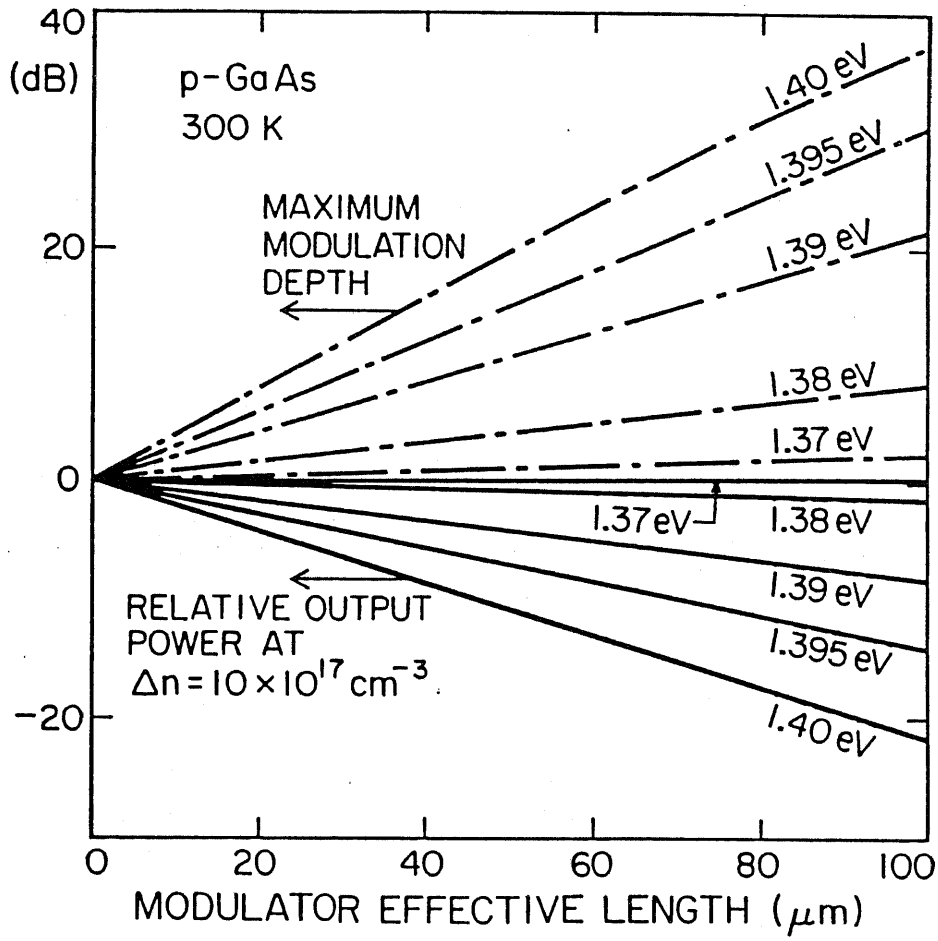

Fig. 3.10 The calculated maximum modulation depth when injected carrier density is modulated between $\Delta n = 3$ and 10×10^{17} cm^{-3}, and the relative modulator output power at $\Delta n = 10\times10^{17}$ cm^{-3}, both as a function of effective modulator length. Different curves are shown corresponding to different photon energies in the range E=1.37–1.40 eV.

Table III-1 Some of the numerical values of the optical modulation characteristics, obtained from the figures 3.9 an 3.10.

Energy E (eV)	Modulator Effective Length ΓL (μm)	Maximum Modulation Depth m (dB)	Relative Output Power P_{on} (dB)
1.37	20	0.5	0.08
	100	2.5	0.38
1.38	20	1.7	-0.28
	100	8.6	-1.4
1.39	20	4.3	-1.6
	100	22	-8.2
1.395	20	6.0	-2.8
	100	30	-14
1.40	20	7.9	-4.3
	100	37	-22

length L, the larger the interaction between the confined optical field and the changes in the absorption, resulting in a larger value of m. Also, m is higher at energies near the band-gap, since the changes in the absorption coefficient are very large at these energies. However, a significant portion of the optical power may be lost in the modulator due to the large magnitude of the absorption coefficient. Moreover, these characteristics are strongly energy dependent and some of the numerical values obtained from Fig. 3.9 and 3.10 are listed in Table III-1. For example, for ΓL = 100 μm and $\Delta n = 10\times10^{17}$ cm^{-3}, $\alpha \approx 32$ cm^{-1} corresponding to $m \approx 8.6$ dB and $P_{on} \approx +1.4$ dB at E = 1.38 eV. At E = 1.40 eV, however, $\alpha \approx 320$ cm^{-1}, which is an order of magnitude greater than at E = 1.38 eV, resulting in $m \approx 30$ dB and $P_{on} \approx -14$ dB for ΓL = 100 μm. The values of the β_c-parameter lie in the region of about 0.5 ~ 3 at these photon energies, and hence small frequency chirping can be expected.

It is therefore concluded that the optimum photon energy and effective modulator length to be used for optical modulation in our DH optical modulator/switch, with the HBT waveguide structure characterized by a relatively heavy-doped p-GaAs base or waveguide layer, would be E = 1.38 eV (λ = 899 nm) and ΓL = 100 μm, resulting in a maximum modulation on-off ratio of about 8 : 1, with a sufficiently high value of $P_{on}/P_{in} \approx 0.72$ (−1.4 dB), at an injected carrier density $\Delta n = 10\times10^{17}$cm^{-3}.

3.4 Conclusions

In conclusion, using a band-tail model to calculate the absorption coefficient and a Kramers-Kronig analysis to calculate the refractive index, the contribution of the band-filling effect and band-gap shrinkage effect on the absorption coefficient and the refractive index variations due to free carrier injection, which take place in the heavily-doped p-GaAs region of a N-p-N AlGaAs/GaAs DH bipolar transistor optical modulator/switch have been evaluated in detail. It is found that large absorption and refractive index changes can be obtained at photon energies below the band-gap. The advantages of the bipolar transistor structure compared to conventional diode structures are also briefly discussed, though a more comprehensive description can be found in the previous chapter.

The calculated results are analyzed on the basis of the maximum depth of modulation, absorption losses, and figures of merit, α_c-parameter and β_c-parameter, which determine the degree of spectral broadening that can take place as a result of simultaneous refractive index change with the absorption change. It is concluded that a carrier-injected optical modulator/switch which is almost free from frequency

chirping with low absorption loss can be realized, if the photon energy is properly chosen for the modulation. The device characteristics, however, are expected to be strongly dependent on the operating wavelength among other parameters, and therefore, it is necessary to select the optimum conditions precisely. The optimum photon energy and effective modulator length to be used for optical modulation in our DHBT optical modulator/switch are determined to be E = 1.38 eV (λ = 899 nm) and ΓL = 100 μm, which will result in a maximum modulation on-off ratio m of about 8 : 1 when the carrier density in the waveguide layer is modulated between $\Delta n = 3\times10^{17}$ and 10×10^{17} cm^{-3}. Furthermore, a sufficiently high value of $P_{on} / P_{in} \approx 0.72$ (−1.4 dB), can be obtained at an injected carrier density $\Delta n = 10\times10^{17} cm^{-3}$. These results indicate that our DHBT optical modulator/switch may find very useful applications in optical communication and processing systems.

References

[1] J. G. Mendoza-Alvarez, R. H. Yan, and L. A. Coldren, "Contribution of the band-filling effect to the effective refractive-index change in double-heterostructure GaAs/AlGaAs phase modulators", *J. Appl. Phys.*, vol. 62, p. 4548, 1987.

[2] J. G. Mendoza-Alvarez, L. A. Coldren, A. Alping, R. H. Yan, T. Hausken, K. Lee, and K. Pedrotti, "Analysis of depletion edge translation lightwave modulators", *IEEE J. Lightwave Technology*, vol. LWT-6, p. 793, 1988.

[3] F. Stern, "Band-tail model for optical absorption and for the mobility edge in amorphous silicon", *Phys. Rev.*, vol. B3, p. 2636, 1971.

[4] H. C. Casey and F. Stern, "Concentration-dependent absorption and spontaneous emission of heavily doped GaAs", *J. Appl. Phys.*, vol. 47, p. 631, 1976.

[5] E. O. Kane, "Thomas-Fermi approach to impure semiconductor band structure", *Phys. Rev.*, vol. 131, p. 79, 1963.

[6] B. I. Halperin and M. Lax, "Impurity-band tails in the high-density limit. I. Minimum counting methods", *Phys. Rev.*, vol. 148, p. 722, 1966.

[7] C. J. Hwang, "Properties of spontaneous and stimulated emission in GaAs in GaAs junction lasers. I. Densities of states in the active regions", *Phys. Rev.*, vol. B2, p. 4117, 1970.

[8] J. R. Lowney, "Impurity bands and band tailing in *n*-type GaAs", *J. Appl. Phys.*, vol. 60, p. 2854, 1986.

[9] F. Ermanis and K. Wolfstirn, "Hall effect and resistivity of Zn-doped GaAs", *J. Appl. Phys.*, vol. 37, p. 1963, 1966.

[10] H. Kroemer, "Theory of a wide-gap emitter for transistors", *Proc. IRE*, vol. 45, p. 1535, 1957.

[11] H. Kroemer, "Heterostructure bipolar transistors and integrated circuits", *Proc. IEEE*, vol. 70, p. 13, 1982.

[12] G. Lasher and F. Stern, "Spontaneous and stimulated recombination radiation in semiconductors", *Phys. Rev.*, vol. 133, p. A553, 1964.

[13] H. C. Casey and M. B. Panish, *Heterostructure Lasers Part A*, Academic Press, New York, 1978.

[14] J. G. Mendoza-Alvarez, F. D. Nunes, and N. B. Patel, "Refractive index dependence on free carriers for GaAs", *J. Appl. Phys.*, vol. 51, p. 4365, 1980.

[15] F. Stern, "Dispersion of the index of refraction near the absorption edge of semiconductors", *Phys. Rev.*, vol. 133, p. A1653, 1964.

[16] K. Ishida, H. Nakamura, H. Matsumura, T. Kadoi, and H. Inoue, "InGaAsP/InP optical switches using carrier induced refractive index change", *Appl. Phys. Lett.*, vol. 50, p. 141, 1987.

[17] K. Tada, J. Hashimoto, and Y. Nakano, "Effects of facet reflection in a monolithically integrated optical device consisting of a DFB laser and an amplifier/modulator", *Technical Digest of the Topical Meeting on Integrated and Guided-Wave Optics*, Santa Fe, p. 219, 1988.

[18] F. Koyama and K. Iga, "Frequency chirping of external modulation and its reduction", *Electron. Lett.*, vol. 21, p. 1065, 1985.

[19] Y. Kan, H. Nagai, M. Yamanishi, and I. Suemune, "Field effects on the refractive index and absorption coefficient in AlGaAs quantum well structures and their feasibility for electrooptic device applications", *IEEE J. Quantum Electron.*, vol. QE-23, p. 2167, 1987.

[20] I. D. Henning and J. V. Collins, "Measurements of the semiconductor laser linewidth enhancement factor", *Electron. Lett.*, vol. 19, p. 927, 1983.

CHAPTER 4

DEVICE FABRICATION AND MEASUREMENT OF ELECTRICAL AND OPTICAL MODULATION CHARACTERISTICS

4.1 Introduction

The advantages of a wide-gap emitter bipolar transistor such as high emitter injection efficiency and hence high current gain, were first discussed in detail by Kroemer [1]. Early work on single heterojunction bipolar transistors (HBTs) employed material systems such as GaAs-Ge [2] and ZnSe-Ge [3]. Current gains typically obtained with these materials were only about 1 ~ 40, which were mainly attributed to the lattice mismatch at the emitter-base heterojunction interface resulting in low emitter injection efficiencies. High-quality heterojunction interfaces can be obtained in GaAs/AlGaAs system for example, because of the small lattice mismatch of GaAs and AlGaAs. Exploitation of the advantages of GaAs/AlGaAs heterojunctions, however, was not practically possible until the advent of liquid phase epitaxy (LPE). Using this technique, HBTs with greatly improved characteristics have been successfully demonstrated [4]–[8]. Unfortunately, the thicknesses, doping levels, and uniformities of the epitaxial layers grown by LPE, were not considered good enough in order to produce integrated circuits and/or extremely thin base thicknesses on a manufacturing basis.

Most recently, with advances in molecular beam epitaxy (MBE) and metal-organic vapor phase epitaxy (MOVPE), it has become possible to obtain extremely precise control of doping and composition profiles with excellent uniformity across the wafer and wafer-to-wafer producibility. The recent surge in activity in the area of HBTs is largely due to these crystal growth capabilities; the energy band diagram of the HBT's may now be tailored almost at will in order to optimize the device performance.

In this chapter, an emphasis is placed on the process technology employed for the fabrication of a GaAs/AlGaAs double-heterojunction bipolar transistor (DHBT) waveguide structure carrier-injected optical intensity modulator/switch grown by MBE, and on the characterization of the device performance, particularly the electrical properties and optical modulation characteristics of the DHBT waveguide structure. The results are also applied to design, compute, and analyze the characteristics expected for a

reflection-type optical switch, as discussed in Chapter 2, by use of the DHBT waveguide structure.

4.2 Fabrication Procedures

The following experimental procedures have been taken for the fabrication of the DHBT single-waveguide carrier-injected optical intensity modulator/switch, whose schematic structure is as shown in Fig. 4.1, and a set of layer parameters are listed in Table 4-I. The process flow is also depicted in the form of a flow-chart as shown in Fig. 4.2.

(1) *Crystal Growth*

The 10-epilayer structure was grown on an (100)-oriented n^+-GaAs (Si-doped to 1×10^{18} cm^{-3}) substrate by molecular beam epitaxy (MBE). An n^+-GaAs buffer layer (Si-doped to 1×10^{17} cm^{-3}, 0.3 μm) was first grown directly on the substrate. This buffer layer was used to equilibrate the growth and to reduce the effects of the relatively poor substrate-epilayer interface on the more critical collector, base, and emitter layers. Then a 500 Å-thick $(AlAs)_5$ / $(GaAs)_5$ 20-period superlattice structure, which was aimed to trap the defects was grown. It was followed by an N-$Al_{0.2}Ga_{0.8}As$ collector layer (Si-doped to 1×10^{17} cm^{-3}, 0.5 μm), a compositionally graded collector layer, a spacer layer, a p^+-GaAs base layer (Be-doped to 1×10^{18} cm^{-3}, 0.2 μm), a spacer layer, a graded emitter layer, an N-$Al_{0.2}Ga_{0.8}As$ emitter layer (Si-doped to 1×10^{17} cm^{-3}, 0.3 μm), and finally, an n^+-GaAs cap layer (Si-doped to 2×10^{18} cm^{-3}, 0.1 μm). The base has been designed to be relatively thick compared to the conventional HBTs [9], since it also serves as a single-mode optical waveguide with almost an unity optical confinement factor. Furthermore, the collector-base and emitter-base heterojunctions have graded energy-band configurations in order to prevent the occurrence of "spikes", which would adversely affect the injection and collection of minority carriers [1]. A schematic illustration depicting this situation is shown in Fig. 4.3, and the Al fraction and the grading width employed for both the collector and emitter regions were 0.2 and 400 Å, respectively. Undoped GaAs spacer layers of 200 Å were inserted between the collector and base, and the emitter and base to allow for the redistribution of Be during the growth of the emitter layers [10]. The substrate temperature was kept at 650 °C during the entire growth period.

For the grading region, the temperature of the Al-cell was linearly varied with time, which resulted in typical measured Al-flux variations as shown in Fig. 4.4. In our present MBE system, the temperatures of each Knudsen cell are controlled by a computer algorithm following the concepts of

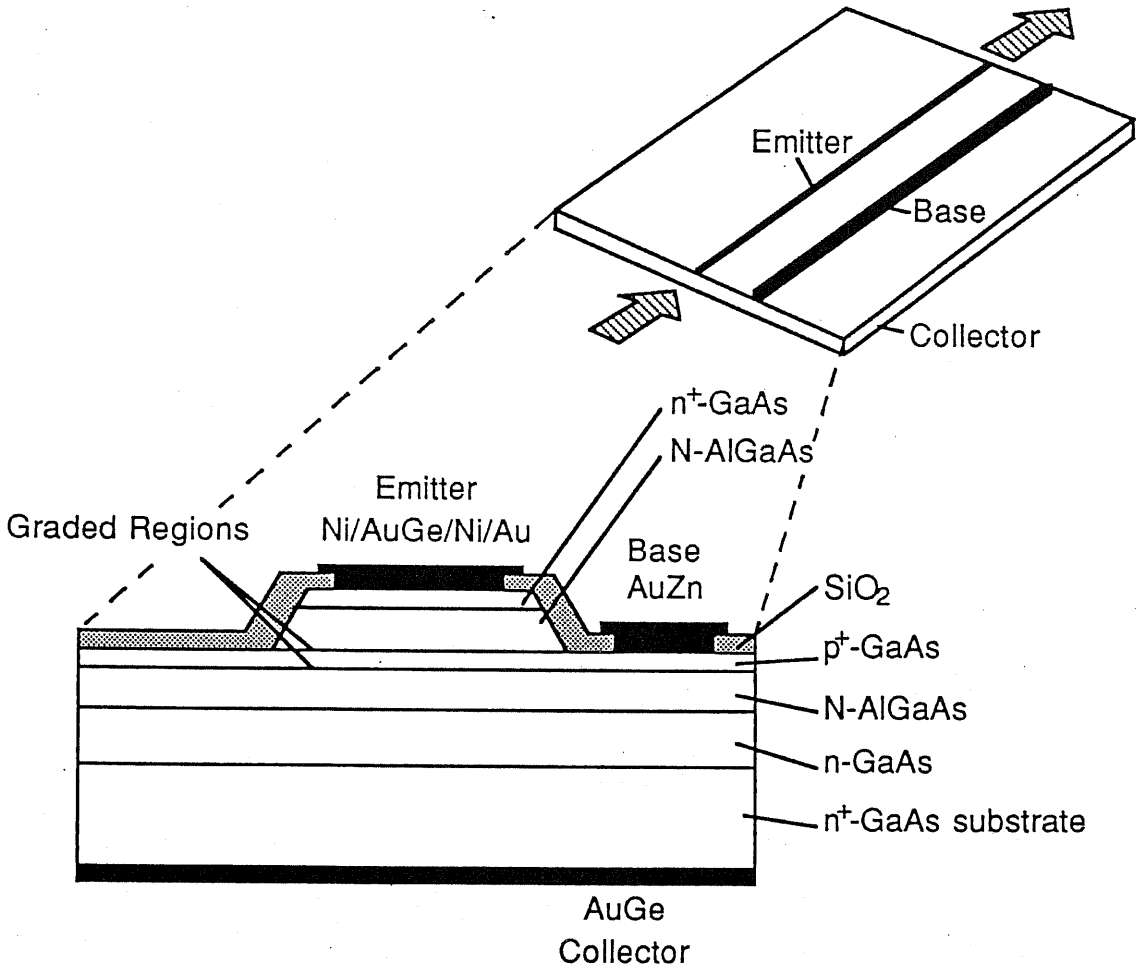

Fig. 4.1 A schematic diagram of the DHBT waveguide structure carrier-injected optical intensity modulator. Both the emitter-base and the base-collector heterojunctions have graded energy-band configurations in order to prevent the occurrence of spikes, which would adversely affect the injection and collection of minority carriers (Also see Fig. 4.3). The emitter/waveguide is 7 μm wide and 190 μm long, and arrows indicate light focused into and emerging from the optical modulator.

Table 4-I A set of layer parameters grown by MBE for the DHBT waveguide structure carrier-injected optical intensity modulator as of Fig. 4.1.

Layer	Al Fraction	Thickness (Å)	Type	Concentration ($\times 10^{18}$ cm^{-3})
Cap	0	1000	n^+	2.0
Emitter	0.2	3000	n	0.1
Grading	0.2→0.05	400	n	0.1
Spacer	0	200	undoped	....
Base	0	2000	p^+	1.0
Spacer	0	200	undoped	....
Grading	0.05→0.2	400	n	0.1
Collector	0.2	5000	n	0.1
Superlattice Buffer		500	n	0.1
Buffer	0	3000	n	0.1
Substrate	0	....	n^+	1.0

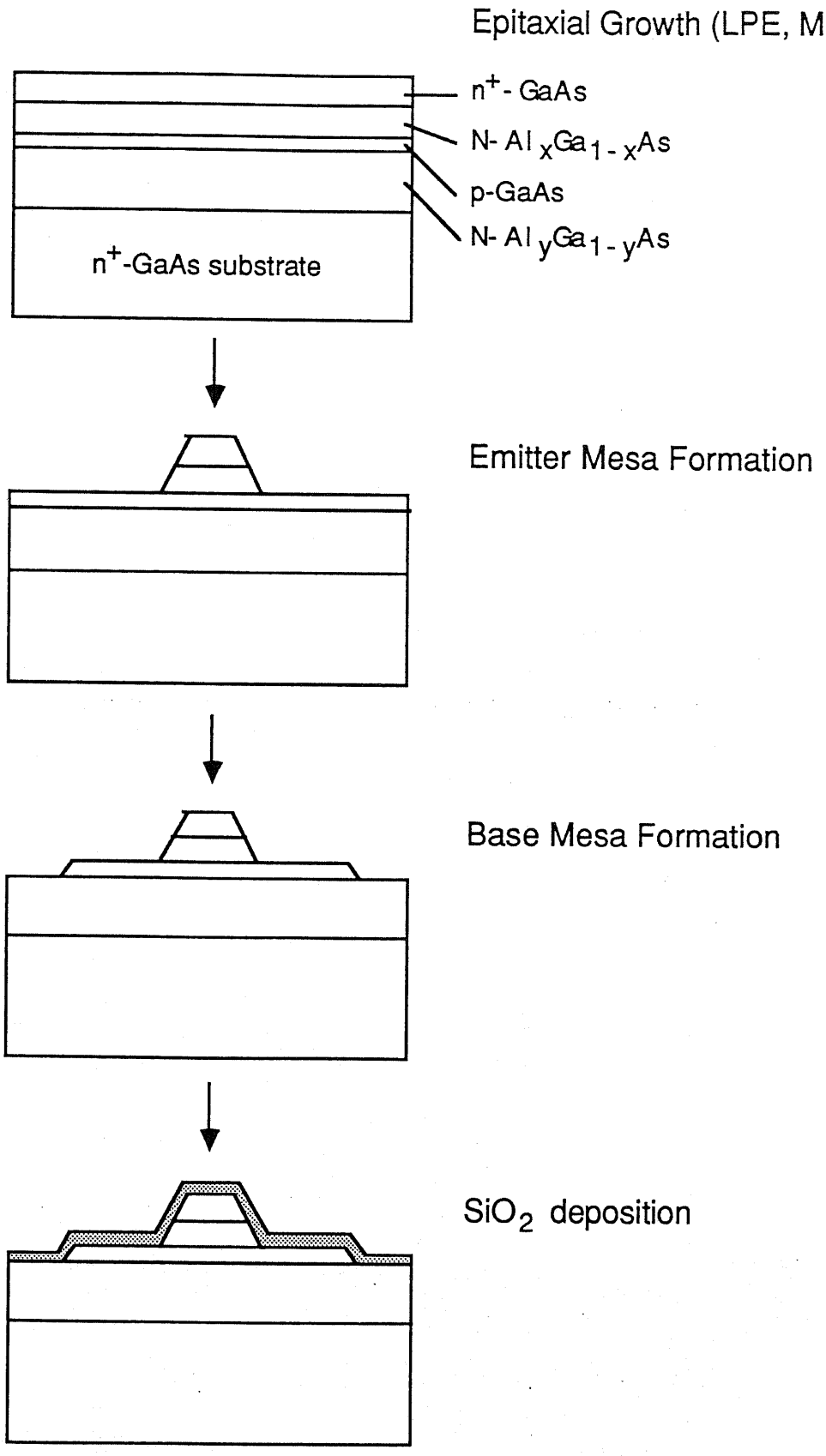
Epitaxial Growth (LPE, MBE)
n+- GaAs
N- Al xGa1 - xAs
p-GaAs
N- Al yGa1 - yAs
n+-GaAs substrate
Emitter Mesa Formation
Base Mesa Formation
SiO2 deposition

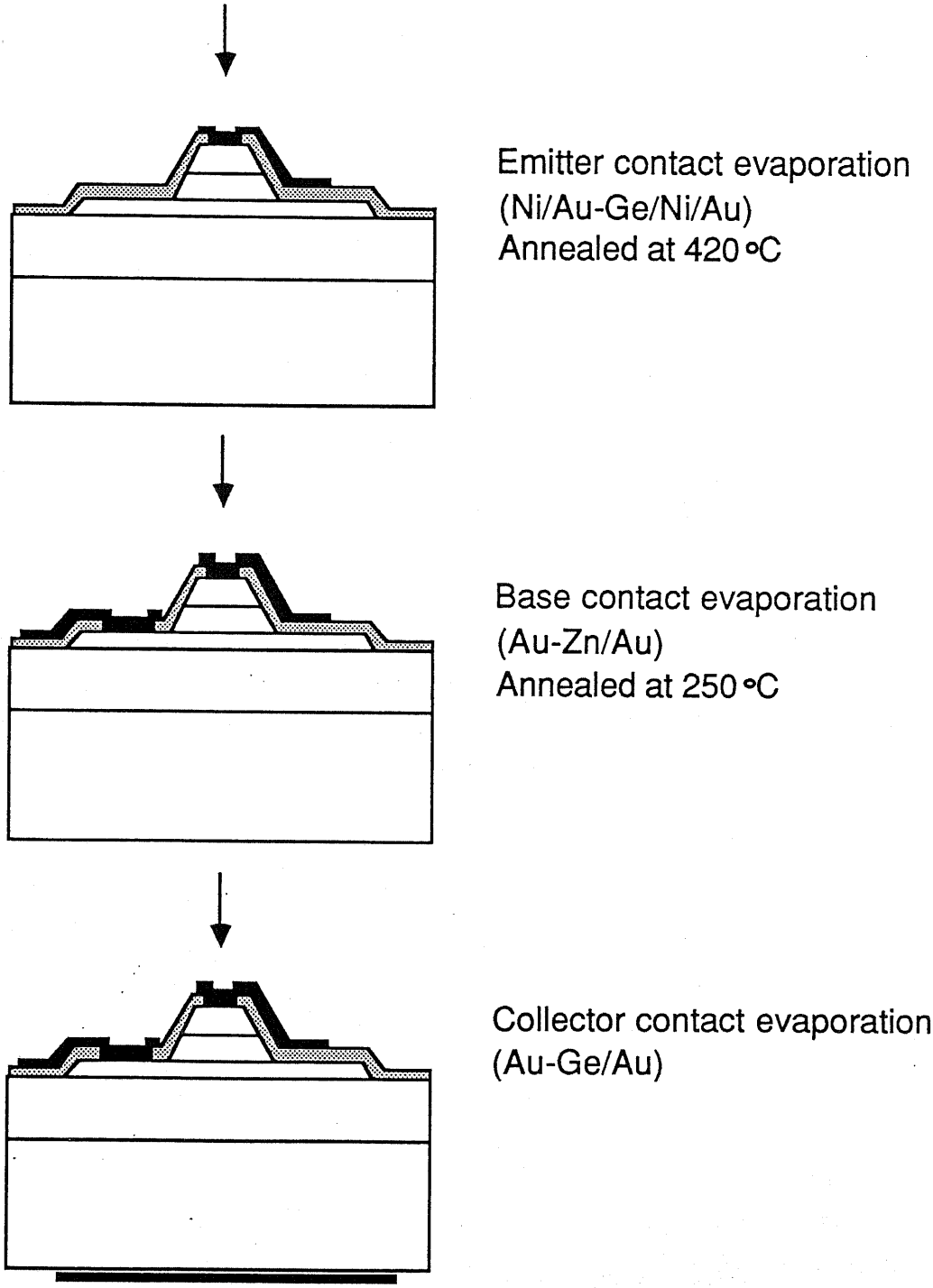

Fig. 4.2 Experimental procedures for the fabrication of the DHBT structure.

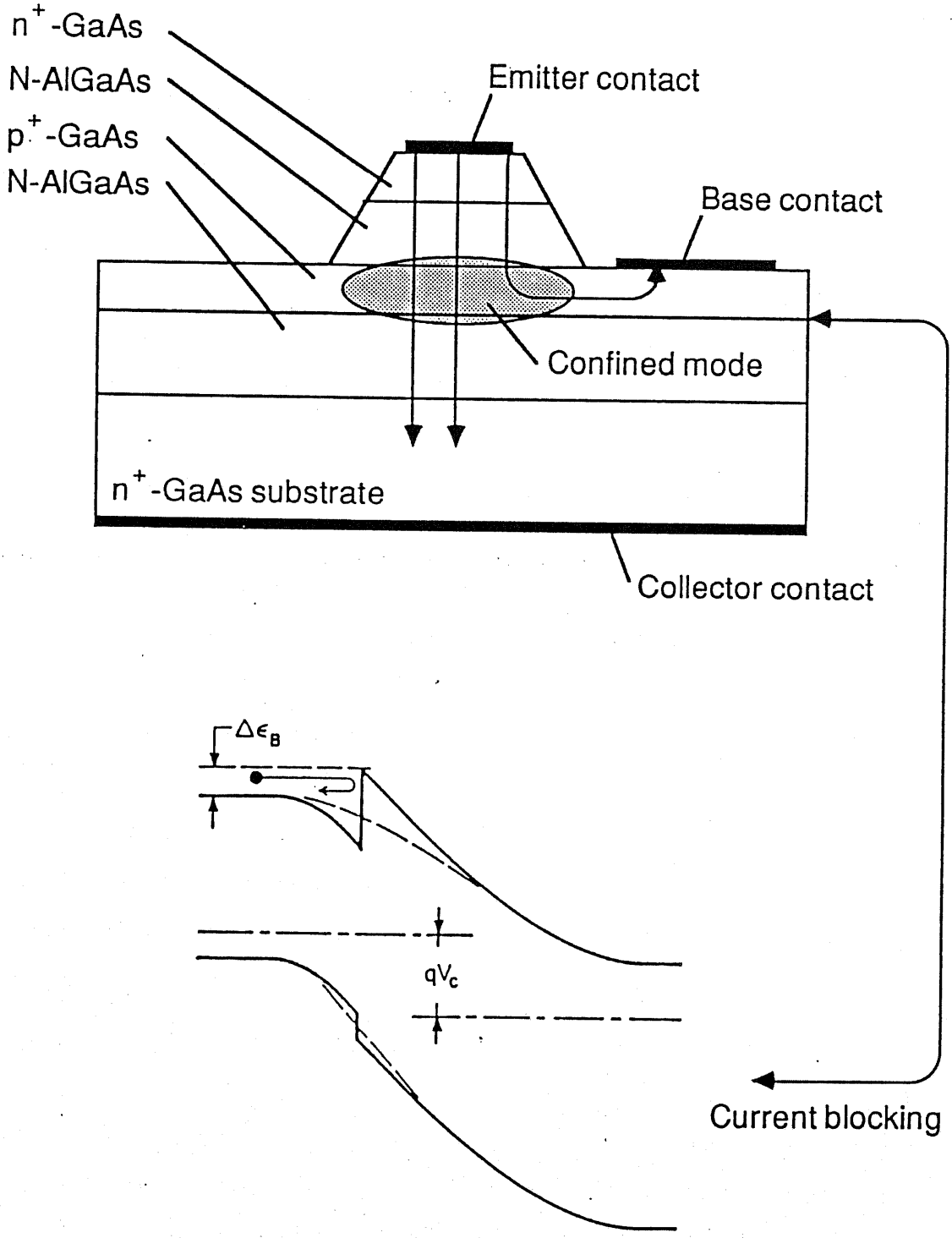

Fig. 4.3 A schematic illustration of the current blocking expected at an abrupt heterojunction of the base-collector interface. (After reference [1])

modern control theory rather than the conventional PID algorithm, and it has been shown that the cell temperatures follow very closely to the time-varying set temperatures [11]. Therefore, the energy band profiles of the compositionally graded AlGaAs regions should be of almost the same shape as the measured Al-flux profiles shown in Fig. 4.4.

(2) *Emitter Mesa Formation*

Indium on the backside of the substrate was first removed in hydrochloric acid (HCl) and the wafer was lapped down to a thickness of about 320 μm. The emitter mesa was formed by first patterning the corresponding area using a positive photoresist (OFPR-800, 50 cp) by standard photolithographic methods. The practical conditions employed with the OFPR-800 photoresist were as follows;

(i) Spin-on at 500 rpm for 5 seconds, followed by 6000 rpm for 30 seconds.

(ii) Prebake in dry air at 90 °C for 30 minutes.

(iii) Exposure under UV mercury lamp for the required time (system-dependent).

(iv) Development in the NMD-3 Developer for 60 seconds.

(v) Rinse in distilled water for 60 seconds.

(vi) Postbake in dry air at 120 °C for 30 minutes.

Using the photoresist as an etch mask, the GaAs cap layer and the AlGaAs emitter/cladding layer were then etched off using $H_3PO_4 : H_2O_2 : H_2O = 4 : 1 : 50$ solution, at least 15 minutes after the solution has been prepared. The measured etch-rate of GaAs using this solution is about 700 Å/min at the ambient temperature, as shown in Fig. 4.5. For $Al_xGa_{1-x}As$, the etch-rate is about 30% more for $x \sim 0.2$. Finally, the photoresist was removed in acetone.

(3) *Base Mesa Formation*

The base region was formed by the same experimental procedure as for the emitter mesa formation. The mask alignments have been achieved within an error of ± 1 μm hereafter.

(4) *SiO_2 Deposition*

After the usual degreasing cycle, a SiO_2 insulating film of 1500 ~ 2000Å thickness was deposited on the wafer surface in an RF sputtering system, ULVAC SBR-1104. The background pressure of the

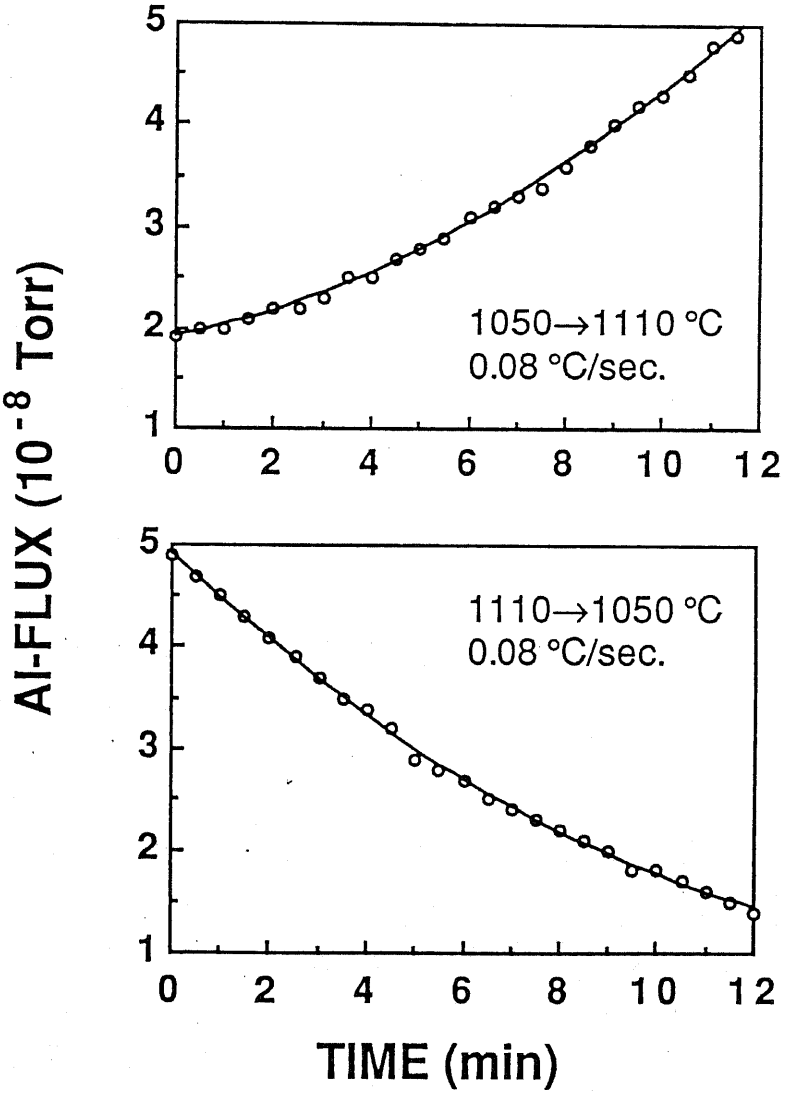

Fig. 4.4 Measured Al-flux variations, for when the temperature of the Al-cell was linearly varied with time for the growth of the graded regions. The energy band profiles of the compositionally graded AlGaAs regions should be of almost the same shape as these Al-flux profiles.

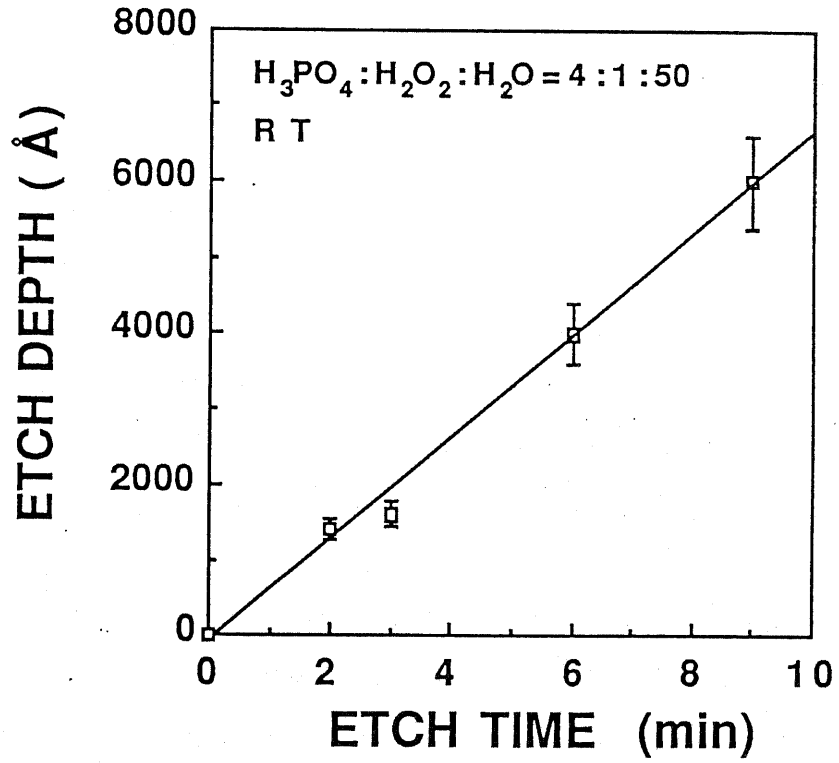

Fig. 4.5 Measured etch-rate of GaAs and AlGaAs (Al < ~ 0.1) for a mixed solution of $H_3PO_4 : H_2O_2 : H_2O = 4 : 1 : 50$ (at least 15 minutes after preparation).

chamber was made less than 3×10^{-6} Torr before the deposition, and during the deposition, the sputtering Ar pressure was kept at 3×10^{-2} Torr.

(5) *Emitter Contact Formation*

Again after degreasing the wafer, windows were first defined in the SiO_2 film for contact evaporations, by patterning the corresponding areas of the emitter and base regions with a negative photoresist (ONNR-22, 35cp). The practical conditions employed with the ONNR-22 photoresist were as follows;

(i) Spin-on at 500 rpm for 5 seconds, followed by 6000 rpm for 30 seconds.

(ii) Prebake in dry air at 95 °C for 30 minutes.

(iii) Exposure under UV mercury lamp for the required time (system-dependent).

(iv) Development in the ONNR Developer for 45 seconds.

(v) Rinse in Rinse-I, then in Rinse-II solutions for 60 seconds each.

(vi) Postbake in dry air at 140 °C for 30 minutes.

Using the photoresist as an etch mask, the SiO_2 film was then etched in a buffered HF for no more than 30 seconds. The photoresist was finally removed in the OMR Stripper at 90 °C for 10 minutes.

The emitter contact region was then patterned using a positive photoresist (OFPR-800, 50 cp) with the following *lift-off* procedure;

(i) Spin-on at 500 rpm for 5 seconds, followed by 4000 rpm for 30 seconds.

(ii) Prebake in dry air at 80 °C for 20 minutes.

(iii) Exposure under UV mercury lamp for the required time (system-dependent).

(iv) Soak and shake *rigorously* in chlorobenzene for 5 minutes and dry with N_2 gas. This hardens the surface of the resist to the development.

(v) Develop in the NMD-3 Developer for 60 seconds.

(vi) Rinse in distilled water for 60 seconds.

(vii) Postbake in dry air at 120 °C for *5 minutes*.

The native oxides of the GaAs wafer surface was then removed by soaking the wafer in pure HCl

for 1 minute, rinsed in distilled water for another 1 minute, and thoroughly dried with N_2 gas, immediately before loading the wafer in a filament evaporation chamber, ULVAC EBH-6. With a background pressure of less than 2.5×10^{-6} Torr, an alloy of Ni/AuGe/Ni/Au (100Å/800Å/400Å/1000Å) was evaporated in sequence in order to accomplish an ohmic metallization to the *n*-type emitter. The contact metal was lifted-off in heated acetone, and the wafer was finally annealed in a flowing N_2 atmosphere at 430 °C for 45 seconds.

(6) *Base Contact Formation*

The same experimental procedure (lift-off technique) was followed for the formation of the *p*-type ohmic contact to the base layer. The alloy used was AuZn/Au (200Å/1000Å), which was annealed at 250 ~ 300 °C for 50 seconds, instead of 430 °C, because of the high diffusivity of Zn in GaAs.

(7) *Collector Contact Formation*

After lapping the wafer on its backside (substrate) down to a thickness of 80 ~ 100 μm, AuGe/Au alloy was evaporated. No annealing was performed. Finally, the device was cleaved down to a length of about 190 μm.

A scanning electron microscope (SEM) photograph of the cross-sectional view of the prepared device is as shown in Fig. 4.6(a). A schematic drawing of the same view is also included in Fig. 4.6(b). The operation principle of the this device is understood as follows; when the free carriers in this case electrons, are injected into the base/waveguide of the transistor, the absorption coefficient in this region changes primarily due to the carrier-induced band-filling effect and plasma dispersion effect, and consequently, the output light intensity can be modulated. Employing a bipolar transistor structure, methods such as fast-rate removal of stored excess carriers by reverse current injection from the base, which are frequently used for electronic switching at high-speeds, can also be applied for optical switching at high-speeds. An amplification nature of the transistor means that large collector currents can be accurately controlled by small input base currents.

4.3 Device Performance

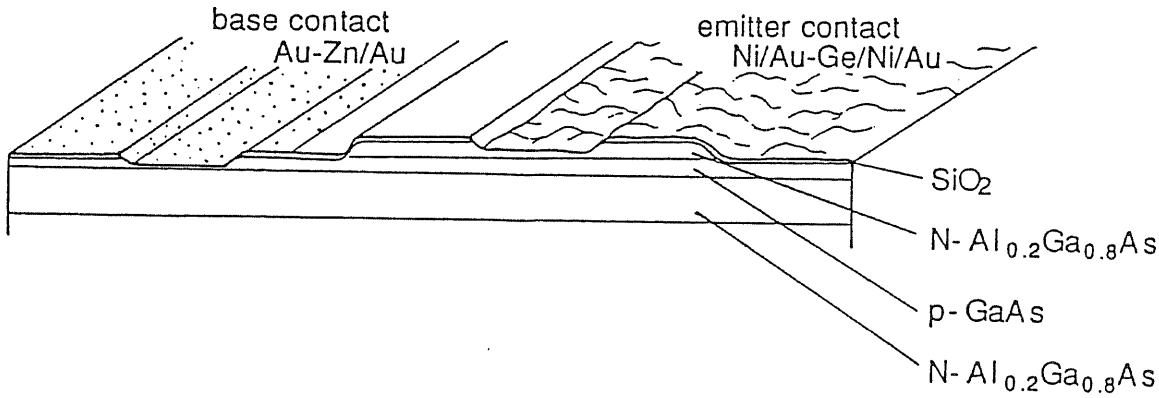

(b)

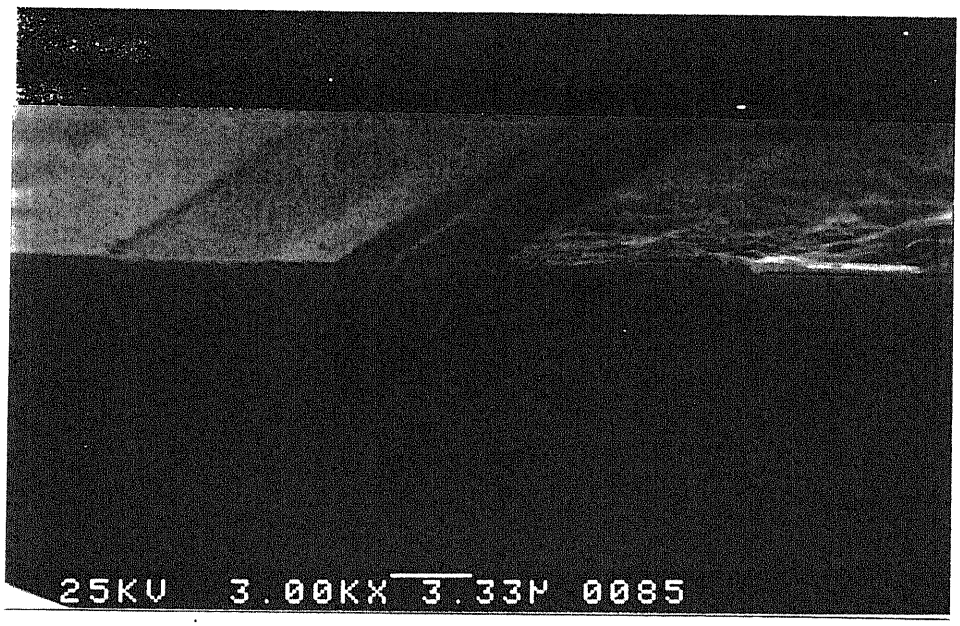

(a)

Fig. 4.6 Cross-sectional view of the prepared device; (a)SEM photograph, and (b)schematic drawing.

4.3.1 Electrical Characteristics

A typical transistor characteristics of the DHBT structure measured in the common-emitter configuration is as shown in Fig. 4.7. Typical current gains h_{FE} obtained were about 38, and some exhibited a maximum h_{FE} of up to about 46. The injection efficiency of the bipolar transistor α_i is essentially a function of the square of the base width w^2,

$$\alpha_i = \alpha_E \, \alpha_T \, \alpha_C \approx \alpha_T = w^2 / 2 D_{nB} \tag{4-1}$$

where α_E is the emitter injection efficiency, α_T is the base transport factor, α_C is the collector collection efficiency, and D_{nB} is the diffusion constant of the minority carriers (electrons) in the base, respectively. And hence, considering that h_{FE} is approximately given by,

$$h_{FE} \approx \alpha_T / (1 - \alpha_T) \tag{4-2}$$

then the present value of h_{FE} for w = 0.25 μm should be acceptable, since w used is < ~ 0.1 μm for the conventional high-gain transistors (h_{FE} > 100) [9]. Furthermore, the results were considerably better than the DHBT waveguide structure also studied with abrupt emitter-base and base-collector heterojunctions, and can be attributed mainly to reduced recombination currents at the graded hetero-interfaces. The dependence of h_{FE} on collector current is also shown in Fig. 4.8. It can be observed that h_{FE} remains constant up to a relatively large collector current of I_c > ~ 80 mA, which is due to an efficient suppression of the flow of backward base current; one of the acclaimed advantages of HBTs [1]. Further improvements in the current gain can be expected by optimizing the growth conditions such as the substrate temperature [10].

For the high-frequency analysis, a very simple transistor equivalent circuit as shown in Fig. 4.9 was considered, and both the values of each circuit component and the expected high-frequency characteristics are tabulated in Table 4-II. In particular, the switching rise time t_r of the transistor was determined by a charge-control analysis [12]. Assuming the common-emitter configuration, t_r was estimated as 1.5 ns. Although t_r was limited by the parasitic impedances, particularly by the emitter contact resistance $R_{ee'}$ (specific contact resistance was no better than $\rho_c \approx 5\times10^{-4}$ Ωcm^2), it has been significantly reduced as compared to the diode-structured devices, whose switching times are typically on the order of several ns. Further technological improvements have to be searched for producing low ohmic contact resistances such as non-alloy ohmic contacts [13], in order to achieve ultra-fast switching speeds as

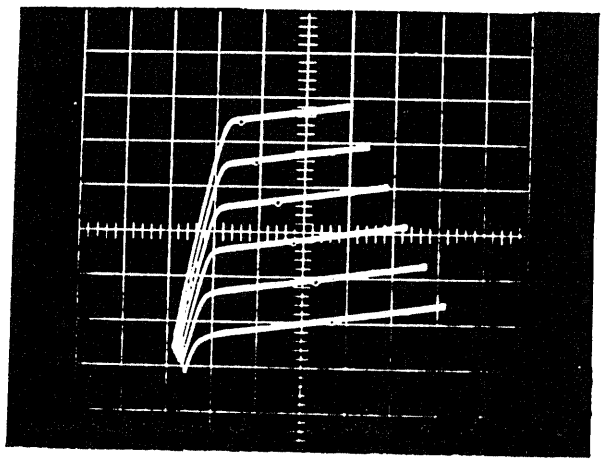

Vertical Axis I_c, 1 mA/div
Horizontal Axis V_{ce}, 1 V/div
Base Current Step, 20 μA

Fig. 4.7 Typical d.c. transistor characteristics measured in the common-emitter configuration.

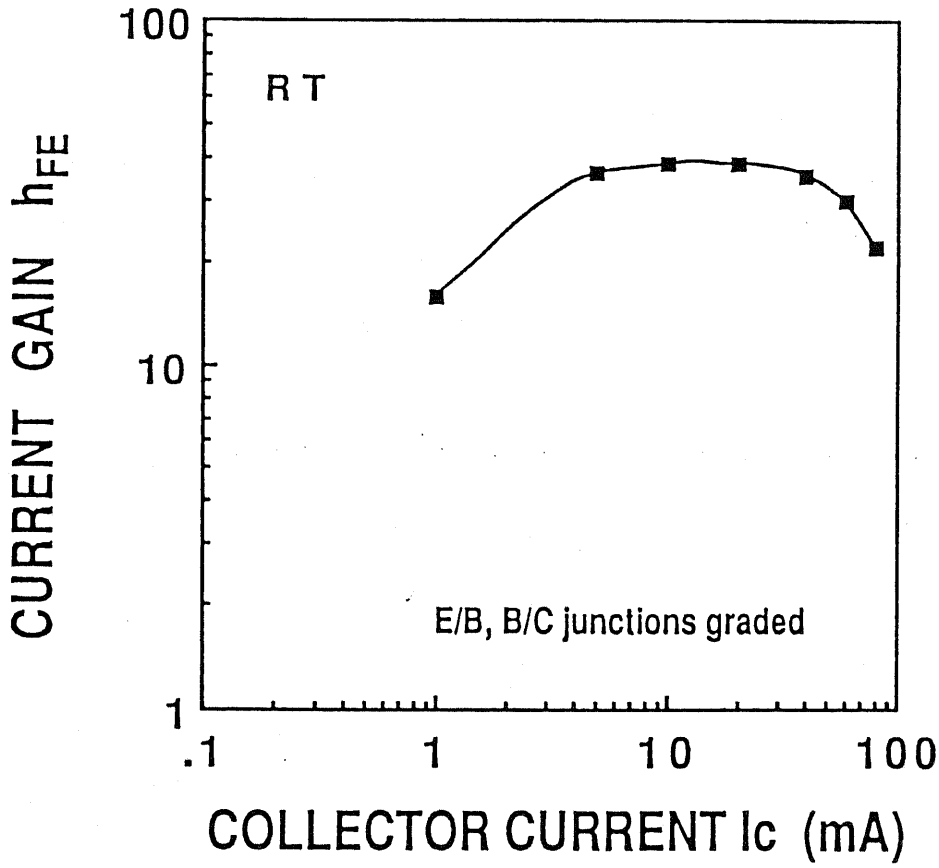

Fig. 4.8 Measured dependence of the current gain h_{FE} on collector current.

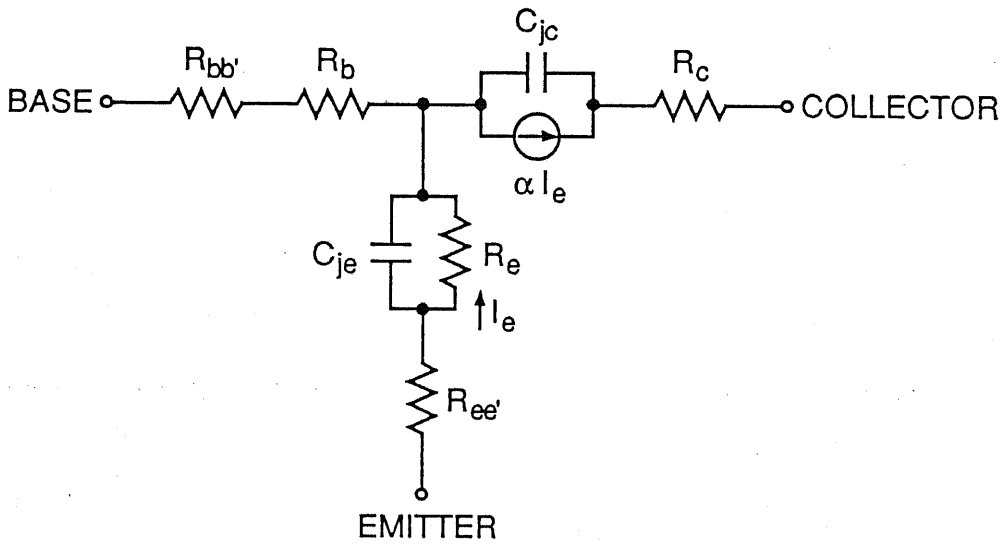

Fig. 4.9 Typical equivalent circuit of the bipolar transistor considered in this work.

Table 4-II Element values of the equivalent circuit model as of Fig. 4.9.

Emitter junction resistance (Ω)	R_e	0.6
Emitter series resistance (Ω)	$R_{ee'}$	40
Base resistance (Ω)	R_b	2.0
Base series resistance (Ω)	$R_{bb'}$	22
Collector resistance (Ω)	R_c	0.1
Load resistance (Ω)	R_L	50
Emitter junction capacitance (pF)	C_{je}	2.3
Collector junction capacitance (pF)	C_{jc}	4.9
Current amplification factor (@I_e = 80 mA)	$\beta\,(h_{FE})$	22
Emitter charging time (ps)	τ_e	1.4
Base transit time (ps)	τ_T	8.9
a) Collector charging time (ps)	τ_c	200
Emitter-collector delay time (ps)	τ_{ec}	210
b) Rise time (common-base) (ns)	t_r	1.0 *
c) Rise time (common-emitter) (ns)	t_r	1.5
d) Intrinsic cutoff frequency (GHz)	f_α	18
e) Maximum oscillation frequency (GHz)	f_{max}	2.5
f) Unity current gain cutoff frequency (GHz)	f_T	0.76

a) $\tau_c = (R_e + R_{ee'} + R_c)\, C_{jc}$

b) $t_r \approx \left(\tau_T + (R_e + R_{ee'} + R_c + R_L)\, C_{jc}\right) \ln 10$

c) $t_r \approx \left(\beta\,\tau_T + (R_e + R_{ee'} + R_c + R_L)\, C_{jc}\right) \ln 10$

d) $f_\alpha = \dfrac{1}{2\pi\,\tau_T}$

e) $f_{max} = \sqrt{\dfrac{f_\alpha}{8\pi\,(R_b + R_{bb'})\, C_{jc}}}$

f) $f_T = \dfrac{1}{2\pi\,\tau_{ec}}$

* N.B.) For the estimate of the switching time of an HBT, the following expression is also frequently used [1],

$$t_r \approx \frac{5}{2}(R_b + R_{bb'})\, C_{jc} + \frac{(R_b + R_{bb'})}{R_L}\,\tau_T + (3C_{jc} + C_L)\, R_L$$

in which case, t_r = 1.0 ns with C_L = 0 pF. The result is therefore the same as the value obtained with the equation b).

is studied in more detail in the next chapter.

4.3.2 Optical Modulation Characteristics

A schematic experimental set-up used for the determination of optical modulation characteristics is as shown in Fig. 4.10. A single TE_0-like mode output from a CW GaAs distributed-feedback (DFB) laser diode (λ = 870 nm) was end-fire coupled into a cleaved end face of the waveguide by a microscope objective (20×, NA 0.40). To permit the observation of the mode structure, the near-field pattern of the output was magnified with another microscope lens (20×, NA 0.40), and then imaged into an infrared vidicon and displayed on a TV monitor. The output power was also monitored using a Si photodiode. The transistor was operated in the common-emitter configuration, and the collector was reverse-biased at 1.5 V. The current was injected into the sample as a pulse train from the pulse generator. Also, the sample has been soldered and fixed on a copper stub (about 0.7 mm wide) with indium.

Figure 4.11 shows the near-field patterns observed at various points along the waveguide plane. The 100-μm wide *dummy* mesa structures prepared in between the actual optical modulator devices, act to ease the manual optical axis alignment as well as to protect the actual modulators from any mechanical damage during the cleaving process. As can be clearly observed from the figure, the near-field pattern of the guided wave through the DHBT structure optical modulator is of a single-mode spot.

Figure 4.12 shows the relative change of the output light intensity measured at different levels of carrier injection. Also shown in Fig. 4.13 is the measured response of the output light intensity to the injected collector current. The spontaneous emission due to current injection was measured to be negligible, which meant that the carrier lifetime in the base/waveguide region was mainly determined by the non-radiative recombination lifetime. It can be observed from Fig. 4.12 that the output light intensity increases almost linearly with injection current, and up to 2.1:1 optical on/off modulation ratio has been obtained at a pulsed base current of as small as $I_b \approx 3$ mA, or equivalently at a collector current of $I_c \approx$ 80 mA as can be observed from Fig. 4.13. Also, the results were considerably better than the DHBT waveguide structure also studied with abrupt emitter-base and base-collector heterojunctions as can be seen from the plot of Fig. 4.14. This is strongly thought to be due to an improved interaction of the down-flow current field and the guided wave in the base/waveguide. And for the beam propagation, the following conventional dependence,

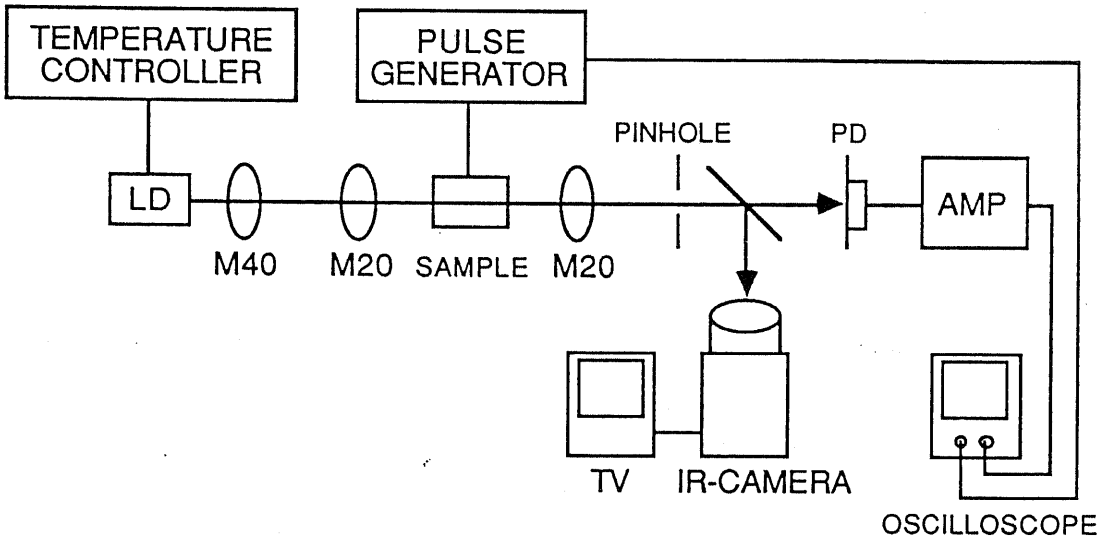

Fig. 4.10 A schematic measurement set-up used for the determination of the optical modulation characteristics. A CW GaAs laser diode (SONY corp.) was used as the input light source ($\lambda = 870$ nm).

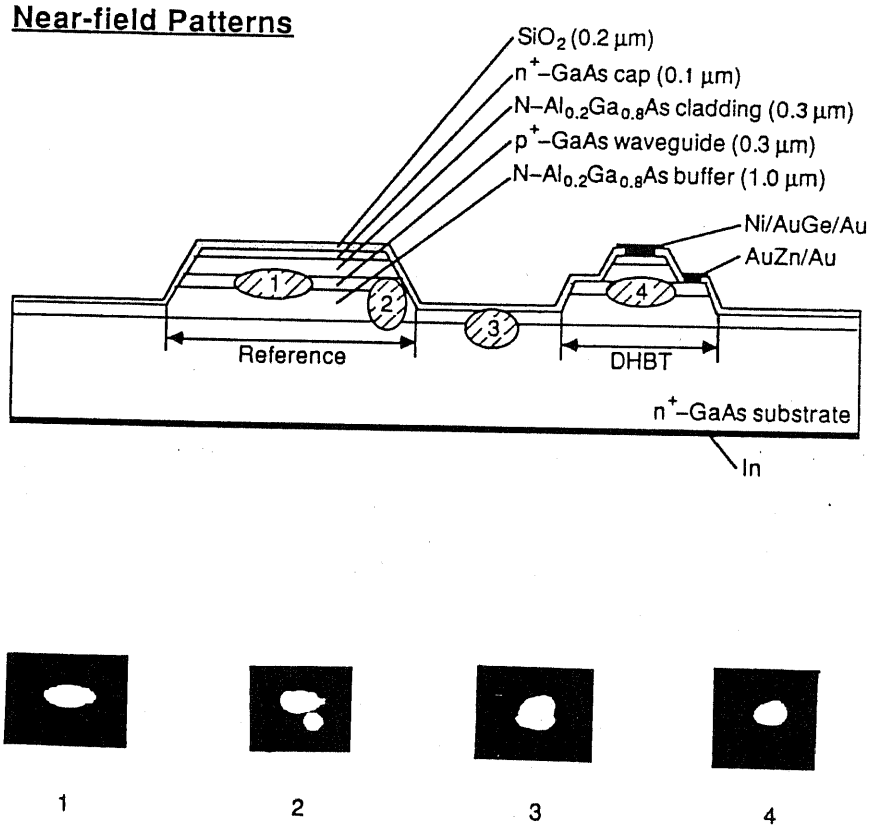

Fig. 4.11 Observed near-field patterns along the waveguide plane. As can be clearly observed, the near-field pattern of the guided wave through the DHBT structure optical modulator is of a single-mode spot.

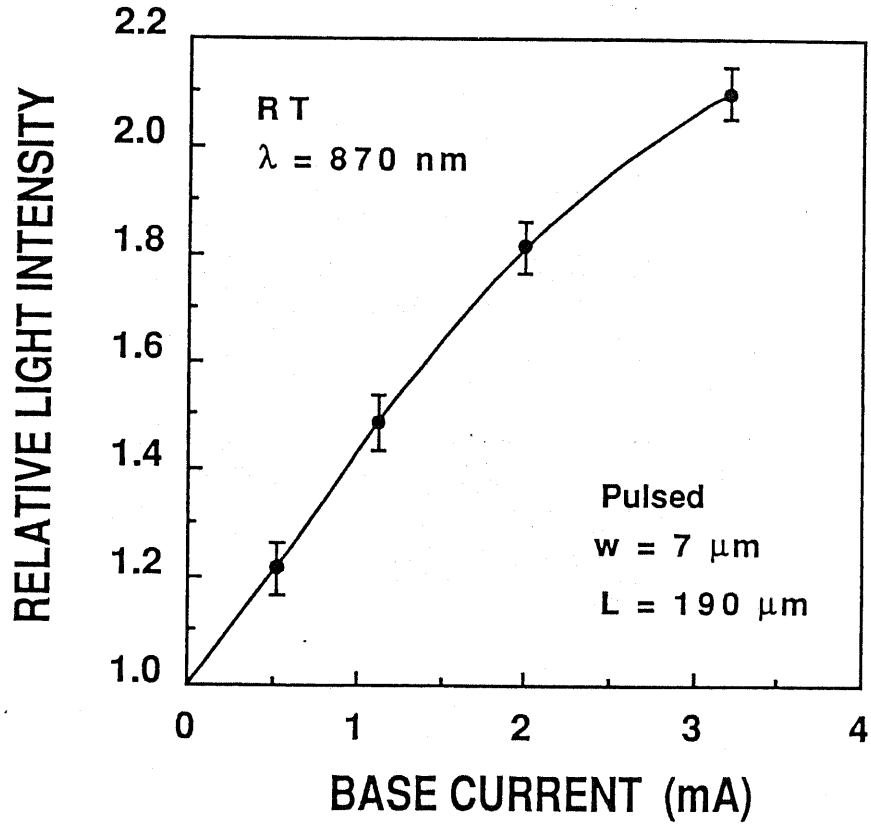

Fig. 4.12 Optical modulation characteristics measured at room temperature. The output light intensity *increases* almost linearly with injection current, mainly due to the band-filling and plasma dispersion effects.

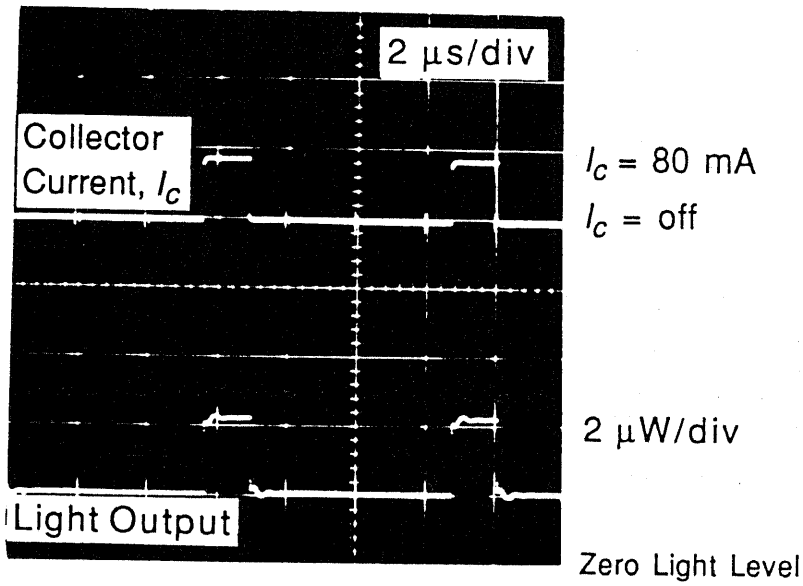

Fig. 4.13 Measured response of the output light intensity to the injected collector current.

$$m = \exp\,[-\,\Delta\alpha\,\Gamma L] \tag{4-3}$$

can be assumed, where m is the on/off ratio of the optical powers after and before the current injection, $\Delta\alpha$ is the current-induced absorption change, Γ is the optical confinement factor of the waveguide, and L is the device length, respectively. Then the absorption change $\Delta\alpha$ obtained would be approximately – 41 cm^{-1} at $I_b \approx 3$ mA for an ideal case of Γ equals unity And in the present device under study, Γ of the waveguide can be assumed to be unity. However, the overlap integral between the optical and current fields is thought to be somewhat smaller than unity because of such factors as large surface recombination losses expected in the external base region. Therefore, the actual $\Delta\alpha$ obtained was believed to be much larger.

The waveguide absorption loss α was also determined using a Fabry-Perot resonance technique [14]. Typical resonance pattern obtained for a sample with 10 μm width and 500 μm length, and the identical device layer structure as of Fig. 4.1 is shown in Fig. 4.15(a). The wavelength dependence was also measured as shown in Fig. 15(b). For this measurement, the laser temperature was slowly changed by about 0.5 °C/min thereby changing the laser wavelength. α can then be determined from the following expression [14],

$$\alpha = -\frac{1}{L}\ln\left(\frac{1}{R}\frac{\sqrt{K}-1}{\sqrt{K}+1}\right) \tag{4-4}$$

where,

$$K = \frac{\text{Power at resonance (maximum)}}{\text{Power at anti-resonance (minimum)}} \tag{4-5}$$

where L is the device length and R is the power reflectivity (R = 0.32 for GaAs), respectively. From Fig. 4.15(a), the value of α was determined to be approximately 46 cm^{-1} (or total waveguide loss of 4.0 dB for 190 μm length) at λ = 870 nm. This meant that the modulation efficiency $\Delta\alpha / \alpha$ was better than 89% at $I_b \approx 3$ mA for the results as shown in Fig. 4.12. Further improvements in the optical modulation efficiency can be expected, if the wavelength of the light source had been optimized to a value near the band-gap, which would result in larger absorption variations as well as small frequency chirping or alpha-parameter, while keeping the absolute absorption losses small. On the basis of our previous calculations (Chapter 3), the theoretical value for such optimum wavelength should lie in the region of be about 885 nm. Furthermore, in Fig. 4.15(b), the absorption data agree fairly well with the calculation

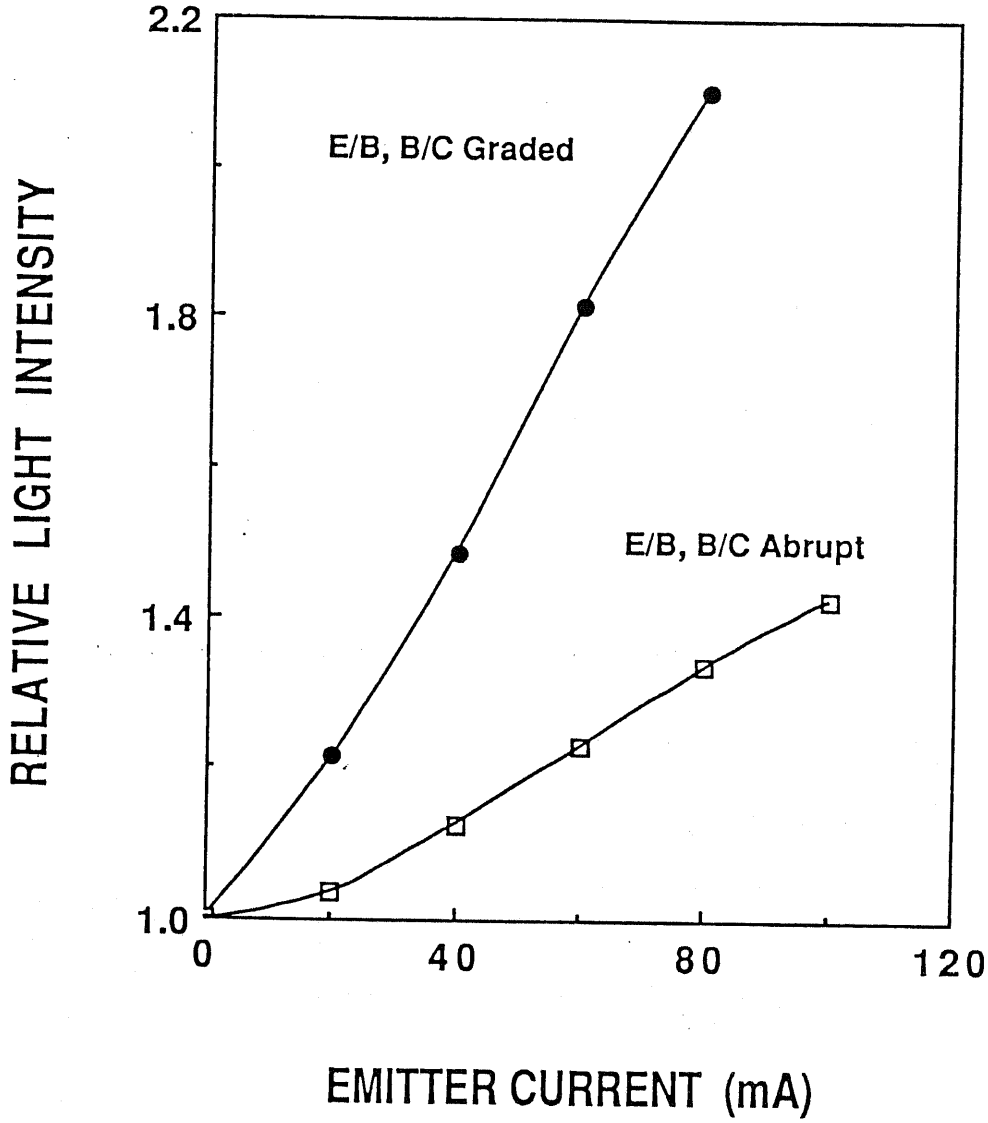

Fig. 4.14 Comparison of optical modulation characteristics for the two different samples; one with *graded* emitter-base and base-collector heterojunctions and the other with *abrupt* heterojunctions.

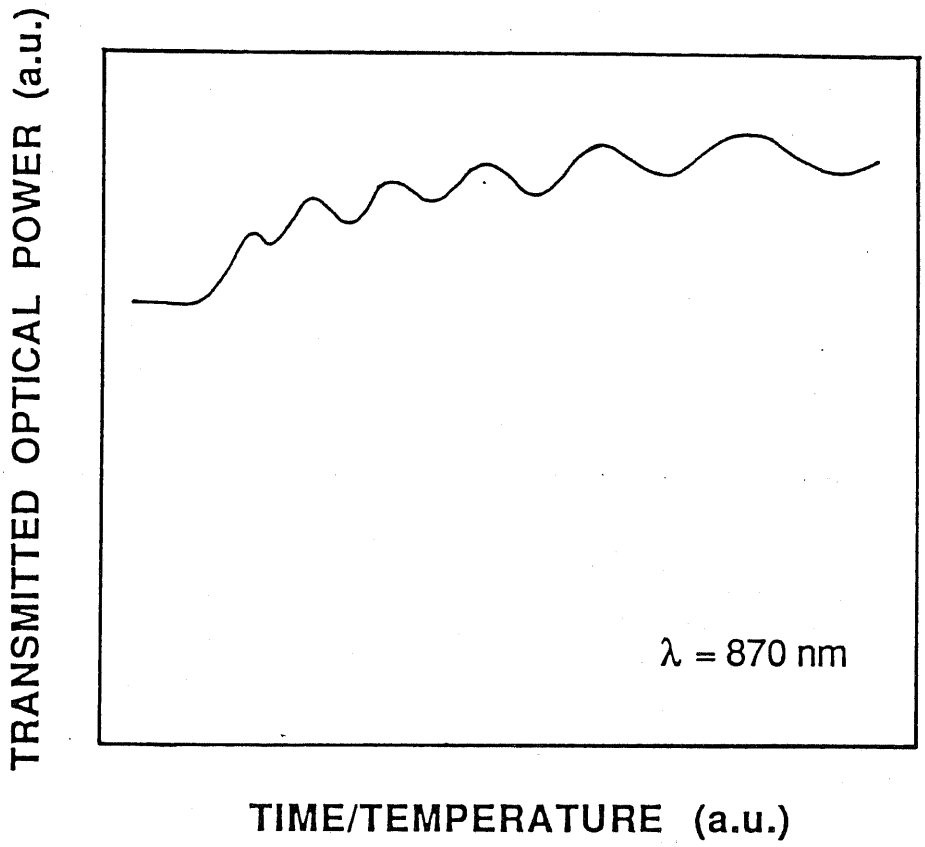

Fig. 4.15(a) Typical Fabry-Perot resonance pattern obtained as the temperature of the laser, and hence the wavelength was varied slowly with time. The waveguide loss of was determined to be approximately 46 cm^{-1} (or total waveguide loss of 4.0 dB) at $\lambda = 870$ nm.

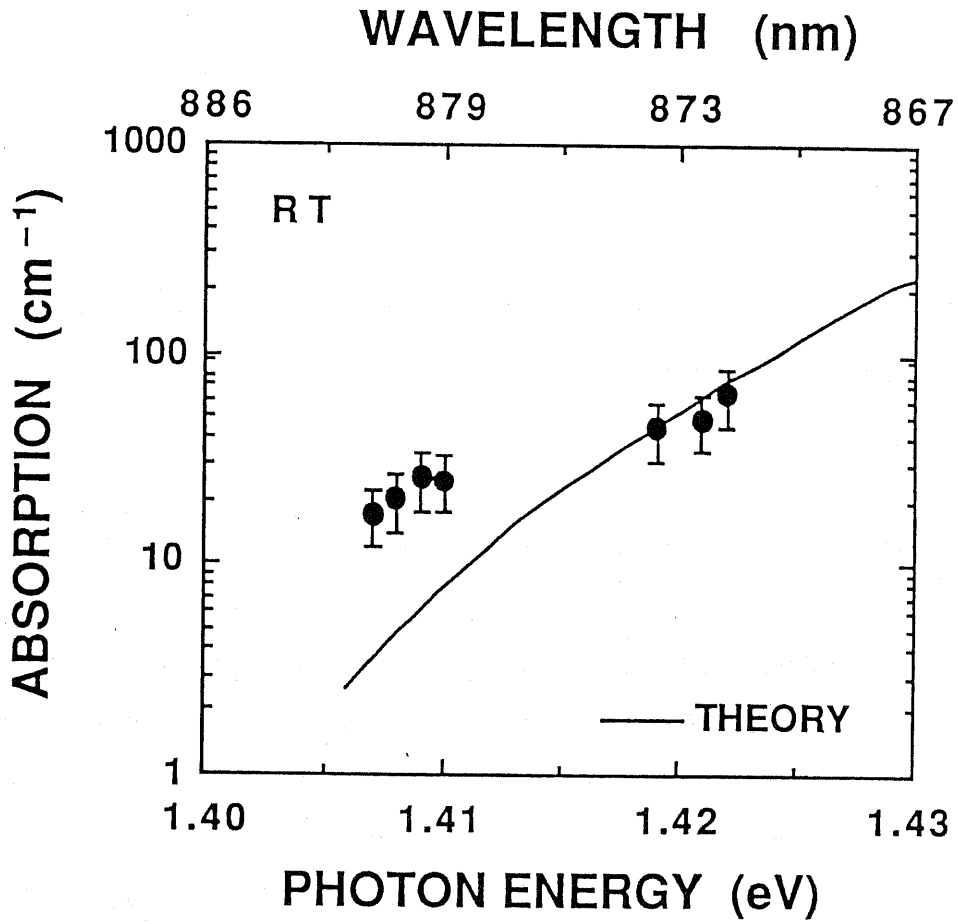

Fig. 4.15(b) Measured wavelength dependence of α as determined using Fabry-Perot resonance technique. Solid-line is the calculation assuming Stern's absorption model.

using Stern's band-tail model for energies in the band-tail region. For much lower energies, the absorption α seems to saturate at around 7 cm^{-1}. Lastly, the total optical loss in the measurement was summarized as follows;

$$\begin{array}{c} \text{Total optical loss} \approx \text{Insertion loss} + \text{Fresnel reflection loss} + \text{Waveguide loss} \\ 23.5\ (\text{dB}) \quad = \quad 16.1 \quad + \quad 3.4 \quad + \quad 4.0 \\ (1.7\ \text{dB/facet at}\ \lambda = 870\ \text{nm}) \end{array} \tag{4-6}$$

A large insertion loss indicates a poor optical coupling efficiency inherent in the end-fire coupling technique, and one simple way of reducing the loss is by coupling the optical power through an optical fiber with a spherically polished end so that the output beam diameter remains < ~ 5 μm.

4.4 Analysis of Reflection-Type Optical Switch Using Bipolar Transistor Waveguide Structure

In this section, experimental data obtained in the last section with the DHBT waveguide structure carrier-injected optical intensity modulator have been applied to design, compute, and analyze the device characteristics expected for a semiconductor reflection-type X-crossing optical switch [15]–[18].

A schematic drawing of the DHBT waveguide structure carrier-injected X-crossing optical switch considered is shown in Fig. 4.16. The layer structure as shown in Fig. 4.16(b) is almost identical to the structure previously studied in the last section, and the 0.25 μm-thick p^+ -GaAs layer doped to 1×10^{18} cm^{-3} functions as the base of an *N-p-N* HBT structure, as well as a single-mode optical waveguide. When the carriers are injected into the base/waveguide of the transistor, the refractive index in this region reduces for a properly selected wavelength, primarily due to the carrier-induced band-filling and plasma dispersion effects, and consequently, the incident light power can be switched from the transmission port L_1 to the opposite reflection port L_2 by total internal reflection.

Let us first summarize the results reported in Sec. 4.2; typical common-emitter d.c. current gain h_{FE} of the HBT measured was 38. Also the estimated transit time τ_T of the diffusing minority carriers (electrons) across the 0.25 μm-thick base was 8.9 ps, and the switching time t_r of the DHBT structure in the common-emitter mode for a 50 Ω load circuit was about 1.5 ns, which had been limited by the parasitic impedance mainly by the emitter contact resistance $R_{ee'}$. Free-carrier injection has modulated the

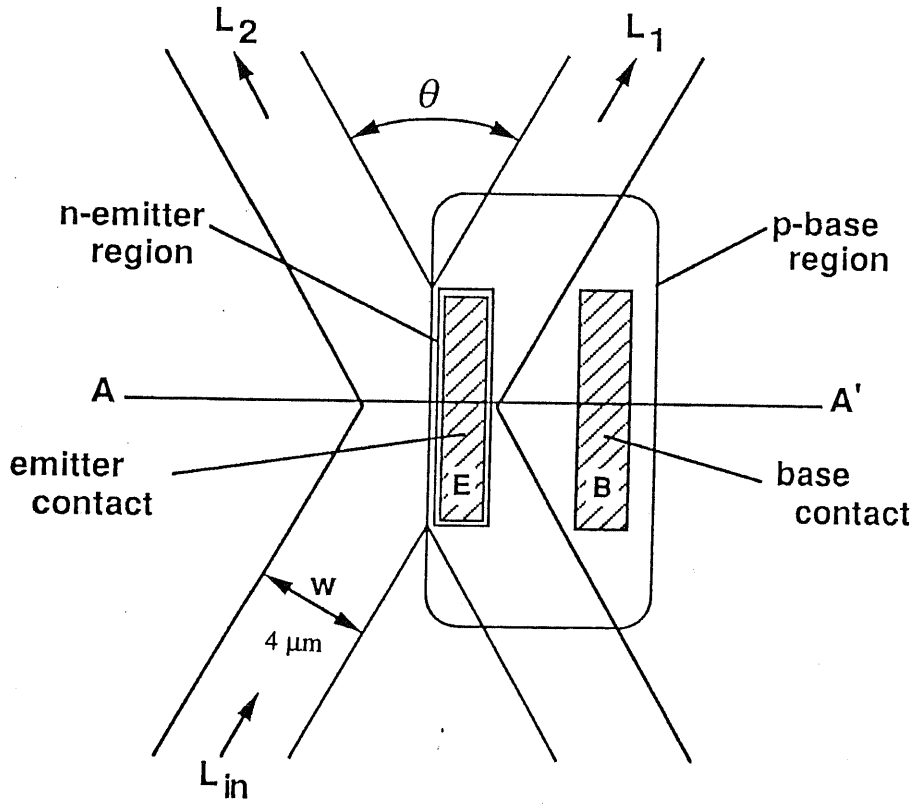

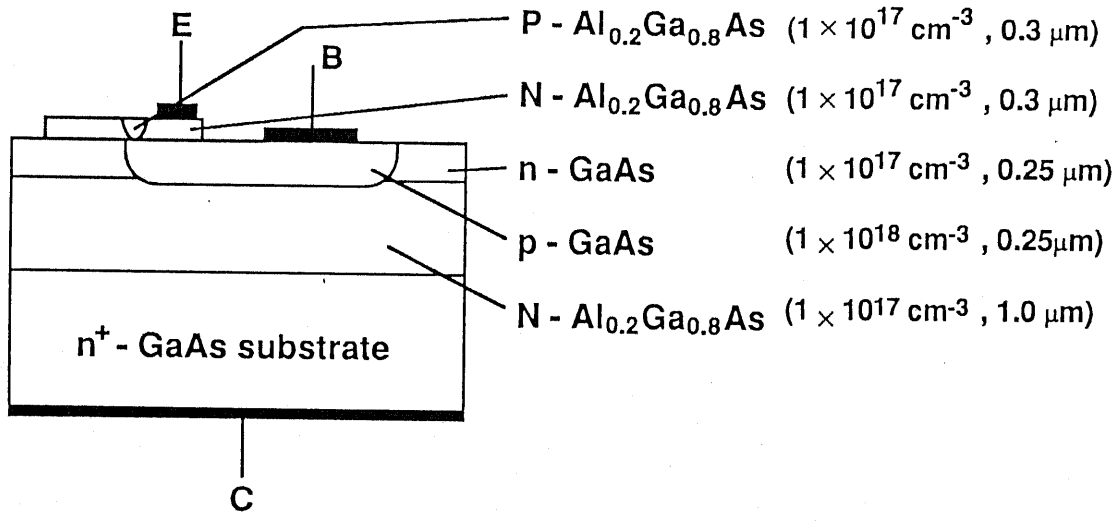

Fig. 4.16 A schematic drawing of the DHBT waveguide structure reflection-type carrier-injected X-crossing optical switch considered for this work; (a) overview, and (b) AA' cross-section.

absorption coefficient α in the waveguide and consequently, optical on/off modulation ratio of up to 2.1:1, corresponding to modulation efficiency of $\Delta\alpha / \alpha \approx 89\%$ have been demonstrated at the injected base current of 3 mA as shown in Fig. 4.12, for a device with waveguide width of 7 μm, length of 190 μm, and at the wavelength of $\lambda = 870$ nm.

Assuming Stern's absorption model for the base/waveguide layer (c.f. Chapter 3), the variation of the real refractive index $\Delta\mu$ with injected current can be determined by taking a Kramers-Kronig transformation of the absorption variation $\Delta\alpha$. The results are shown in Fig. 4.17, and it can be observed from the figure that $\Delta\mu$ varies in relative proportion with $\Delta\alpha$, and $\Delta\mu \approx -0.4 \times 10^{-2}$ at the base current of $I_b = 3$ mA was obtained.

The above results were then used to calculate the optical switching characteristics of the X-crossing optical switch as of Fig. 4.16 by using beam propagation method (BPM). The Fourier transform required for the BPM is accomplished using a standard subroutine in Tokyo University Computer Centre Mathematical Subroutine Library MSL II, as mentioned in Sec. 2.4.1. Also the assumed parameters for the analysis are as follows;

(i) A TE_0-like mode is excited in one of the two input single-mode waveguide arms. The wavelength of the guided mode is assumed to be $\lambda = 870$ nm.

(ii) The total device length is 800 μm. This means that for $\theta = 4°$, the switch length is about 110 μm and the separation of the waveguide arms at the both ends of the device is ~ 30 μm.

(iii) Negative changes in the refractive index are caused in the waveguide/base region as a result of electron injection for the given wavelength. The amount of index variation was estimated using the results as plotted in Fig. 4.17. The least-square fit results in the following relation;

$$\Delta\mu \approx -0.013 \times 10^{-18} \Delta n \tag{4-7}$$

(iv) The transistor is assumed to operate in its active state when fully turned on. This means that the distribution of the injected minority carriers will be at a maximum at the emitter end of the base region, decreasing nearly *linearly* to zero at the collector end, where the carriers are removed by the electric field that is set up across the base-collector reverse biased junction. Since the carrier-induced index variations also vary accordingly with distance in the waveguide/base layer, a fully three dimensional BPM analysis is necessary for an exact treatment of the mode propagation. In order to reduce the problem to a two

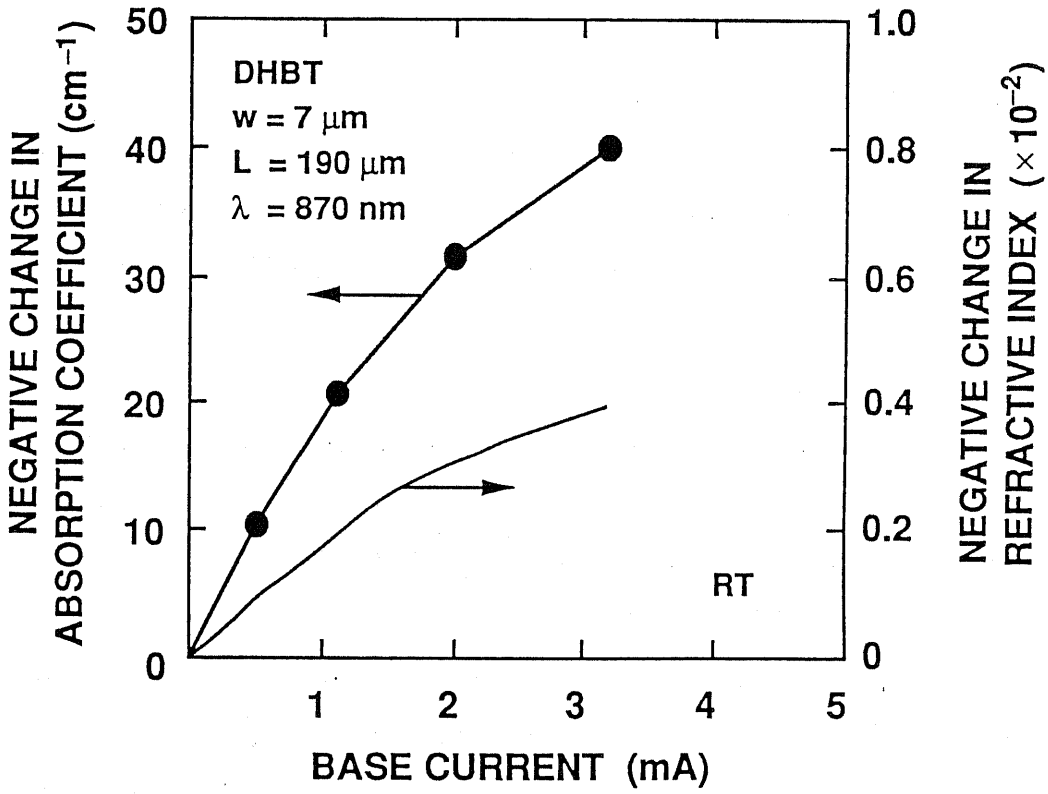

Fig. 4.17 Assuming Stern's absorption model for the base/waveguide layer (c.f. Chapter 3), the variation of the real refractive index $\Delta\mu$ with injected current was determined by taking a Kramers-Kronig transformation of the absorption variation $\Delta\alpha$.

dimensional one without much loss of accuracy and to save the running time of computation, an *average* value of the carrier density and hence the refractive index in the base/waveguide region are considered.

The results obtained for an intersecting angle of $\theta = 4°$ is shown in Fig. 4.18. Typical optical field/power distributions obtained for both the through and crossover states are also shown in Fig. 4.19(a) and (b), respectively. It can be observed from Fig. 4.18 that the amount of the reflected optical power could be controlled by the base current, and an extinction ratio of better than 12 dB could be achieved at I_b = 1.5 mA. The common-emitter mode switching time was estimated as about 0.9 ns, had the parasitic impedance been reduced to a minimum. The results are therefore, very promising for realizing small reflection-type optical switches with high-speeds and high extinction ratios.

4.5 Conclusion

In conclusion, we have presented device fabrication and measurement of optical modulation and electrical characteristics of a GaAs/AlGaAs DHBT single-waveguide structure carrier-injected optical intensity modulator, whose device configuration is particularly suitable for possible monolithic integrated circuits. The device structure is uniquely characterized by an incorporation of graded heterojunctions in order to improve the d.c. transistor characteristics, i.e. the collector-base and emitter-base heterojunctions have graded energy-band configurations in order to prevent the occurrence of "spikes", which would adversely affect the injection and collection of minority carriers. Typical common-emitter d.c. current gain obtained with a 0.25 μm-thick base was about 38 and assuming the common-emitter configuration, the switching time t_r was estimated as 1.5 ns. Although t_r was limited by the parasitic impedances, particularly by the emitter contact resistance $R_{ee'}$ (specific contact resistance was no better than $\rho_c \approx 5\times10^{-4}\ \Omega cm^2$), it has been significantly reduced as compared to the diode-structured devices, whose switching times are typically on the order of several ns. Further technological improvements have to be searched for producing low ohmic contact resistances such as non-alloy ohmic contacts, in order to achieve ultra-fast switching speeds, which will be studied in more detail in Chapter 5.

Optical modulation characteristics was determined using a single TE_0-like mode output from a CW GaAs distributed-feedback (DFB) laser diode (λ = 870 nm) and by an end-fire coupling technique. The output light intensity increased almost linearly with the injection current primarily due to the carrier-

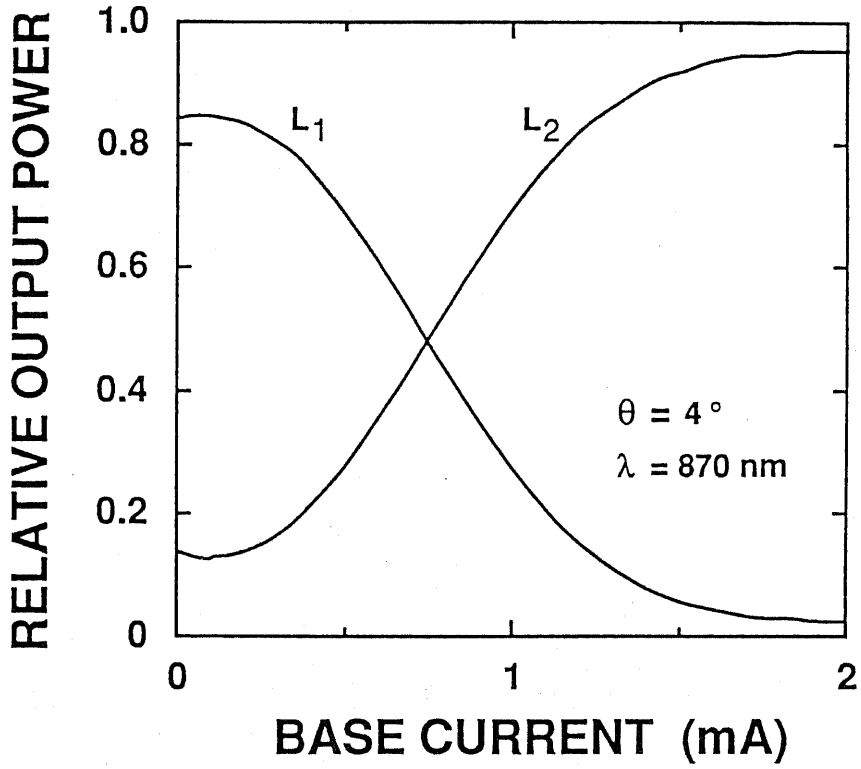

Fig. 4.18 Optical switching characteristics for $\theta = 4^{\circ}$, calculated using the BPM method.

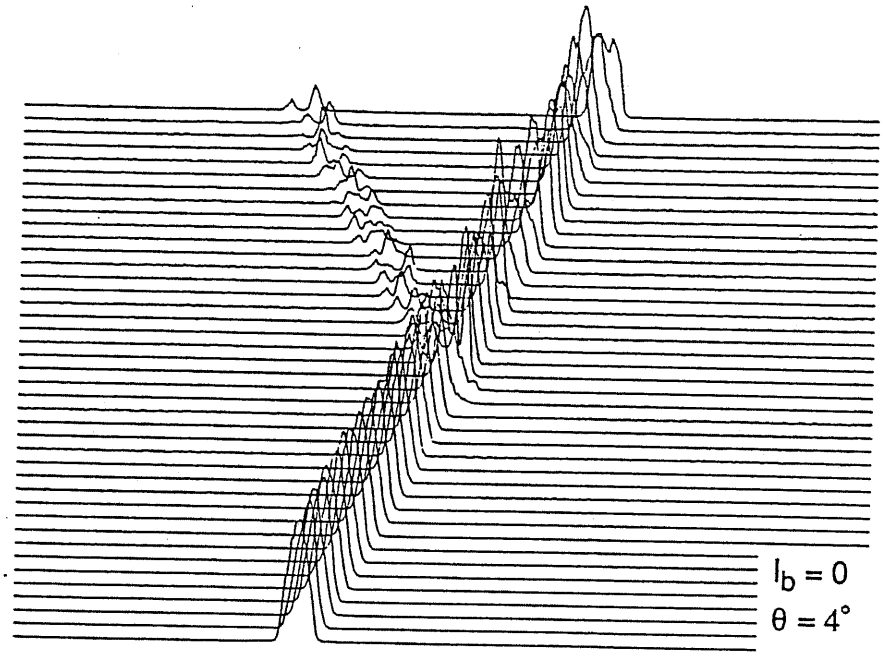

(a)

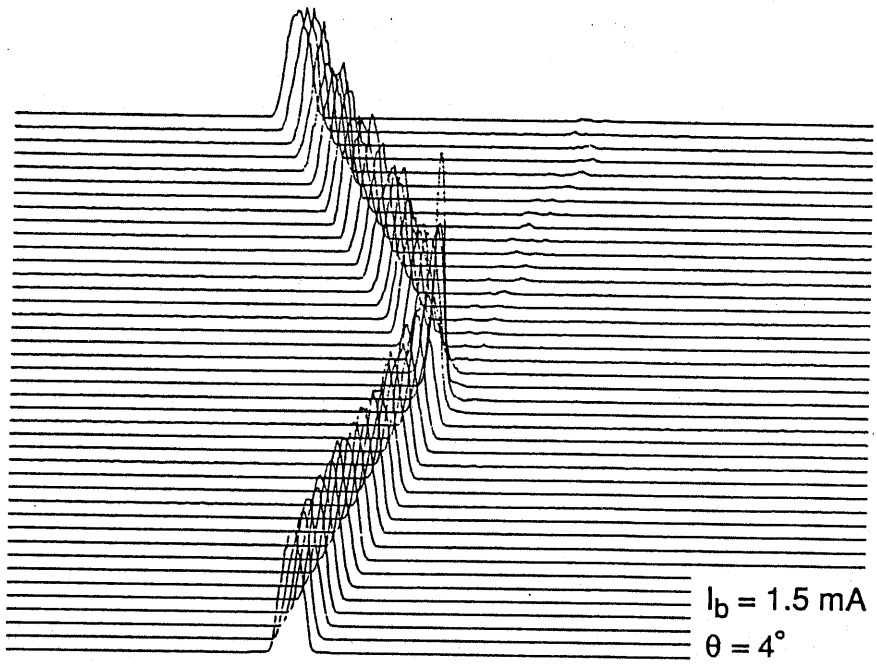

(b)

Fig. 4.19 Calculated optical power distributions obtained for; (a)through state, (b)cross-over state.

induced band-filling effect and plasma dispersion effect, and up to 2.1 : 1 optical on/off intensity modulation or absorption change $\Delta\alpha$ of larger than – 41 cm^{-1} ($\Delta\alpha / \alpha \sim 89\%$) have been demonstrated at a pulsed base current of as small as $I_b \approx 3$ mA or a collector current of $I_c \approx 80$ mA.

Experimental results obtained with this optical intensity modulator have also been applied to design, compute, and analyze the device characteristics expected for a semiconductor reflection-type X-crossing optical switch using beam propagation method. It has been shown that an extinction ratio of better than 12 dB could be obtained at $I_b = 1.5$ mA for a device with an intersecting angle of 4°, and switch length of about 110 μm.

References

[1] H. Kroemer, "Theory of a wide-gap emitter for transistors", *Proc. IRE*, vol. 45, p. 1535, 1957. A recent review by Kroemer describes the potentials of the HBTs in some more detail; "Heterostructure bipolar transistors and integrated circuits", *Proc. IEEE*, vol. 70, p. 13, 1982.

[2] D. K. Jadus and D. L. Feucht, "The realization of a GaAs-Ge wide band gap emitter transistor", *IEEE Trans. Electron Devices*, vol. ED-16, p. 102, 1969.

[3] H. J. Hovel and A. G. Milnes, *IEEE Trans. Electron Devices*, vol. ED-16, p. 766, 1969.

[4] M. Konagai and K. Takahashi, "(GaAl)As-GaAs heterojunction bipolar transistors with high injection efficiency", *J. Appl. Phys.*, vol. 46, p. 2120, 1975.

[5] M. Konagai, K. Katsukawa, and K. Takahashi, "(GaAl)As-GaAs heterojunction phototransistors with high current gain", *J. Appl. Phys.*, vol. 48, p. 4389, 1977.

[6] J. P. Bailbe, A. Marty, P. H. Hiep, and G. E. Rey, "Design and fabrication of high-speed GaAlAs/GaAs heterojunction transistors", *IEEE Trans. Electron Devices*, vol. ED-27, p. 1160, 1980.

[7] H. Beneking and L. M. Su, "GaAlAs/GaAs heterojunction microwave bipolar transistors", *Electron. Lett.*, vol. 17, p. 301, 1981.

[8] D. Ankri, A. Scavennec, C. Bescombes, C. Courbet, F. Heliot, and J. Riou, "High frequency low current GaAlAs/GaAs bipolar transistor", presented at *Dev. Res. Conf.*, Santa Barbara, 1981.

[9] P. M. Asbeck and D. L. Miller, "Recent advances in GaAs/(Ga,Al)As heterojunction bipolar transistors", *Extended Abstracts of the 16th (International) Conference on Solid State Devices and Materials*, Kobe, p. 343, 1984.

[10] S. L. Su, R. Fischer, W. G. Lyons, O. Tejayadi, D. Arnold, J. Klem, and H. Morkoç, "Double

heterojunction GaAs/$Al_xGa_{1-x}As$ bipolar transistors prepared by molecular beam epitaxy", *J. Appl. Phys.*, vol. 54, p. 6725, 1983.

[11] T. Ishikawa, Y. C. Chan, Y. Nakano, and K. Tada, "Application of Modern Control Theory to Temperature Control of MBE System", *Technical Digest of the 1st International Meeting on Advanced Processing and Characterization Technologies*, Tokyo, p. 17, 1989.

[12] K. Tada, T. Sugano, and H. Yanai, *J. IEE Jpn.*, vol. 82, p. 982, 1962.

[13] M A. Rao, E. J. Caine, S. I. Long, and H. Kroemer, "An (Al,Ga) As Heterostructure Bipolar Transistor with Nonalloyed Graded-Gap Ohmic Contacts to the Base and Emitter", *IEEE Electron Device Lett.*, vol. EDL-8, p. 30, 1987.

[14] R. G. Walker, "Simple and Accurate Loss Measurement Technique for Semiconductor Optical Waveguides", *Electron. Lett.*, vol. 21, p. 581, 1985.

[15] O. Mikami and H. Nakagome, "InGaAsP/InP optical waveguide switch operated by a carrier-induced change in the refractive index", *Opt. Quantum Electron.*, vol. 17, p. 449, 1985.

[16] K. Ishida, H. Nakamura, H. Matsumura, T. Kadoi, and H. Inoue, "InGaAsP/InP optical switches using carrier induced refractive index change", *Appl. Phys. Lett.*, vol. 50, p. 141, 1987.

[17] T. Kikugawa, K. G. Ravikumar, K. Shimomura, A. Izumi, K. Matsubara, Y. Miyamoto, S. Arai, and Y. Suematsu, "Switching Operation in OMVPE Grown GaInAs/InP MQW Intersectional Optical Switches", *IEEE Photonics Tech. Lett.*, vol. 1, p. 126, 1989.

[18] T. C. Huang, T. Hausken, K. Lee, N. Dagli, L. A. Coldren, and D. R. Myers, "Depletion Edge Translation Waveguide Crossing Optical Switch", *IEEE Photonics Tech. Lett.*, vol. 1, p. 168, 1989.

CHAPTER 5

LOW-RESISTANCE NON-ALLOYED GRADED-GAP OHMIC CONTACT TO *n*-TYPE GaAs

5.1 Introduction

Reduction of parasitic impedance is a fundamental requirement in order to improve the high-speed performance of both the electronic and the optical devices, which have been designed to operate at microwave or even higher frequencies. Inevitably, if the intrinsic switching speed of a given device is very high such as in the case for GaAs and other semiconductor devices, the reduction of the parasitic series resistance is indispensable for suppressing the overall extrinsic delay time. Moreover, it is also evident that low-resistance ohmic contact capability to fine patterns is highly desirable for device scale-down, and hence for possible high-density integrations.

The lack of reproducible and reliable ohmic contacts to moderately-doped *n*-type GaAs, however, has been a persistent problem in metal-semiconductor technology, and should not be overlooked by all means. A simple and therefore widely used technique today to overcome this problem is to alloy suitable evaporated metal layers such as Ni/AuGe [1] to a clean *n*-GaAs surface to obtain a low-resistance ohmic contact. But it has been found that these alloyed ohmic contacts, in practice, suffer from a number of undesirable disadvantages. Firstly, the specific contact (sheet) resistance ρ_c which with today's technology is at best on the order of $\rho_c \approx 10^{-5}$–10^{-6} Ωcm^2 [2], is not low enough for possible application to small-size devices. For example, $\rho_c = 10^{-5}$ Ωcm^2 would correspond to a series resistance of about 10 Ω to a 10×10 μm^2 contact area, which is still considerably large. In Chapter 4, ρ_c measured for a Ni/AuGe/*n*-GaAs contact in the HBT fabrication was limited to about $\rho_c \approx 3$–5×10^{-4} Ωcm^2, which unfortunately was an order of magnitude worse than the best values reported elsewhere. This high contact resistance has been shown to be the major factor that limited the switching speed of the HBT waveguide structure carrier-injected optical modulator/switch under study. Secondly, the fine-pattern capability is poor due to the surface roughness or non-uniformity known as the "ball-up" [3], which is caused during the annealing/alloying cycle. And lastly, the reproducibility and thermal stability of the alloyed contacts are also not sufficient. In fact, the specific contact resistance is very sensitive to the annealing history of

contact. For example, the resistivity of a typical Ni/AuGe/*n*-GaAs contact remains very high for short alloy times at temperatures higher than the AuGe eutectic temperature of 360 °C, then drops sharply to very low values for somewhat longer alloy times (typically on the order of minutes), and then rises rapidly with alloying for even longer anneals [2]. A similar feature has also been reported on the temperature dependence of ρ_c as shown in Fig. 5.1 [3]. Therefore, a critical control of the alloy process is evidently required to obtain reliable and reproducible ohmic contacts.

If one seeks to improve the thermal stability, reproducibility, reliability as well as contact resistivity, then one promising method is to develop "non-alloyed" ohmic contacts, the concept of which has gained much interest recently. There are basically two ways of obtaining low-resistance non-alloyed ohmic contacts to *n*-GaAs. One is to make the Schottky barrier that inherently exists at the metal-semiconductor interface, thin by heavily doping the GaAs contact layer thereby enhancing the tunneling probability. Although specific contact resistances as low as 1×10^{-6} Ωcm^2 have been obtained by heavily doping GaAs with Si [4] or Sn [5], it is difficult to achieve lower values because of the solubility limit of these dopants in GaAs during the growth.

The other way is to utilize a semiconductor having a low Schottky barrier height sandwiched between the *n*-GaAs and the contact metal. Stall *et al.* have demonstrated a specific contact resistance below 1×10^{-7} Ωcm^2 using an n^+-Ge layer [6], which was nearly lattice-matched to GaAs. However, their method still resulted in residual barriers present at the GaAs/Ge and Ge/metal interfaces. Murakami and Price have recently reported an In-based contact to *n*-GaAs [7]. Their technique attempts to form an (In, Ga)As layer on the top thin layer of an *n*-GaAs cap layer by heat treatment, in order to reduce the Schottky barrier height. It has been reported that this contact was thermally stable during an anneal at 500 °C for 10 hours, but the specific contact resistance was limited to about 1×10^{-6} Ωcm^2.

In 1981, Woodall *et al.* [8] proposed and demonstrated a non-alloyed graded-gap scheme for obtaining ohmic contacts to *n*-GaAs by first growing a graded transition from GaAs to InAs, and then making a non-alloyed metallic contact to the InAs. The underlying idea was as follows; it is well known that at an InAs/metal interface, the Fermi level is "pinned" inside the InAs conduction band [9], hence this interface by itself acts as an ideal negative-barrier ohmic contact. However, if the GaAs-to-InAs transition was not graded, it would act as a quasi-Schottky barrier with a barrier height close to the conduction-band offset ΔE_c of the GaAs/InAs heterojunction of about 0.9 eV [10], and hence the contact would be poor overall. Sufficient grading flattens out the heterojunction barrier and leads to an excellent ohmic contact. A very low specific contact resistance of 2×10^{-9} Ωcm^2 has also been predicted with this structure [11],

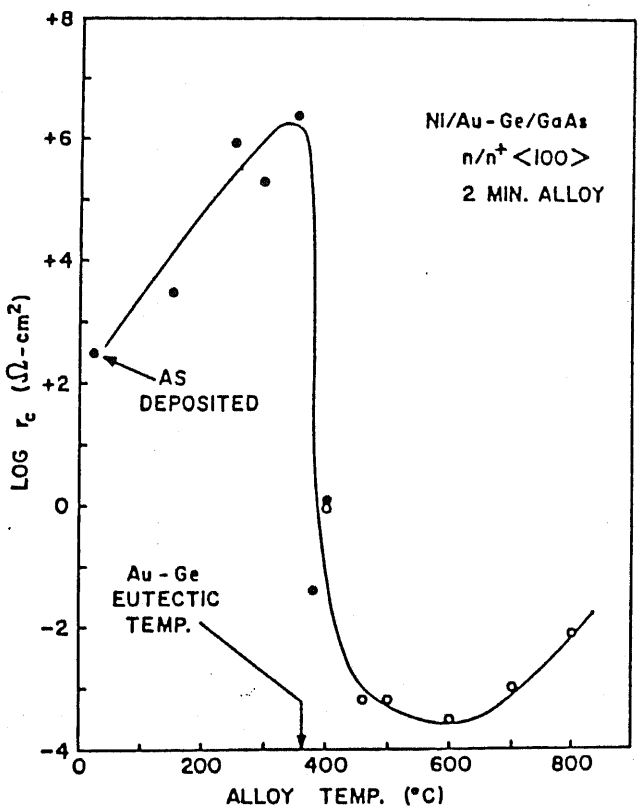

Fig. 5.1 Typical specific contact resistance as a function of alloy temperature for Ni/AuGe on epitaxial *n*-GaAs. (After reference [3])

and $\rho_c = 5\times10^{-9}$ Ωcm^2 has been successfully demonstrated with a 2×10^{19} cm^3 Si-doped structure grown at 450 °C by T. Nittono *et al.* [12].

In this chapter, the MBE growth conditions for an InAs/$In_xGa_{1-x}As$($x = 1\rightarrow0$)/GaAs structure to achieve a low ohmic contact resistance have been investigated with regard to the electrical properties of the grown layers and specific contact resistance. The results are directly applicable to reduce the emitter contact resistance of the *n-p-n* HBT waveguide structure optical modulator/switch under study, and hence the modulation/switching speeds of the device.

5.2 Theory of Graded Band-Gap $In_xGa_{1-x}As$ Ohmic Contact to *n*-GaAs

The metal/*n*-GaAs contact can be represented by the energy diagram of Fig. 5.2(a) [8]. It has been found experimentally for *n*-GaAs that the Schottky barrier height ϕ_b *cannot* be represented by the classical Schottky relationship,

$$\phi_b = \phi_m - \chi_{sc} \tag{5-1}$$

where ϕ_b is the barrier height to *n*-GaAs, ϕ_m is the metal work function, and χ_{sc} is the electron affinity for the semiconductor, respectively. But instead, ϕ_b seems to be almost independent of ϕ_m and has a fixed value of about 0.7–0.9 eV regardless of the type of metal used [9]. This effect has generally been ascribed to the Fermi level "pinning" at the surface or interface due to a large density of mid-gap states either at the surface or interface. More recently, these states have been postulated to be associated with defects at the surface/interface region, which occur as a result of either oxygen adsorption or metal deposition. Whatever the reason may be, the Fermi level pinning causes a rectifying current-voltage (I-V) characteristics for metal contacts to *n*-GaAs. For $n \leq 10^{18}$ cm^{-3}, the result is useful as Schottky diodes, and for higher doping levels an ohmic tunneling behavior should result. However, the specific contact resistance of such ohmic contact [13] can be excessively large for some high-speed applications.

Surface states do not always cause mid-gap Fermi level pinning. For example, at a metal/InAs interface, the Fermi level is "pinned" inside the InAs conduction band [9]. Thus, the situation for the metal/*n*-InAs contact shown in Fig. 5.2(b) would produce an ideal negative-resistance ohmic contact ($\phi_b \leq 0$). In this case, the tunneling is not a required process and low-resistance ohmic contacts can be realized for a wide range of *n*-type doping without the need of alloying to form the n^+-surface layers. With these

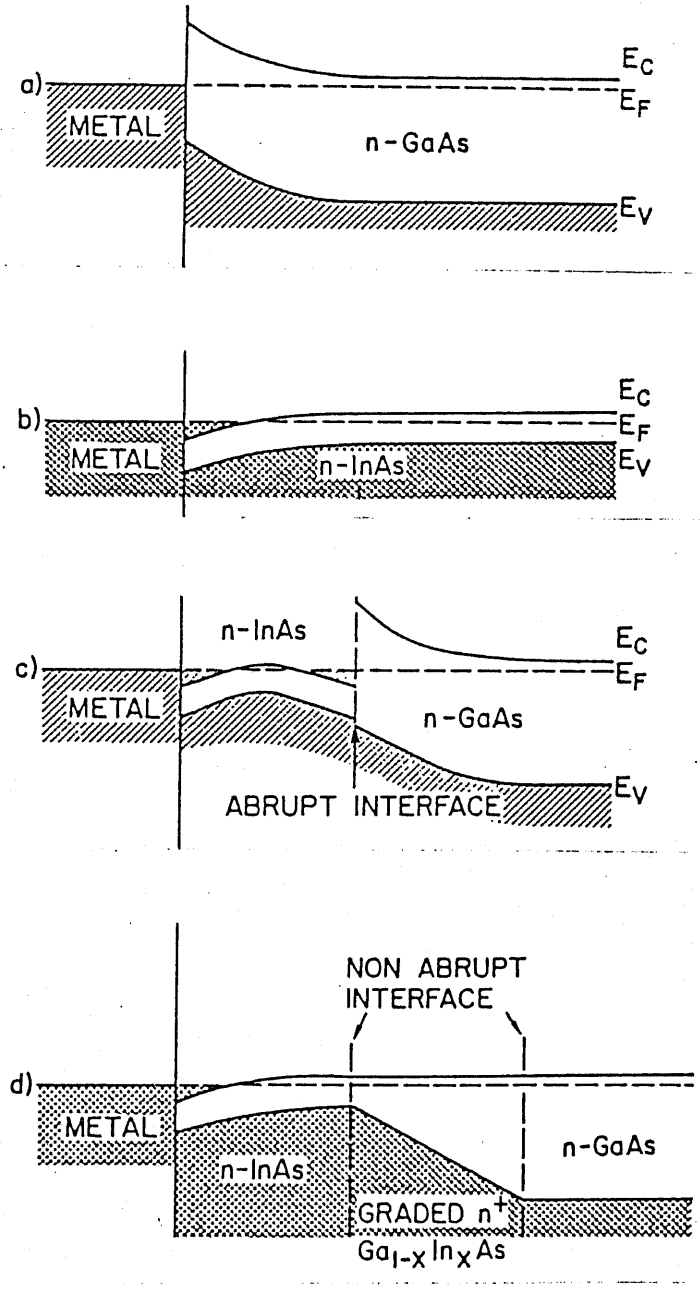

Fig. 5.2 Band-bending diagram for various semiconductor interfaces; (a) metal on *n*-GaAs, (b) metal on *n*-InAs, (c) metal on *n*-InAs on *n*-GaAs, and (d) metal on *n*-InAs on *n*-$In_xGa_{1-x}As$ on *n*-GaAs. (After reference [8])

in mind, one might conclude that good ohmic contacts for GaAs would result if a metal/*n*-InAs/*n*-GaAs combination were used. However, the situation is not quite as simple and the reason for this can be drawn from Fig. 5.2(c). For this structure, there is a positive ϕ_b between the *n*-InAs and *n*-GaAs, which depending on the doping levels, results in either rectifying or ohmic behavior. This quasi-Schottky barrier is due to one or more of the following factors; (i) a large electron affinity discontinuity across the hetero-interface, (b) a large lattice constant discontinuity of about 7 %, and (c) a "dirty" GaAs surface prior to the epitaxial growth. The main effect of the latter two will be the formation of a large number of mid-gap interface states and hence, the Fermi level will be pinned at the mid-gap position. Thus, the *n*-InAs/*n*-GaAs abrupt heterojunction behaves like the metal/*n*-GaAs contact as of Fig. 5.2(a) with a barrier height close to the conduction-band offset ΔE_c of the GaAs/InAs heterojunction of about 0.9 eV [10]. A solution to this problem is as shown in Fig. 5.2(d). For this case, the abrupt *n*-InAs/*n*-GaAs heterojunction is replaced by a layer of graded $In_xGa_{1-x}As$ with varying In composition from $x = 0$ at the GaAs interface to $x = 1$ at the InAs interface. It should be noted that there are no abrupt discontinuities in the conduction band following this approach, and that $\phi_b \leq 0$ for the metal/*n*-InAs contact. Therefore, this system is expected to produce a *non-alloyed low-resistance* ohmic contact. On the other hand, the Ga(As,Sb) system could be similarly used for forming a non-alloyed ohmic contact to *p*-type GaAs, as proposed by Chang and Freeouf [14].

5.3 Graded-Gap Ohmic Contact Growth by Molecular Beam Epitaxy

As a preliminary to the contact growth, the usual relationships of; (a) In-flux versus In-cell temperature, and (b) InAs growth rate versus In-flux were first investigated for our molecular beam epitaxy (MBE) system [15]. The results are shown in Fig. 5.3(a) and (b), respectively. These data have been taken under a fixed *measured* Ga-flux of 2×10^{-7} and As-flux of 1×10^{-5}, or an As/Ga *flux* ratio of about 3 : 1, which resulted in a GaAs growth rate of about 1.8Å/s at the substrate temperature of about T_{sub} = 550 °C.

Based on these results, an *n*-type graded-gap ohmic contact structure was grown by MBE on an (100) p^+-GaAs substrate (Zn-doped to $3\text{–}4\times10^{19}$ cm^{-3}), the layer structure of which is schematically drawn in Fig. 5.4. In order to keep the series path resistance of the graded region low, the doping level in this graded region should be as high as possible and the thickness of the graded region should be as thin as possible, limited only by the requirement to flatten the quasi-Schottky barrier mentioned in the last

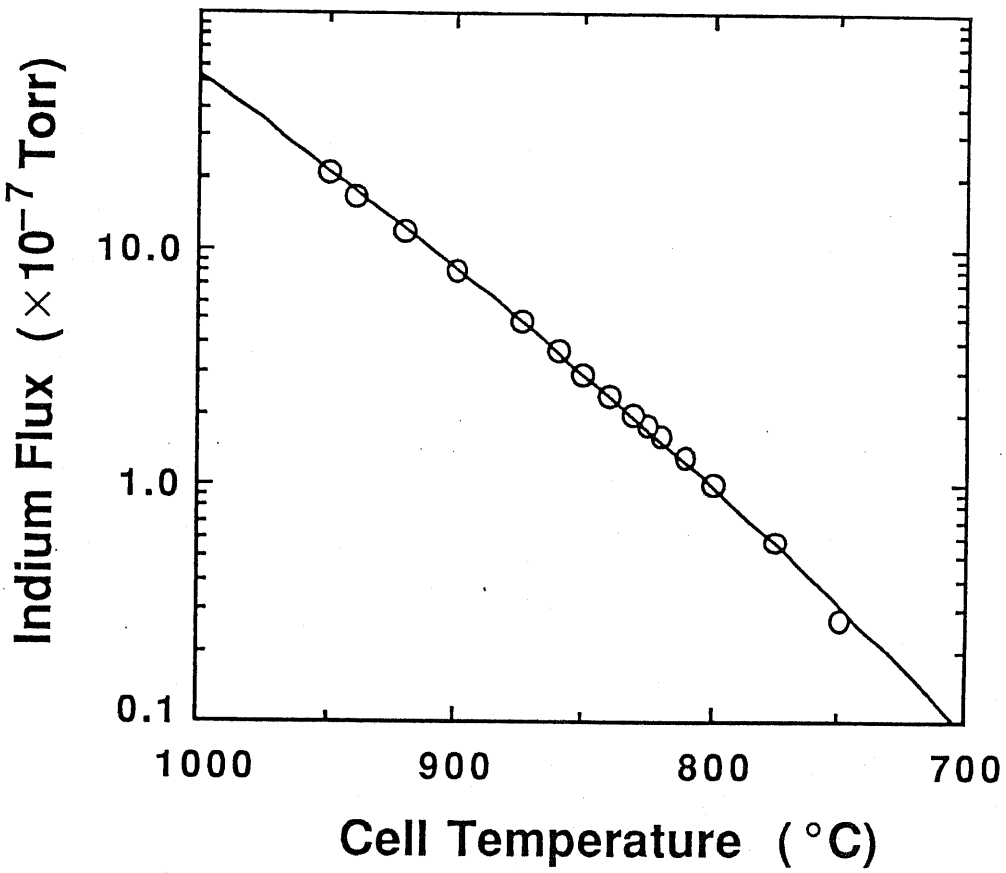

(a)

Fig. 5.3 Measured relationships obtained for our MBE; (a) In-flux versus In-cell temperature, and (b) InAs growth rate versus In-flux.

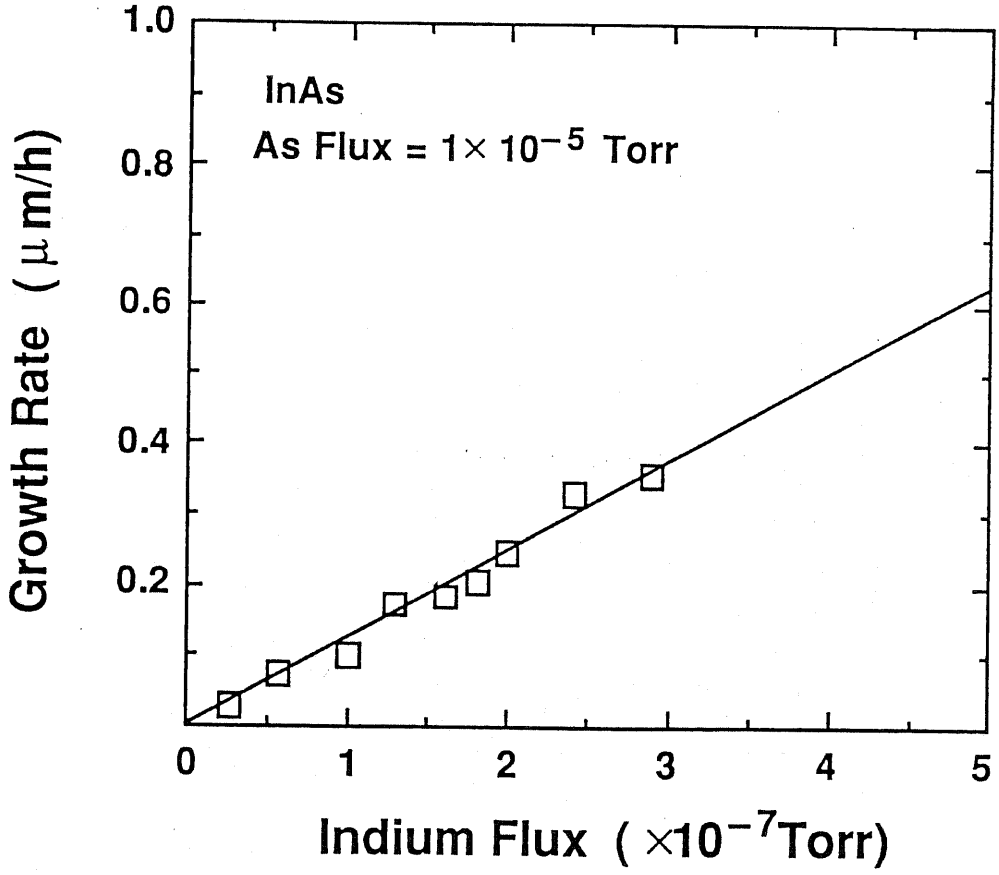

(b)

Fig. 5.3 Measured relationships obtained for our MBE; (a) In-flux versus In-cell temperature, and (b) InAs growth rate versus In-flux.

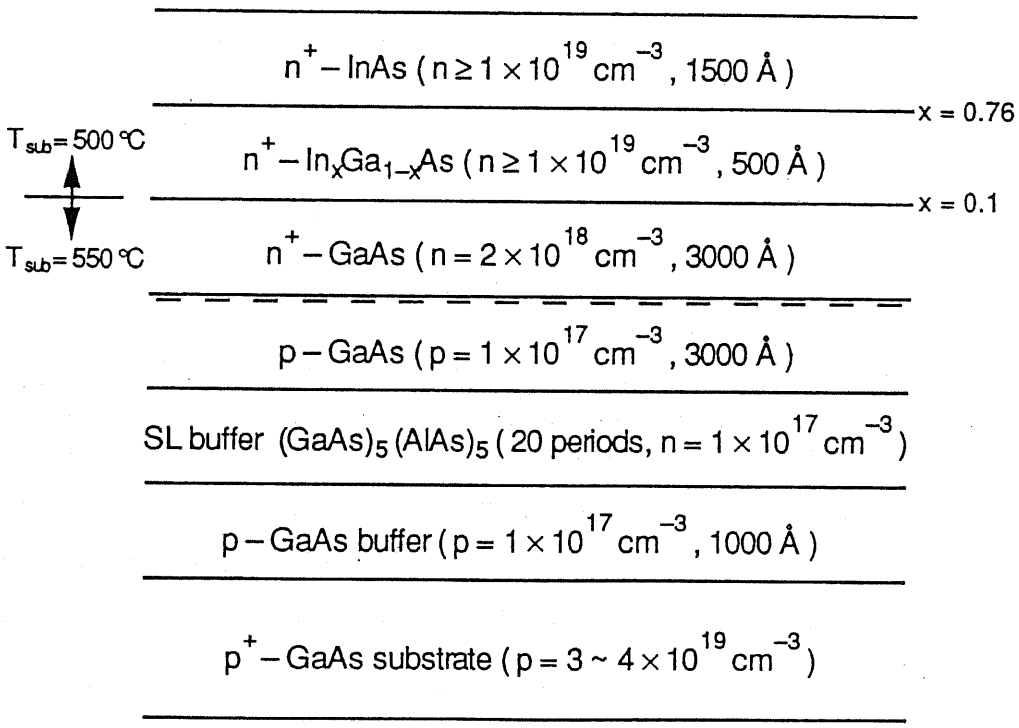

Fig. 5.4 A set of layer parameters grown by MBE for realizing a graded-gap non-alloy ohmic contact.

section. It has been theoretically investigated [16] that the graded regions as thin as 300 Å should be permissible to satisfy the requirement of energy-band flattening. Here, the thickness of the graded region was chosen to be 500 Å.

A *p*-GaAs buffer layer (Si-doped to 1×10^{17} cm^{-3}, 1000 Å) was first grown directly on the substrate. This buffer layer was used to equilibrate the growth and to reduce the effects of the relatively poor substrate-epilayer interface on the more critical *pn*-junction diode layers. Then a 500 Å-thick $(AlAs)_5$ / $(GaAs)_5$ 20-period superlattice structure was grown. It was followed by a *p*-GaAs layer (Be-doped to 1×10^{17} cm^{-3}, 3000 Å), an n^+-GaAs junction layer (Si-doped to 2×10^{18} cm^{-3}, 3000 Å), then by a 500 Å of n^+-(In,Ga)As layer (Si-doped to $\geq 1\times10^{19}$ cm^{-3}) compositionally graded from GaAs to InAs. Finally, an n^+-InAs cap layer (Si-doped to $\geq 1\times10^{19}$ cm^{-3}, 1500 Å) was grown above the grading region. Up to the growth of the n^+-(In,Ga)As graded-gap layer, the substrate temperature was kept constant at about T_{sub} = 550 °C. For the growth of the graded-gap layer and the n^+-InAs cap layer, the substrate temperature was reduced to T_{sub} = 500 °C, because the temperature congruent sublimation for (In,Ga)As decreases with increasing In fraction [17]. Also, the compositional grading was achieved by ramping the temperature of In cell from 730 up to 870 °C at a rising rate of 0.32 °C/s. Furthermore, the Ga-flux was reduced to one fourth of the value thereby reducing the growth rate of GaAs. These factors have been aimed to facilitate the substitution of Ga by In at lower growth rates, thereby facilitating the growth of the grading layer; an $In_{0.1}Ga_{0.9}As$ layer should have been formed at the GaAs end of the grading layer and an $In_{0.76}Ga_{0.24}As$ layer at the InAs end.

Following the MBE growth, the wafer was loaded into a filament evaporation chamber, covered with corresponding masks for the consequent specific contact resistance measurement (Transmission Line Measurement, TLC [13]) and Hall measurement (van der Pauw method). With a background pressure of less than 2.5×10^{-6} Torr, approximately a 1000Å-thick Au metal was evaporated. *No* annealing was performed. An SEM picture of the surface morphology is as shown in Fig. 5.5.

5.4 Results

5.4.1 Current-Voltage (I-V) Characteristics

Figure 5.6 displays the typical I-V trace determined by placing the probes of a curve tracer across

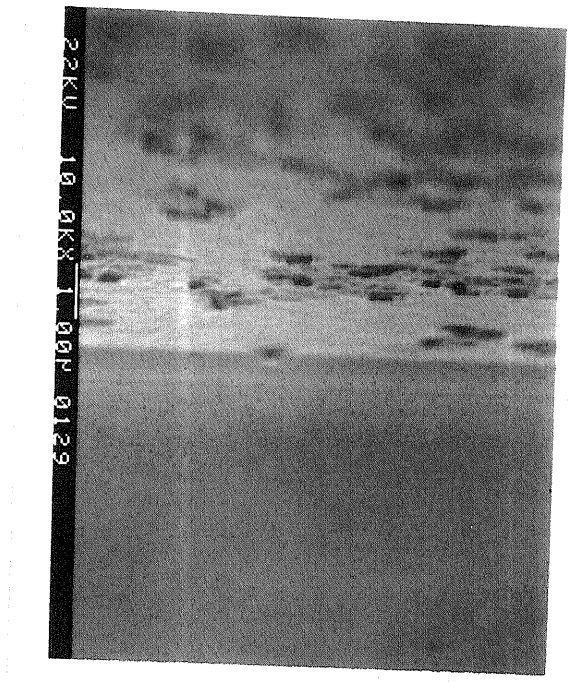

Fig. 5.5 SEM photograph of the prepared sample surface.

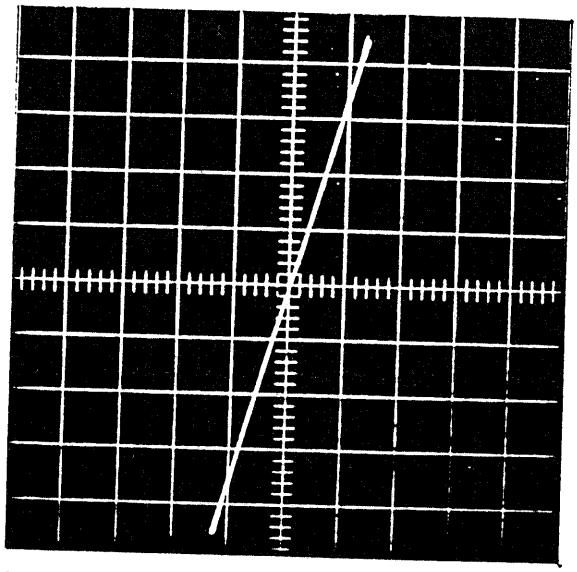

Fig. 5.6 Typical I-V trace determined by a curve tracer.

two of the pads on the TLC. Note again that no annealing has been performed on the wafer. Also, the Hall measurement has revealed that the free carrier concentrations in the InAs and $In_xGa_{1-x}As$ layers were both about 2×10^{19} cm^{-3}. As can be clearly observed, the I-V trace is linear and hence the contacts are those of ohmic contacts. Compared to the typical trace obtained with a Ni/AuGe/*n*-GaAs structure, which would be that of back-to-back "soft" Schottky barriers (before alloying), the result should be of a significant value.

5.4.2 Specific Contact Resistance

If the specific contact resistance ρ_c is known to be much larger than the series bulk resistance, ρ_c can be easily measured by examining the I-V characteristics of a simple diode structure on a curve tracer, or by using a lock-in amplifier to measure the small-signal a.c. current with a small a.c. voltage applied to the diode at zero d.c. bias. If the contact resistance is comparable to or much less than the bulk resistance, then these techniques are clearly inadequate. In this work, a technique due to Yu [13] has been employed as illustrated in Fig. 5.7. Having prepared the sample comprised of an *n*-layer grown on a *p*-layer/substrate and a metal pattern deposited, two probes are used to send a d.c. current I through the *n*-layer strip while the voltage across two other probes is measured. A plot of this voltage/resistance as a function of distance between the corresponding metal pads yields a transfer length L_t as shown in Fig. 5.7(c). The sheet resistance R_s of the strip for the measured R is related by [13],

$$R \approx (R_s / Z)\ [l + 2\,L_t] \tag{5-2}$$

where Z is the contact width and l is the distance between the contacts. The specific contact resistance ρ_c can then be determined from the following equation,

$$\rho_c = R_s L_t^2 \tag{5-3}$$

It has been theoretically shown [11] that with a free carrier concentration in the InAs layer of larger than 1×10^{19} cm^{-3}, ρ_c of as small as 2×10^{-9} Ωcm^2 could be obtained. To date, $\rho_c = 5\times10^{-9}$ Ωcm^2 is known to be the best data [12].

Typical result of the specific contact resistance measurement is shown in Fig. 5.8, and the best

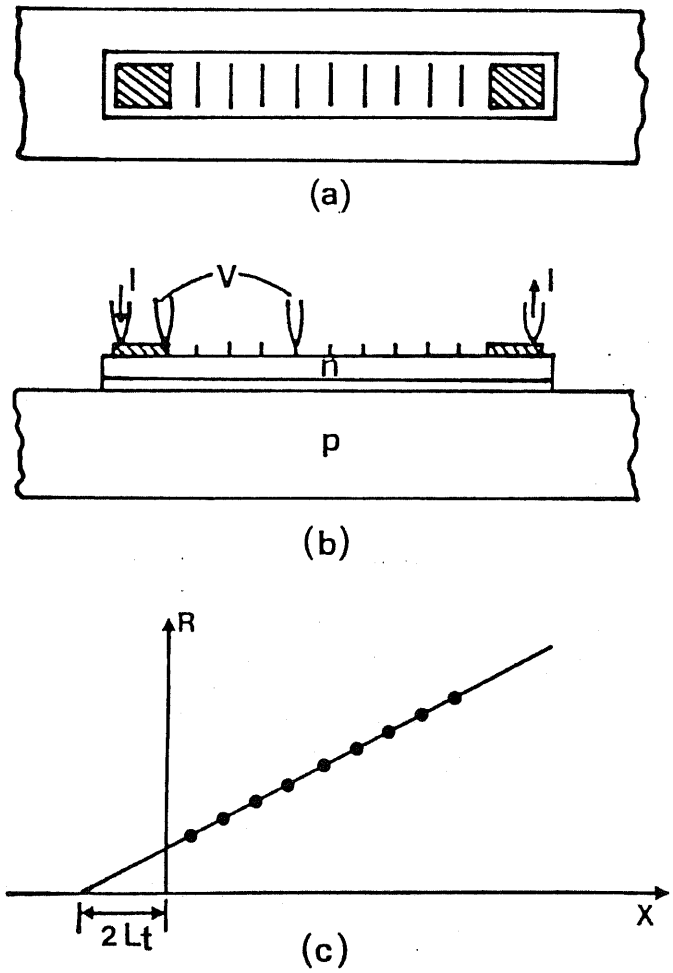

Fig. 5.7 Specific contact resistance measurement using transmission line contact method; (a) top view, (b) side view, and (c) determination of L_t. (After reference [13])

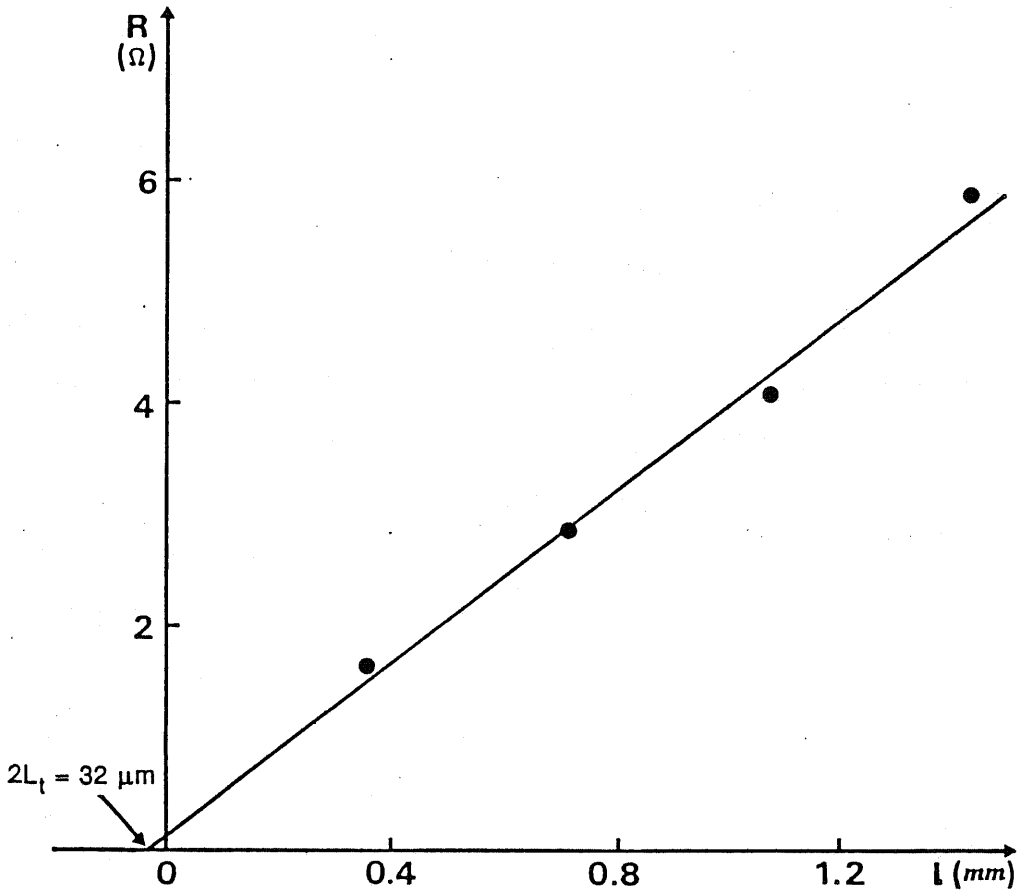

Fig. 5.8 Determination of specific contact resistance.

data of ρ_c measured was obtained as,

$$\rho_c \approx 7\times10^{-6}\ \Omega\text{cm}^2 \tag{5-4}$$

Clearly, as regards to the lowering of the specific contact resistance is concerned, it is apparent that further work needs to be done, however, the present result is nearly two orders of magnitude better than the value obtained in Chapter 4 with Ni/AuGe alloyed contacts. Furthermore, the present results are entirely consistent with the energy diagram shown in Fig. 5.2(d) and with the theory herein. Moreover, Kajiyama *et al.* [18] have reported the compositional dependence of ϕ_b on In composition in $In_xGa_{1-x}As$, and it appears likely that this graded-gap approach can be used to obtain a Schottky barrier height anywhere between that of GaAs (~ 0.9 eV) and that of InAs (0 eV) with the same contact metal. Furthermore, the other important requirements namely, the reproducibility, reliability, and thermal stability have been greatly improved by use of the InAs/$In_xGa_{1-x}As$(x = 1→0) structure to n-GaAs, which therefore is a very promising approach.

5.5 Conclusions

Non-alloyed ohmic contacts to n-GaAs using MBE-grown compositionally graded $In_xGa_{1-x}As$ layers have been investigated, and a specific contact resistance of $\rho_c \approx 7\times10^{-6}\ \Omega\text{cm}^2$ has been obtained using this technique. Clearly, as regards to the lowering of the specific contact resistance is concerned, it is apparent that further work needs to be done, however, the present result is nearly two orders of magnitude better than the value obtained in Chapter 4 with Ni/AuGe alloyed contacts. Furthermore, the present results are entirely consistent with the energy diagram as of Fig. 5.2(d), and with the theory herein. Moreover, this graded-gap approach can be used to obtain a Schottky barrier height anywhere between that of GaAs (~ 0.9 eV) and that of InAs (0 eV) with the same contact metal. Furthermore, the other important requirements namely, the reproducibility, reliability, and thermal stability have been greatly improved by use of the InAs/$In_xGa_{1-x}As$(x = 1→0) structure to n-GaAs, which therefore is a very promising approach. The results should be directly applicable to reduce the emitter contact resistance of the HBT waveguide structure optical modulator/switch under study, and hence the modulation/switching speeds of the device.

References

[1] N. Braslau, J. B. Gunn, and J. L. Staples, "Metal-semiconductor contacts for GaAs bulk effect devices", *Solid-State Electron.*, vol. 10, p. 381, 1967.

[2] T. S. Kuan, P. E. Batson, T. N. Jackson, H. Rupprecht, and E. L. Wilkie, "Electron microscope studies of an alloyed Au/Ni/Au-Ge ohmic contact to GaAs", *J. Appl. Phys.*, vol. 54, p. 6952, 1983.

[3] G. Y. Robinson, "Metallurgical and electrical properties of alloyed Ni/Au-Ge films on *n*-type GaAs", *Solid-State Electron.*, vol. 18, p. 331, 1975.

[4] P. D. Kirchner, T. N. Jackson, G. D. Pettit, and J. M. Woodall, "Low-resistance nonalloyed ohmic contacts to Si-doped molecular beam epitaxial GaAs", *Appl. Phys. Lett.*, vol. 47, p. 26, 1985.

[5] P. A. Barnes and A. Y. Cho, "Nonalloyed ohmic contacts to *n*-GaAs by molecular beam epitaxy", *Appl. Phys. Lett.*, vol. 33, p. 651, 1978.

[6] R. A. Stall, C. E. C. Wood, K. Board, N. Dandekar, L. F. Eastman, and J. Devlin, "A study of Ge/GaAs interfaces grown by molecular beam epitaxy", *J. Appl. Phys.*, vol. 52, p. 4062, 1981.

[7] M. Murakami and W. H. Price, "Thermally stable, low-resistance NiInW ohmic contacts to *n*-type GaAs", *Appl. Phys. Lett.*, vol. 51, p. 664, 1987.

[8] J. M. Woodall, J. L. Freeouf, G. D. Pettit, T. Jackson, and P. Kirchner, "Ohmic contacts to *n*-GaAs using graded band gap layers of $In_xGa_{1-x}As$ grown by molecular beam epitaxy", *J. Vac. Sci. Technol.*, vol. 19, p. 626, 1981.

[9] C. A. Mead and W. G. Spitzer, "Fermi level position at metal-semiconductor interfaces", *Phys. Rev.*, vol. 134, p. A713, 1964.

[10] S. P. Kowalczyk, W. J. Schaffer, E. A. Kraut, and R. W. Grant, "Determination of the InAs-GaAs (100) heterojunction band discontinuities by x-ray photoelectron spectroscopy (XPS)", *J. Vac. Sci. Technol.*, vol. 20, p. 705, 1982.

[11] M. Rao, E. J. Caine, S. I. Long, and H. Kroemer, "AlGaAs/GaAs heterostructure bipolar transistor with nonalloyed graded-gap ohmic contacts to the base and emitter", *IEEE Trans. Electron Devices*, vol. ED-33, p. 1845, 1986.

[12] T. Nittono, H. Ito, O. Nakajima, and T. Ishibashi, "Non-alloyed ohmic contacts to n-GaAs using compositionally graded $In_xGa_{1-x}As$", *Jpn. J. Appl. Phys.*, vol. 27, p. 1718, 1988.

[13] A. Y. C. Yu, "Electron tunneling and contact resistance of metal-silicon contact barriers", *Solid-State Electron.*, vol. 13, p. 239, 1970.

[14] L. L. Chang and J. L. Freeouf, "Ohmic contacts to p-type semiconductors", *IBM Tech. Discl. Bull.*, vol. 24, p. 4065, 1982.

[15] T. Ishikawa, Y. C. Chan, Y. Nakano, and K. Tada, "Application of modern control theory to temperature control of MBE system", *Technical Digest of the 1st International Meeting on Advanced Processing and Characterization Technologies*, Tokyo, p. 17, 1989.

[16] H. Kroemer, Lecture notes taught for the graduate course on *Engineering Quantum Mechanics*, Department of Electrical Engineering, University of California, Santa Barbara, 1988. Also, the subject was discussed with M. Rao, who was at the time working with Prof, H. Kroemer.

[17] C. E. C. Wood, K. Singer, T. Ohashi, L. R. Dawson, and A. J. Noreika, "A pragmatic approach to adatom-induced surface reconstruction of III-V compounds", *J. Appl. Phys.*, vol. 54, p. 2732, 1983.

[18] K. Kajiyama, Y. Mizushima, and S. Sakata, "Schottky barrier height of n-$In_xGa_{1-x}As$ diodes", *Appl. Phys. Lett.*, vol. 23, p. 458, 1973.

CHAPTER 6

SUMMARY AND CONCLUSIONS

The development of sophisticated PICs, to date, has been a gradual process. In as much as optical component integration is the least developed area with PICs, this work has focused on just a few aspects of this problem. In particular, the emphasis of this work has been placed on a particularly desirable geometry for obtaining large index or absorption variations in optical waveguides in semiconductors. The resulting waveguide optical modulator/switch should be directly useful in possible 4×4 optical switch arrays, and may form fundamental building blocks for more sophisticated forms of PICs. For this reason, proposal, analysis, fabrication, and experimental measurement of optical modulation and electrical characteristics of a GaAs/AlGaAs double-heterojunction bipolar transistor (DHBT) waveguide structure carrier-injected optical modulator/switch have been studied.

In Chapter 2, proposal and theoretical analysis on the switching characteristics and the mode propagation behavior of the DHBT waveguide structure applied to a reflection-type X-switch have been presented using the beam propagation method (BPM). It has been concluded that for the proposed structure and $\theta = 4°$, the propagating beam could be switched by total internal reflection at an emitter current of 150 mA and an extinction ratio of ~ 14 dB has been obtained. A charge control analysis showed that the switching times of the proposed bipolar transistor structure can be as fast as ~ 60 ps, which are considerably faster than those expected for diode structures, which are typically on the order of 10 ~ 100 ns. We have also discussed qualitatively and quantitatively a method of reducing the switching current by driving the transistor into the saturation region.

Chapter 3 presents the details of several significant theoretical analyses developed at the University of California at Santa Barbara (UCSB). Using a band-tail model to calculate the absorption coefficient and a Kramers-Kronig analysis to calculate the refractive index, the contribution of the band-filling effect and band-gap shrinkage effect on the absorption coefficient and the refractive index variations due to free carrier injection, which take place in the heavily-doped p-GaAs region of a N-p-N AlGaAs/GaAs DH bipolar transistor optical modulator/switch have been evaluated in detail. It was found that large absorption and refractive index changes can be obtained at photon energies below the band-gap. The calculated results have been analyzed on the basis of the maximum depth of modulation, absorption

losses, and figures of merit, α_c-parameter and β_c-parameter, which determine the degree of spectral broadening that can take place as a result of simultaneous refractive index change with the absorption change. It has been concluded that a carrier-injected optical modulator/switch which is almost free from frequency chirping with low absorption loss can be realized, if the wavelength were properly chosen for the modulation. The device characteristics, however, are expected to be strongly dependent on the operating wavelength among other parameters, and therefore, it is necessary to select the optimum conditions precisely. The optimum photon energy and effective modulator length to be used for optical modulation in our DHBT optical modulator/switch have been determined to be E = 1.38 eV (λ = 899 nm) and ΓL = 100 μm, which would result in a maximum modulation on-off ratio m of about 8 : 1 when the carrier density in the waveguide layer was modulated between $\Delta n = 3\times10^{17}$ and 10×10^{17} cm^{-3}. Furthermore, a sufficiently high value of $P_{on} / P_{in} \approx 0.72$ (−1.4 dB), can be obtained at an injected carrier density $\Delta n = 10\times10^{17} cm^{-3}$. These results indicated that DHBT waveguide structure optical modulator/switch may find very useful applications in optical communication, processing systems, and PICs.

In Chapter 4, device fabrication and experimental measurement of optical modulation and electrical characteristics of a GaAs/AlGaAs DHBT waveguide structure carrier-injected optical intensity modulator grown by molecular beam epitaxy (MBE) have been presented. The device structure was characterized by an incorporation of graded heterojunctions in order to improve the d.c. transistor characteristics, i.e. the collector-base and emitter-base heterojunctions have graded energy-band configurations in order to prevent the occurrence of "spikes", which would adversely affect the injection and collection of minority carriers. Typical common-emitter d.c. current gain obtained with a 0.25 μm-thick base was about 38 and assuming the common-emitter configuration, the switching time t_r was estimated as 1.5 ns. Although t_r was limited by the parasitic impedances, particularly by the emitter contact resistance $R_{ee'}$ (specific contact resistance was no better than $\rho_c \approx 5\times10^{-4}$ Ωcm^2), it has been significantly reduced as compared to the diode-structured devices, whose switching times are typically on the order of several nano seconds. Further technological improvements have to be searched for producing low ohmic contact resistances such as non-alloy ohmic contacts, in order to achieve ultra-fast switching speeds, which in fact have been studied in detail in Chapter 5.

Optical modulation characteristics was determined using a single TE_0-like mode output from a CW GaAs distributed-feedback (DFB) laser diode (λ = 870 nm) and by an end-fire coupling technique. The output light intensity increased almost linearly with the injection current primarily due to the carrier-induced band-filling effect and plasma dispersion effect, and up to 2.1 : 1 optical on/off intensity

modulation or absorption change $\Delta\alpha$ of larger than $-41\ cm^{-1}$ ($\Delta\alpha / \alpha \sim 89\%$) have been demonstrated at a pulsed base current of as small as $I_b \approx 3$ mA or a collector current of $I_c \approx 80$ mA. Experimental results obtained with this optical intensity modulator have also been applied to design, compute, and analyze the device characteristics expected for a semiconductor reflection-type X-crossing optical switch using beam propagation method. It has been shown that an extinction ratio of better than 12 dB could be obtained at $I_b = 1.5$ mA for a device with an intersecting angle of 4°, and switch length of about 110 μm.

Non-alloyed ohmic contacts to *n*-GaAs using MBE-grown compositionally graded $In_xGa_{1-x}As$ layers have been investigated in Chapter 5, and a specific contact resistance of $\rho_c \approx 7\times10^{-6}\ \Omega cm^2$ has been successfully obtained using this technique. In so far as the lowering of the specific contact resistance is concerned, it is apparent that further work needs to be done, however, the present result is nearly two orders of magnitude better than the value obtained in Chapter 4 with Ni/AuGe alloyed contacts. Furthermore, the present results are entirely consistent with the proposed energy diagram, and with the theory herein. Moreover, this graded-gap approach can be used to obtain a Schottky barrier height anywhere between that of GaAs (~ 0.9 eV) and that of InAs (0 eV) with the same contact metal. Furthermore, the other important requirements namely, the reproducibility, reliability, and thermal stability have been greatly improved by use of the InAs/$In_xGa_{1-x}As$($x = 1\rightarrow0$) structure to *n*-GaAs, which therefore is a very promising approach. The results should be directly applicable to reduce the emitter contact resistance of the HBT waveguide structure optical modulator/switch under study, and hence the modulation/switching speeds of the device.